球配列フォトニック結晶の光子のバンド構造と寿命の計算モデルの構築

課題番号　14540293

平成14年度～平成15年度　科学研究費補助金

基盤研究(C)(2)

研究成果報告書

平成16年3月

研究代表者　大高一雄

(千葉大学　先進科学教育センター)

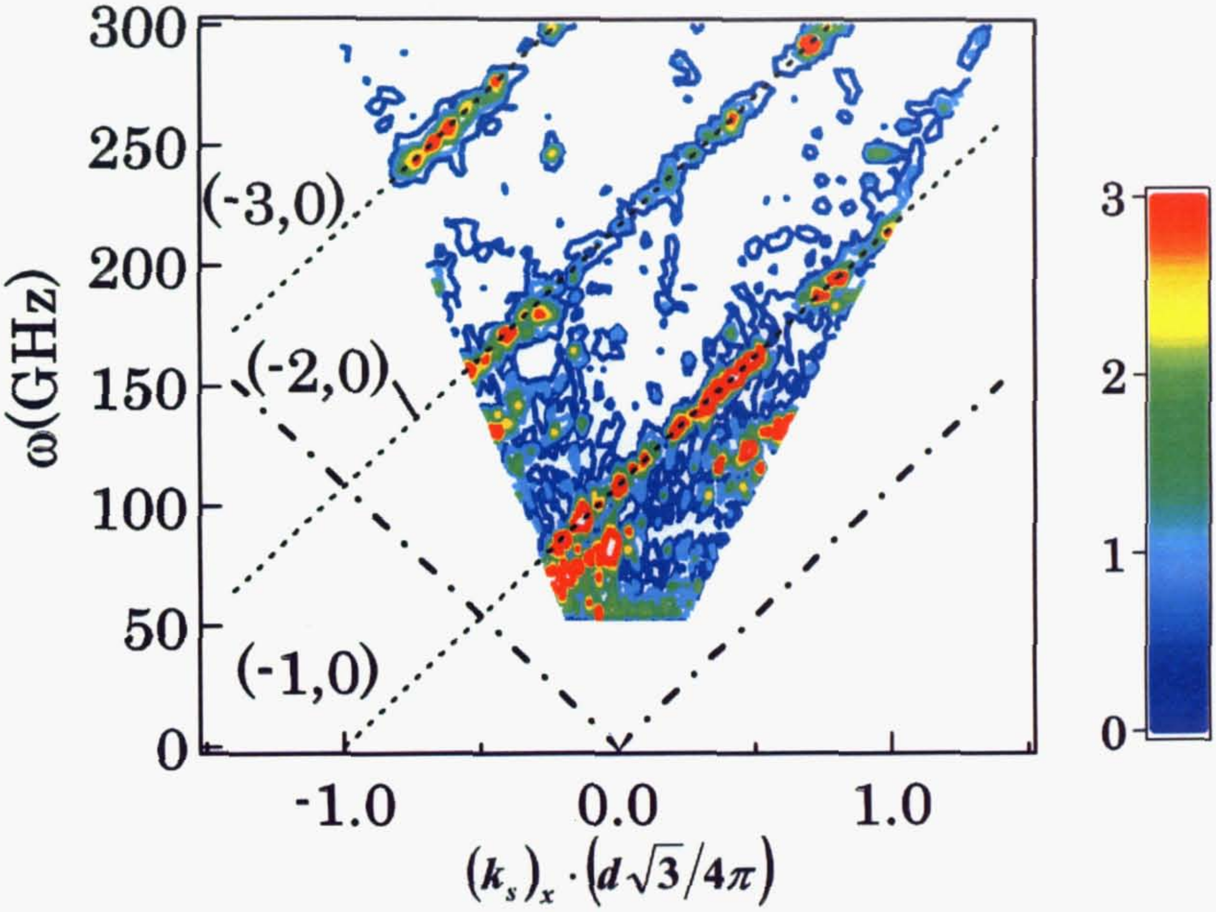

フォトニック結晶からのスミス・パーセル放射の観測データ。150MeVの電子ビームをフォトニック結晶の表面に平行に走らせビームの真上方向で観測。フォトニック結晶は直径3.2mmのpolytetrafluoroethylene (PTFE)球を三角格子に周期配列したもの。dは格子定数、球の屈折率は1.437。電子ビームの真上での放出光子の強度（任意単位）を周波数ωと観測した光子の波数ベクトルの電子ビームの方向への成分$(\boldsymbol{k}_s)_x$の空間内にプロット。$(\boldsymbol{k}_s)_x = 0$はフォトニック結晶の面に垂直方向に対応する。Yamaguti等の理論（論文2)をYamamoto等が実証(論文6) したもの。

平成14年、15年度 科学研究費補助金（基盤研究(C)(2)）「球配列フォトニック結晶の光子のバンド構造と寿命の計算モデルの構築」を終えるにあたって

フォトニック結晶の研究は、デバイスへの展開を視野に入れて、ますます盛んになっている。本研究では、デバイスへの展開において、最も重要な因子となるはずの物質からの光子の漏れに多かれ少なかれ関係する基礎的なテーマの解明を意図している。
ポテンシャルの壁で電子を閉じ込め、電子の漏れを起こさずにデザインどおりの2点を通過させうることが半導体を利用した集積回路の発展の基礎である。これに対し、時間について2階の微分方程式できまる光子のダイナミクスにおいては、光子の閉じ込めはずっと難題であり、系に表面があれば表面からの漏れが避けがたい。本研究は光子の漏れの研究であると言い換えてもよい。
取り扱ったテーマは多岐に渡り、特に、球形および円筒形の誘電体や金属の周期配列系とその関連の非周期系の性質を扱っている。この系は、より複雑なさまざまなフォトニック結晶のもつ諸性質を如実に実現すると同時に、配列単位の、球対称性や軸対称性を利用して数学的解析が完璧に行えるという特徴を持っている。この系を定量的に理解することにより、現実に作成され実験・理論の研究の対象になっている多くのフォトニック結晶の性質を理解することができる。

ほぼ成功裏に成果を収めて報告書をまとめることができるのは研究代表者、分担者を取り囲む、千葉大学、東北大学、理化学研究所、物材機構、日本大学、東京大学、およびベルギーの多くの研究者たちのご協力の賜物である。この報告書の大部分はそれらの研究者たちの業績を採録することで成り立っている。これらの論文の著者たちに厚くお礼を申し上げるとともに深い敬意を表するものである。この研究を基礎にしてよりいっそうフォトニック結晶の分野が発展することを期待している。

平成16年3月31日

研究代表者
千葉大学先進科学教育センター
大高一雄

(1) 研究課題と課題番号

研究課題：球配列フォトニック結晶の光子のバンド構造と寿命の計算モデルの構築

課題番号：14540293

(2) 標題

平成14年度、15年度　（基盤研究（C)(2))

(3) 研究代表者

大高一雄	千葉大学・先進科学教育センター・教授

(4) 研究分担者

宮嵜博司	東北大学・大学院工学研究科・助教授
井上純一	千葉大学・先進科学教育センター・助手

(5) 研究経費 (直接経費)

平成14年度	1,300千円
平成15年度	1,200千円
総計	2,500 千円

(6) 研究発表

研究発表の一覧を示す前に本科研費助成申請に照らして研究課題の狙い・背景・目的・総括を述べておく。

(6)-1. 狙い

この基盤研究の狙いはフォトニック結晶 (PC) で最も典型的にその特徴が現れ、かつベクトル球面波を使うことによって最も完璧に解析ができる誘電体球または誘電体円筒の配列系における光子の挙動を理論的に追求し、とりわけ Mie 散乱の起源をモデル化して電子系の於けるアンダーソンハミルトニアンに相当する光子アンダーソンハミルトニアンの正当性に裏づけを与え、それを用いて PC に関して大規模な数値計算でしか到達し得ない結果を定量的にもできるだけ単純なシナリオで理解しようとする試みである。

(6)-2. 研究の背景

アンダーソンハミルトニアンのオリジナル版は、金属に不純物として含まれる磁性原子が及ぼす伝導電子の挙動を説明するために導入された。不純物原子は鋭い d レベル等からなる順位を持ち、その順位は、エネルギー的に伝導電子のバンドの中に埋め込まれていることがおおい。もしも、伝導電子がトンネル効果によって不純物原子順位に入れば、不純物原子には、はいり込んだ電子のスピンにもとずく磁気モーメントが生じ、他の伝導電子はそれにによってスピンに依存する散乱を受ける。逆に、一旦不純物原子内に入りこんだ電子が、トンネル効果によって伝導帯の平面波状態に抜け出せば、不純物原子の磁気モーメントは突然消滅する。この電子の不純物原子への出入りが伝導電子に時間とスピンに依存する摂動を与え、伝導帯の電子（多体系）はそれに従った挙動をとる。たとえば、磁気モーメントによる散乱をうけ電気抵抗が生じる。この電子の d 順位からの出入りをモデル化したのがアンダーソンハミルトニアンであった。このアンダーソンハミルトニアンを基礎に、近藤効果が議論された。近藤効果は時間に依存して突然現れたり消えたりする摂動にたいする伝導電子の応答がフェルミ面上の電子の散乱断面積に対数的な発散を与え、電気抵抗が温度の現象とともに増加する現象である。

球形であれ、円筒形であれ、孤立した誘電体の中には光の束縛状態（Mie 状態）が生じるが、光の束縛状態は常に孤立系の外部に存在する平面波状態の光子の連続状態の中に埋め込まれている。このため、束縛状態にある光子は完全に光に閉じ込められているのではなく、ある確率で外部に漏れる。光子という粒子像を用いれば、外部の連続状態と内部の鋭い光子の束縛常態の間にの出入りが存在する。このために Mie 状態にいる光子は有限の寿命を持っているといえる。孤立系による光の散乱実験を行うと、この束縛状態があるために、鋭い共鳴的な散乱確率の増大が見られ、その幅はその順位にいる光子の漏れによる寿命を与える。このシナリオは、電子系でのアンダーソンモデルとの類似性を如実に示しているといえる。

Maxwell 方程式を解けば自然にこの幅がついた散乱断面積が計算され、実験ともよい一致を示し、大きな Q 値を持った鋭いスペクトルの光子だめとして Mie 順位を持つ孤立誘電体系を利用することができる。Cavity Quantum Electronics (Cavity QED) はこの巨大な Q 値をもつ Mie 順位にいる光子をレーザー発振や光応答に利用しようとするものである。

このような光子だめの利用は孤立形にとどまらない。フォトニック結晶ではこれらの孤立した単位からの光子の漏れが順位から順位への光子のホッピングのもとになって、強結合バンドが形成される。

大切なことは、漏れによる Mie 順位の状態密度に現れる幅が周期系でのコヒーレントなモードのバンド幅になることである。すなわち、単一孤立系から２孤立系、３孤立系... と孤立系の数を増やしていくと、漏れによる孤立系間の相互作用が生じ、相互作用がなければ、２重、３重... と縮退していた Mie 順位が分裂し、やがて Mie 順位の幅がバンド幅にクロスオーバーしていくという描像が成り立つと思われる。このようにして孤立した単一の系では有限の寿命としてQ値の増大のネックになっていた光子の漏れが、完全な周期系では coherent な光子の状態（したがってその状態にはいった光子の寿命は無限大）を作るもとになるのである。

(6)-3．研究の目的

本研究の目的は

(a) 孤立系からの光子の漏れをできるだけ正確に取り込んだ、光子アンダーソンモデルを構築すること。

(b) 孤立系を連ねることによって、孤立系における漏れによる光子の寿命がフォトニックバンドのバンド幅にいかにクロスオーバーするかを見ること。

(c) 有限のサイズの周期系やまったく周期性を持たない非周期系で、光子の漏れが光子の状態にどのような影響を及ぼすか、また、光応答にその影響がどう現れるか明らかにし、あたらしい現象を提示し、実験の提案をする。

(6)-4．総括

(a) と (b) は密接に関連するが、、この二つの目的については (a) のみを達成しただけで 50 % ほどの達成率である。その理由は、２年間のこのチームのエネルギーは上の目的の (a) のほかは (b) を飛び越して (c) に含まれる

(1)．フォトニック結晶におけるスミス・パーセル放射の解明

(2)．非周期系フォトニック散乱系のギャップの存在と光応答への影響

の研究に集中的に注がれたからである。しかしながら、この (1). と (2). の研究はそのほとんどが Mie モードの漏れによる寿命とその影響としての外部の光シグナルへの共鳴現象が関係している。Mie モードにおける漏れを伴う状態密度の形成が、周期系、非周期系、少数散乱体系でどのような状態密度に変化していくか、どのように光応答に影響するかという総合的な観点で捕らえれば、この２年間の研究はこの基盤研究の課題に合致しているのである。この観点から総括をするならば、達成度は 100%以上のものだったということができる。そのことは以下に掲げる発表論文のリストと (8) で述べるそれぞれの要約、および、本冊子末尾に採録した論文の内容からうかがい知れるとおもう。

(ア)　学会誌等での発表

論文 1.　S. Yamaguti, J. Inoue and K. Ohtaka,
Role of photonic crystals used in the laser acceleration and in the free electron laser
Phys. Rev. B 66, 085209 (2002)

論文 2. S. Yamaguti, J. Inoue, O. Haeberle and K. Ohtaka,　Photonic crystals versus diffraction gratings in Smith-Purcell radiation
Phys. Rev. B 66, 195202 (2002)

論文 3.　K. Amemiya and K. Ohtaka
Calculation of transmittance of light for an array of dielectric rods using vector cylindrical waves: complex unit cells
J. Phys. Soc. Jpn. 72, 1244 (2003)

論文 4.　J. Inoue and K. Ohtaka
Photonic Anderson model: hybridization between photon virtual bound state in dielectrics and free states
J. Phys. Soc. Jpn. 72, 3024 (2003)

論文 5.　J-P. Vigneron, V. Lousse, A. A. Lucas and K. Ohtaka
Amplification of vacuum-ultraviolet radiation by reflection from planar and corrugated aluminum films containing helium excimers
J. Opt. Soc. Am. B 20, 2297 (2003)

論文 6.　K. Yamamoto, H. Miyazaki, K. Ohtaka, et al.
Observation of millimeter-wave radiation generated by the interaction between an electron beam and a photonic crystal
Phys. Rev. E (in press)

論文 7.　T. Ochiai and K. Ohtaka
Relativistic electron energy loss and induced radiation emission in two-dimensional metallic phttonic crystals I: formalism and surface plasmon polariton
Phys. Rev. B (in press)

論文 8.　T. Ochiai and K. Ohtaka
Relativistic electron energy loss and induced radiation emission in two-dimensional metallic phttonic crystals II: photonic band effect
Phys. Rev. B (in press)

論文 9.　S. Yamaguti, T. Ochiai, J. Inoue and K. Ohtaka
Means of sending a photon to an optically inactive photonic-band mode
Phys. Rev. B (in press)

論文 10.　K. Ohtaka, S. Inoue and S. Yamaguti
Derivation of the density of states of leaky photonic bands
Phys. Rev. B (in press)

論文 11. M. Hase, M. Egashira, H. Miyazaki, et al.
Optical transmission spectra of two-dimensional quasiperiodic photonic crystals based on Penrose-tiling and octagonal-tiling systems.
Journal of Alloys and Compounds 342, 455 (2002)

論文 12. M. Hase, H. Miyazaki, M. Egashira, et al.
Isotropic photonic band gap and anisotropic structures in transmission spectra of two-dimensional fivefold and eightfold symmetric quasi-periodic photonic crystals
Phys. Rev., B66, 214205 (2002)

論文 13. H. T. Miyazaki, H. Miyazaki, K. Miyano
Anomalous scattering from dielectric bispheres in the specular direction. Optics Letters, 27,1208 (2002)

論文 14. H. T. Miyazaki, H. Miyazaki and K. Miyano
Analysis of specular resonance in dielectric bispheres using rigorous and geometrical-optics theories
J. Opt. Soc. Am., A20, 1771 (2003)

論文 15. H. T. Miyazaki, H. Miyazaki and K. Miyano Enhanced light diffraction from a double-layer microsphere lattices
Appl. Phys. Lett., 83, 3662 (2003)

論文 16. H. Miyazaki, M. Hase, H. T. Miyazaki, et al.
Photonic material for designing arbitrarily shaped waveguides in two dimension
Phys. Rev., B67, 235109 (2003)

論文 17. H. T. Miyazaki, H. Miyazaki, Y. Jimba, et al.
Light diffraction from a bilayer lattice of microspheres enhanced by specular resonance
J. Appl. Phys. 95, 793 (2003)

論文 18. H. Miyazaki, M. Hase, H. T. Miyazaki, et al.
Photonic material for designing arbitrarily shaped mirrors and microcavities in two dimension
J. Appl. Phys. (in press)

論文 19. N. Horiuchi, Y. Segawa and H. Miyazaki
Isotropic photonicgaps in a circular photonic crystal
Optics Lett. (in press)

論文 20. Y. Kurokawa, H. Miyazaki and Y. Jimba
Optical band structure and near-field images of a periodically arrayed monolayer of dielectric spheres on dielectric substrate of finite thickness
Phys. Rev. B. (in press)

（イ）口頭発表

（イ）-1 国内会議での発表

1. 堀内典明、瀬川勇三郎、宮嵜博司、他
二次元円座標のフォトニック結晶の光学特性I
日本物理学会2002年秋の分科会　中部大学　9月6日　(2002)

2. 山本貴一、山口修一、大高一雄、他
高エネルギー電子線とフォトニック結晶の相互作用に関する実験III
日本物理学会2002年秋の分科会　中部大学　9月6日　(2002)

3. 黒川要一、神馬洋司、宮嵜博司
二次元周期誘電体球の内部電場に対する基盤の効果
日本物理学会2002年秋の分科会　中部大学　9月6日　(2002)

4. 宮嵜博司、神馬洋司
二次元配列された少数誘電体球の透過率の計算
日本物理学会2002年秋の分科会　中部大学　9月6日　(2002)

5. 山口修一、大高一雄
フォトニックバンドの励起に伴う光の回折とレーザー発振
日本物理学会2002年秋の分科会　中部大学　9月6日　(2002)

6. 井上修一、大高一雄
whispering gallery modeの球外部への染み出しとフォトニックバンド
日本物理学会2002年秋の分科会　中部大学　9月6日　(2002)

7. 井上修一、大高一雄
whispering gallery modeの球外部への染み出しとフォトニックバンドII
日本物理学会第58回年次大会　東北大学　3月28日　(2003)

8. 山口修一、大高一雄
不活性フォトニックバンドの観測可能性
日本物理学会第58回年次大会　東北大学　3月28日　(2003)

9. 堀内典明、瀬川勇三郎、宮崎博司、他
二次元円座標フォトニック結晶の光学特性II
日本物理学会第58回年次大会　東北大学　3月28日　(2003)

10. 野林和哉、黒川要一、宮嵜博司
回転対称フォトニック結晶を用いた2次元導波路中の電磁波解析II
日本物理学会第58回年次大会　東北大学　3月28日　(2003)

11. 黒川要一、神馬洋司、宮嵜博司
境界要素法による任意の形状をした散乱体からの光散乱
日本物理学会第58回年次大会　東北大学　3月28日　(2003)

12. 宮嵜博司、長谷正司、宮崎英樹、他
等方分布円筒群(UDPS)のフォトニックギャップ
日本物理学会2003年秋の分科会　岡山大学　9月23日 (2003)

13. 宮嵜博司、長谷正司、宮崎英樹、他
等方分布円筒群(UDPS)による2次元光導波路
日本物理学会2003年秋の分科会 岡山大学　9月23日 (2003)

14. 黒川要一、神馬洋司、宮嵜博司
境界要素法による回転対称性を持った散乱体からの光散乱の特性
日本物理学会2003年秋の分科会 岡山大学　9月23日 (2003)

15. 堀内典明、瀬川勇三郎、宮嵜博司、他
円座標フォトニック結晶の透過スペクトル
日本物理学会第59回年次大会　九州大学　3月27日　(2004)

16. 宮嵜博司、長谷正司、宮崎英樹、他
等方分布円筒群(UDPS)による2次元マイクロキャビティーの設計
日本物理学会第59回年次大会　九州大学　3月27日　(2004)

17. 瀬川勇三郎、宮嵜博司、大高一雄、他
高エネルギー電子線とフォトニック結晶との相互作用に関する実験IV
日本物理学会第59回年次大会　九州大学　3月27日　(2004)

18. 落合哲行、大高一雄
スラブ型フォトニック結晶における局所状態密度と自発放出光の指向性
日本物理学会第59回年次大会　九州大学　3月27日　(2004)

19. 黒川要一、神馬洋司、宮嵜博司
ベクトルKKR法による有限高さの2次元周期フォトニック結晶によるフォトニックバンド
日本物理学会第59回年次大会　九州大学　3月27日　(2004)

20. 井上純一
誘電体球列における球内光励起モードの伝播
日本物理学会第59回年次大会　九州大学　3月27日　(2004)

（イ）－2 国際会議での発表

1. K. Ohtaka
Density of states of photonic crystals and its effects on lasing and electron-photon interaction
International Conference on Quantum Optics, Minsk, Belarus, May 2002

2. K. Ohtaka

Energy loss spectrum from a traveling electron due to the emission of photons
Werner Brandt Workshop on Charge Scattering, Namur, Belgium, June 2002

3. J. Inoue and K. Ohtaka
Photon virtual bound state
DPC03, Christchurch, New Zealand, August 2003

4. T. Ochiai and K. Ohtaka
Relativistic electron energy loss and Smith-Purcell radiation in two-dimensional metallic photonic crystals
Euroconference on Nano-Optics, Granada, Spain, September 2003 5. K. Ohtaka
Optical excitation of optically inactive photonic band modes
PECS-V, Kyoto, Japan, March 2004

6. T. Ochiai and K. Ohtaka
Relativistic electron energy loss in 2d and 3d photonic crystals
PECS-V, Kyoto, Japan, March 2004

7. H. T. Miyazaki, H. Miyazaki, Y. Jimba, et al.
Enhanced light diffraction from a double-layer microsphere lattice and its application to transmission gratings
PECS-V, Kyoto, Japan, March 2004

8. N. Horiuchi,Y. Segawa, H. Miyazaki, et al.
Bent-line-defect waveguides by using circular photonic crystal
PECS-V, Kyoto, Japan, March 2004

(7) 研究成果による工業所有権の出願・取得状況

なし

(8) 研究成果

「球形の誘電体からの光子のトンネルに基づくモデルを構築すること」については所期の目的を達成して光子アンダーソンモデルともいうべきモデルハミルトニアンの導出に成功した。球形内部の光子の局在順位と光子の外部の平面波の光子状態の重なりを、完全性を壊すことのない定式化で捕らえ、数値計算との一致が極めてよい結合定数の表式を得、仮想束縛状態の諸性質を明らかにした。

「光子の誘電体からの漏れを取り込んだフォトニックバンドの諸性質の解明」については、状態密度のスペクトルから漏れによる光子の寿命と漏れを取り込んだフォトニックバンドの分散を求める公式の導出に成功した。そして、その公式を用いることによって、フォトニック結晶の近くを走る電子からの発光スペクトルに鋭い線スペクトルが現れ、そのピーク高が励起したフォトニックバンドの寿命を用いて解釈できることを明らかにした。さらに電子のエネルギー損失スペクトルの計算にも成功し、電子からの放出電磁波のフォトニック結晶による吸収によるエネルギー損失と光子放出によるエネルギー損失の比較をおこなうなどのいくつかの新しい物理量の計算に成功した。金属フォトニック結晶についての理論的な解析も完結し、実験を待つばかりになっている。

「光子の誘電体からの漏れを取り込んだ非周期系の光子の諸性質の解明」については円筒上誘電体や球状誘電体が、周期系ではないが、隣接単位間の距離がある程度の距離を置いて離れているという制限を加えたuniformly distributed photonic scatterers (UDPS) という新しい系を提唱し、この円筒誘電体群の系が光子の漏れの制御に著しく有効

であることを数値計算で明らかにした。また、全方位バンドギャップの出現の重要性にかんがみ円座標周期系ともいうべき新しい系での光子の性質を調べ、入射光の方向に依存しない周波数帯域に状態密度がほぼ消滅する領域が出現することを明らかにした。

「光子の誘電体からの漏れを取り込んだ誘電体集合の光応答の解明」では光の回折現象に著しい特徴が現れることを少数散乱体系で示しその起源を明らかにした。また、その特異性を利用した導波路などのデバイスの提案をおこなった。さらに外部光から完全に遮断されたフォトニックバンド状態に光子を送り込む方法の提案を行い、この状態が「光子だめ」として利用価値があることを明らかにした。

これらをさらに詳しく、約20編になる既刊および印刷中の論文ごとに要約を加えて解説する。論文の番号は(6)アで用いた番号である。

論文1. 荷電粒子をレーザーを用いて加速するのにフォトニック結晶を利用することを提案した。Q値の大きいバンドを励起することで回折エバネッセント電場の強度が増強され、その結果強い力が荷電粒子に加わり大きく加速される。我々は2次元フォトニック結晶から3次元的に層数を増やしながらその効率の変化について検討した。またこの結果は低閾値の自由電子レーザーに適用することが可能で、フォトニック結晶がこの2つのデバイスについて非常に有効であることを明らかにした。

論文2. 通常使われる回折格子の代わりに2次元周期をもつフォトニック結晶を使った場合のスミス・パーセル放射のスペクトルの解析をした。回折格子の場合はWood anomalyと呼ばれる現象により幅の広いスペクトルを示すがフォトニック結晶ではそのバンド構造に強く依存することがわかった。Q値の大きいバンド励起を利用することにより通常の回折格子の場合に比べて10倍ないし100倍程度の発光強度の増強が理論的に示された。

論文 3. 円筒形誘電体からなるフォトニック結晶について、ユニットセル内に 2 本以上の円筒が存在する複雑なユニットセルに対して、ベクトル円筒波展開法の定式化を行なった。不純物バンドの構造と透過スペクトルの比較、損失のある不純物の影響、曲がりのある欠陥導波路の透過スペクトルの解析に用いることにより、不純物のあるフォトニック結晶の性質を明らかにするとともに、この計算法の有用性を示した。

論文 4. 応用上重要と考えられている，低群速度分散をもつフォトニックバンドは，単位構造内に励起されるいわゆる共鳴モードと，自由空間を伝播する光との結合により，単位構造同士の強結合モデルで理解できると考えられてきた．しかし，その結合係数に関する微視的な理論はこれまで存在しなかった．そこで，単位構造として誘電体球をとり，それを自由空間を伝播する光にとっての不純物という扱いをすることで，磁性問題のアンダーソンモデルに相似な関係となることを示し，結合係数の微視的な表式を導出した．また，本理論に基づく球内励起モードの状態密度が，数値解と良い一致を与えることも確認した。

論文 5. 金属内で周期構造をとる空孔内の励起 He 原子からの光の誘導放射を誘電率の虚部に光増幅をとりいれることによって解析し、周期配列空孔を含む金属の厚さの関数として真空紫外光の誘導放射を制御する可能性を議論した。

論文 6. フォトニック結晶の表面近傍を電子が等速度で通過するときに、特定方向に強い光放射を観測した。放射された光の運動量とエネルギー間の関係は、この光がフォトニック結晶によるウムクラップ散乱により、電子から放射された減衰波が進行波となったものであることを示している。実験により得られた光放射スペクトルと、理論計算により求まる光放射スペクトルとを比較することにより、スペクトルにみられる鋭い微細構造は、フォトニックバンドモードが共鳴的に励

論文3. 円筒形誘電体からなるフォトニック結晶について、ユニットセル内に2本以上の円筒が存在する複雑なユニットセルに対して、ベクトル円筒波展開法の定式化を行なった。不純物バンドの構造と透過スペクトルの比較、損失のある不純物の影響、曲がりのある欠陥導波路の透過スペクトルの解析に用いることにより、不純物のあるフォトニック結晶の性質を明らかにするとともに、この計算法の有用性を示した。

論文4. 応用上重要と考えられている，低群速度分散をもつフォトニックバンドは，単位構造内に励起されるいわゆる共鳴モードと，自由空間を伝播する光との結合により，単位構造同士の強結合モデルで理解できると考えられてきた．しかし，その結合係数に関する微視的な理論はこれまで存在しなかった．そこで，単位構造として誘電体球をとり，それを自由空間を伝播する光にとっての不純物という扱いをすることで，磁性問題のアンダーソンモデルに相似な関係となることを示し，結合係数の微視的な表式を導出した．また，本理論に基づく球内励起モードの状態密度が，数値解と良い一致を与えることも確認した。

論文5. 金属内で周期構造をとる空孔内の励起He原子からの光の誘導放射を誘電率の虚部に光増幅をとりいれることによって解析し、周期配列空孔を含む金属の厚さの関数として真空紫外光の誘導放射を制御する可能性を議論した。

論文6. フォトニック結晶の表面近傍を電子が等速度で通過するときに、特定方向に強い光放射を観測した。放射された光の運動量とエネルギー間の関係は、この光がフォトニック結晶によるウムクラップ散乱により、電子から放射された減衰波が進行波となったものであることを示している。実験により得られた光放射スペクトルと、理論計算により求まる光放射スペクトルとを比較することにより、スペクトルにみられる鋭い微細構造は、フォトニックバンドモードが共鳴的に励

バンドの分散と寿命が決まることを示した。

論文11. 誘電体円柱を用いて5回と8回の回転対称を持つ2次元準周期フォトニック結晶の透過率を実験的に求め，理論計算の結果と比較した．その結果，誘電率が2.4という低い場合でもTMモードにおいてフォトニックギャップを確認することが出来た。

論文12. 誘電体円柱によって構成される5回回転対称Penrose準結晶と8回回転対称準結晶の光学的性質を研究した。誘電率が2.4の低い値でもTMモードに等方的なフォトニックギャップが確認された．これらのギャップは数本の円柱の場合でも既に前駆的な兆候が見られることが数値計算によって示された。等方的なフォトニックギャップのほかに非等方的なディップ構造が透過率に見出された。これらの非等方的なディップは体系全体にわたる光の多重散乱の結果現れるものと推測される。一方，等方的なギャップでは光の局所的な多重散乱が重要な役割を果たすことが分った。

論文13. マイクロ波の領域で観測されていた2連球における鏡面反射現象を可視光の領域で観測した。マイクロマニピュレーション法によってミクロンサイズの2連誘電体球を系統的に作製した．それらの試料の測定の結果，鏡面反射現象は古典的な「虹」の前駆的な効果としてきわめて普遍的なパラメータの範囲で観測されることが判明した。

論文14. 2連球における鏡面反射現象は特殊なパラメータの範囲に限られた現象ではなく，屈折率が1.2から2.2程度でサイズパラメータが5以上であれば容易に観測される普遍的な現象であることを厳密な理論計算と幾何光学における光線追跡法を用いて示した。

論文15. 2層の周期誘電体球系において55％以上の高効率を持つ異常な回折現象を見出した．効率の増強の原因は2連球による鏡面特異反射であることが分った．単層や3層の周期球系ではこのような増強効

果は見出せない。その応用としてblazed transmission gratingがあげられる。

論文16. 誘電体円柱がランダムで且つ稠密に分布した構造では，円柱密度と誘電率比がある閾値を超えると等方的なギャップが現れることを見出した。フォトニックギャップの出現には長距離秩序も短距離秩序も必要ないことが示された。UDPSと呼ばれるこの新たな光物質を用いれば波長程度の大きさを持った任意形状の導波路を容易に作製することが出来る。

論文17. 厳密な解析計算と実験結果を用いて，先に報告した2層の周期誘電体球系における異常回折効果の原因が2連球による鏡面特異反射であることを確かめた。波長の1.6から3.2倍程度の直径を持つ球は特に効率よく鏡面特異反射を起こすことが分った。また，球の代わりに円柱を使うことも可能であることが示された。

論文18. 構造的な一様性と大きな等方的フォトニックギャップを有するＵＤＰＳと称する光学物質を用いてフォトニックニックプレートを提唱した。このフォトニックプレートを用いれば波長と同程度のサイズを持つ任意形状の微小鏡や微小キャビティーを作成することができる。また，キャビティーの共鳴周波数の設計も容易にできる。

論文19. 誘電体円柱群によって作られた円座標フォトニック結晶の光学的な性質を研究した。試料はミリメータサイズのアルミナ円柱によって構成されており，測定領域は20GHｚ帯域までである。その結果，円座標フォトニック結晶が等方的なフォトニックギャップを持つことが見出された。

論文20. 2次元周期誘電体球系に及ぼす有限厚さの基板の効果を数値的に解析した．透過率から得られたフォトニックバンド構造は実験結果とよく一致した。透過スペクトルは基板のない場合に比べて著しい

変化を見せた。その変化は基板に局在した固有モードとの相互作用に由来することが分った。

Observation of Millimeter-Wave Radiation Generated by the Interaction between an Electron Beam and a Photonic Crystal

K. Yamamoto[1,*], R. Sakakibara[2], S. Yano[1], Y. Segawa[1,2], Y. Shibata[3], K. Ishi[3],
T. Ohsaka[3], T. Hara[4], Y. Kondo[4], H. Miyazaki[4], F. Hinode[5], T. Matsuyama[5],
S. Yamaguti[6], and K. Ohtaka[7]

[1] *Photodynamics Research Center, The Institute of Physical and Chemical Research (RIKEN), Sendai 980-0845, Japan*

[2] *Department of Physics, Tohoku University, Sendai 980-8578, Japan*

[3] *Institute of Multidisciplinary Research for Advanced Materials, Tohoku University, 980-8577, Japan*

[4] *Department of Applied Physics, Tohoku University, Sendai 980-8579, Japan*

[5] *Laboratory of Nuclear Science, Tohoku University, Sendai 982-0826, Japan*

[6] *Graduate School of Science and Technology, Chiba University, Chiba 263-8522, Japan*

[7] *Center for Frontier Science, Chiba University, Chiba 263-8522, Japan*

Abstract

We observed directional light emission in the millimeter-wave region when a high-energy (150 MeV) electron beam passes just above a photonic crystal made of polytetrafluoroethylene beads ($\simeq 3.2$ mm in diameter). The relation between the momentum and the energy of the emitted photons strongly suggests that the observed light is generated by the umklapp scattering process that changes the evanescent waves emitted by the electron beam into observable ones. By comparing the observed spectra with calculated ones based on the photonic band structure, we found that generated photons excite the photonic band modes making them observable as enhanced fine structures in the emission spectra.

PACS numbers : 42.70.Qs, 41.60.-m

Photonic crystals (PhCs) have drawn much attention due to their potential applications to new types of optical materials. Owing to their multidimensional periodic dielectric structures, they show unique optical properties arising from so called a photonic band gap (PBG) and a photonic band (PB) [1–4]. In these days, light emission phenomena involving the excitation of PB modes have become one of the hottest issues in this field of investigation, because they are expected to show novel features; sharply enhanced Smith-Purcell radiation (refs. 5 – 7) and backward-pointing Cherenkov radiation (ref. 8) are such examples. These novel features obviously come from the peculiar energy dispersion of photon (PBs) in PhCs. Recently, an electron energy-loss spectroscopy (EELS) study has reported the Cherenkov effect of a PhC [9]. However, to the best of our knowledge, there is no study on direct observation of the radiation involving the excitation of PB modes. In this communication, we would like to report an experimental study of one of the radiation phenomena, which was based on the theoretical prediction in refs. 5 – 7, to demonstrate that the light emission involving the excitation of PB modes can indeed be observed.

Let us briefly explain the formulation of the light emission mechanism. An electron running at a constant velocity in the x direction (Fig. 1(a)) emits an evanescent light whose wave vector is defined by

$$\mathbf{k}_i = (k_x, q_y, \Gamma_i). \tag{1}$$

The suffix i of $\mathbf{k}_i$ shows that this evanescent light is taken to be an incident light on the PhC. We define the direction that is perpendicular to the PhC as the z direction (Fig. 1(d)). Note that the x component of $\mathbf{k}_i$ is fixed at the value $k_x = \omega/v$, where ω is the frequency of the emitted light that varies from zero to infinity, and v is the velocity of the running charge. The evanescent wave can be expressed by the superposition over q_y values. Γ_i is the quantity that governs the propagation in the z direction of the evanescent light and which is defined by

$$\Gamma_i = \sqrt{\frac{\omega^2}{c^2} - k_x^2 - q_y^2} \equiv \sqrt{\frac{\omega^2}{c^2} - \frac{\omega^2}{v^2} - q_y^2}. \tag{2}$$

Since v is always smaller than c, Γ_i is always an imaginary number. This is why the direct light from the charge is evanescent.

The umklapp process in the subsequent light scattering of the evanescent light by a periodic structure (a grating or a PhC) converts it into a light which can be observed at a far-field observation point. In a triangular lattice of a two-dimensional (2D) periodic array of beads (see Fig. 1(a)), which is the PhC used in the present study, basis vectors of the reciprocal space are (see Fig. 1(b))

$$\mathrm{K}_1 = \frac{4\pi}{d\sqrt{3}}(1,0) \equiv (K_{1x}, K_{1y}), \tag{3}$$

$$\mathrm{K}_2 = \frac{4\pi}{d\sqrt{3}}(\frac{1}{2}, \frac{\sqrt{3}}{2}) \equiv (K_{2x}, K_{2y}), \tag{4}$$

where d is the diameter of each bead composing the PhC. The radiation due to the umklapp process can then be described by a propagating plane wave whose wave vector is

$$\mathbf{k}_s = (k_x + mK_{1x} + nK_{2x}, q_y + mK_{1y} + nK_{2y}, \Gamma_{mn}), \tag{5}$$

with two integers m and n. By the energy-momentum relation, Γ_{mn} is given by

$$\Gamma_{mn} = \sqrt{\frac{\omega^2}{c^2} - (\frac{\omega}{v} + mK_{1x} + nK_{2x})^2 - (q_y + mK_{1y} + nK_{2y})^2}. \tag{6}$$

In the (k, ω) space, therefore, the dispersion line of the evanescent light is shifted by $m\mathrm{K}_1 + n\mathrm{K}_2$, from the outside to the inside region of the light cone whose boundary is the light line ($\omega = ck$) (see Fig. 1(c)). In the following, we call these shifted evanescent light dispersion lines $\mathbf{H}_{m,n}$ lines, using a set of (m, n) that defines the wave vector of the propagating light after the scattering.

If we use a metallic grating as a periodic structure, the effect formulated above is known as Smith-Purcell radiation (SPR) [10,11]. The difference from SPR arises when we use PhCs in place of a metallic grating; the photons on the $\mathbf{H}_{m,n}$ lines are expected to excite PB modes. It is predicted theoretically that a strongly enhanced sharp light emission will be generated from PhCs [5-7]. Such a strongly enhanced light emission reflects the confinement effect of electromagnetic energies, which results from the high Q value of an excited PB [12]. The purpose of the present study is to observe such resonant emission of photons by exciting a PB mode (REPEP).

We prepared the experimental set up illustrated in Fig. 1(d) at the Laboratory of Nuclear Science (LNS), Tohoku University. Electrons with the energy of 150 MeV from the S-band linear accelerator passed near the PhC in Fig. 1(d). The duration of a burst of electron pulses was 1.8 μs, whose repetition rate was 16.67 Hz. Average beam current was typically 1.0 μA. The cross section of the beam was about 10×12 mm^2. The height of the beam shown in Fig. 1(d) was 10 mm. In order to obtain emission angle dependence, we varied the angle θ of Fig. 1(d) from 60° to 112° by moving the mirror M1. The acceptance angle of the optical system was $\pm 0.75°$ in the xz-plane, and $\pm 1.4°$ in the yz-plane. The radiated light was directed to a Martin-Puplett type Fourier-transform spectrometer equipped with a liquid helium-cooled Si bolometer. The resolution of the spectrometer was 3.75 GHz.

The PhC used in this study (Fig. 1(a)) is a single layer of polytetrafluoroethylene (PTFE) beads periodically arrayed in a 2D triangular lattice. The diameter of a bead is 1/8 inch ($\simeq$ 3.2 mm). In a single layer of beads arrayed in a 2D lattice structure, each whispering gallery (WG) mode of a bead, specified by the angular momentum index (l, m), couples with WG modes of other beads to form tight binding bands with 2D dispersion. The $(2l + 1)$-fold degeneracy of the WG mode is partly lifted in a lattice of beads due to this mode mixing, producing the densely populated 2D PB structure. Existence of such PB structures in PhCs of single layered beads has already been probed by the incident-angle dependent transmission spectra of them, and very good agreement with the calculated dispersion relation was confirmed [13–15].

Let us turn our eyes on the experimental result and discussion. Figures 2(b) and 2(c) show spectral changes in the emitted light as θ is varied. We can see sharp peaks with a band width (FWHM) typically of about 5 GHz. The spectrum is thus characterized by the presence of monochromatic light emissions. It should be noted that these emission peaks present strong θ-dependence. For example, the peaks indexed as (-1, 0), (-2, 0), and (-3, 0) change their intensities drastically within the angle variation of 5° in Figs. 2(b) and 2(c).

To determine the origin of the directional light emission, the measured intensity data in the (θ, ω) plane was converted to those of $((k_s)_x,\ \omega)$, where $(k_s)_x$ is the x-component of $\mathbf{k}_s$ defined by Eq. (5). The values of $(k_s)_x$ are derived from θ by using the relation $(k_s)_x = \frac{\omega}{c}\cos\theta$. The y-component of $\mathbf{k}_s$ can be considered to be zero ($(k_s)_y = 0$), because the mirror M1 in our measurement system (Fig. 1(d)), which stands perpendicular to the xz-plane, always moves within xz-plane. The contour map of the intensity thus obtained is shown in Fig. 3. We can see that intense light emission indeed occurs around the $\mathbf{H}_{-1,0}$ line, and even around the $\mathbf{H}_{-2,0}$ and $\mathbf{H}_{-3,0}$ lines (Fig. 3). This indicates that the emitted photons corresponding to these parts are generated through the PhC and emitted into the direction determined by Eq. (5).

In the emission spectra, however, there are some peaks that are not on the $\mathbf{H}_{m,n}$ lines: such emission peaks are indicated by asterisks in Figs. 2(b) and 2(c). These emission peaks correspond to the part with strong emission intensity below $\mathbf{H}_{-1,0}$ line in $((k_s)_x,\ \omega)$ plane (Fig. 3). One of the possible origins is an excitation of PBs by the transition radiation, because the area of the light emission in the $((k_s)_x,\ \omega)$ plane almost coincide with the calculated PB dispersion curves. Since we cannot clearly identify the origin of these light emissions at this stage, we will focus only on the light emission peaks on the $\mathbf{H}_{m,n}$ lines in the following discussion.

Next, let us discuss the origin of the strong θ-dependence of the emission intensity along the $\mathbf{H}_{m,n}$ lines. If it were not for any dispersion curve of special modes in the $((k_s)_x,\ \omega)$ plane, the emission intensity would show a smooth variation on θ. This is the case in a grating system, where the SPR spectrum has generally a smooth change except the fine structures brought about by Wood anomaly [16,17]. Moreover, fine structures of SPR spectra have their θ dependence much smaller than those observed here [7]. The strong θ dependence observed here therefore proves that the emission is indeed of REPEP origin, which is schematically explained in Fig. 1(c). By varying ω of the observed photons with θ kept fixed, we can experimentally sweep $((k_s)_x,\ \omega)$ space along the line $\omega = c(k_s)_x/\cos\theta$ (called observation line). An enhanced light emission occurs only when all the three curves, the observation line,

$H_{m,n}$ line and the dispersion curve of a PB, meet together in the $((k_s)_x, \omega)$ space. In Fig. 1(c), three observation lines are drawn to show that only the θ_2 line has an enhanced signal. By varying θ, we can tilt the observation line to spoil the matching. This is the origin of the rapid θ dependence on the $H_{m,n}$ line. Since PBs have finite lifetimes, a dispersion curve has a finite width, which determines the sharpness of the θ dependence of REPEP signal.

If the peaks of the spectrum indeed arise from the excitation of PB modes along the $H_{m,n}$ line, they should reflect the PB structure. In order to confirm this point, we calculated the PB structure and the spectrum of the emitted light by using the vector KKR formalism [1,18,19], which is the same method as that presented in ref. 7. The value of the complex refractive index of the PTFE beads used in the calculation of the emission spectrum was $1.437 + 0.0002i$ $(i^2 = -1)$ [13]. We can find a good correspondence between the calculated emission peak positions (Fig. 4(b)) and the position where the PBs cross with the $\mathbf{H}_{-1,0}$ line (Fig. 4(a)).

Then let us compare the calculated emission spectrum (Fig. 4(b)) and the observed one (Fig. 4(c)). The spectrum was calculated along with a dispersion line, $\mathbf{H}_{-1,0}$ (Fig. 4(a)) in the $((k_s)_x, \omega)$ plane. Since the intensity of the experimental results shown in Fig. 4(c) is not corrected by the difference in intensities arising from the difference in optical paths between each θ-const. spectrum (see Fig. 1(d)), we can only discuss the peak positions of the observed light emission. Besides the peaks indicated by crosses [20], the peak positions in the frequency ranges of $140 - 170$, $125 - 140$, and $90 - 110$ GHz in the observed spectrum correspond well to those in the calculated one [21]. This provides strong evidence that the observed light emission reflects a PB structure, which is characteristic of the REPEP.

In conclusion, we observed for the first time REPEP from a PhC using an electron beam running just above the PhC. The observed light emission spectrum consists of many sharp peaks. The rapid variation in the emission peaks with change in the direction of observation shows that the peaks indeed arise accompanying excitation of the PB modes. The excitation of the PB modes was also confirmed by comparison of experimentally obtained spectrum and the calculated one reflecting the PB structure.

We thank Mr. T. Tsutaya, Mr. N. Ohara, Mr. M. Kanbe, Dr. N. Horiuchi, and the staff of LNS, Tohoku University for their help in the experiment. The present work was supported by a Grant-In-Aid for Scientific Research and a Special Coordination Funds from the Ministry of Education, Culture, Sports, Science and Technology, Japan, and by the Special Postdoctoral Research Program of RIKEN, Japan.

REFERENCES

* Present address: Institute of Physics, University of Tsukuba, Tsukuba 305-8571, Japan.

[1] K. Ohtaka, Phys. Rev. B **19**, 5057 (1979).

[2] E. Yablonovitch, Phys. Rev. Lett. **58**, 2059 (1987).

[3] E. Yablonovitch and T. J. Gmitter, Phys. Rev. Lett. **63**, 1950 (1989).

[4] E. Yablonovitch, J. Phys.: Condens. Matter. **5**, 2443 (1993).

[5] K. Ohtaka and S. Yamaguti, Opt. Spectrosc. **91**, 506 (2001).

[6] K. Ohtaka and S. Yamaguti, Optics and Quantum Electronics **34**, 235 (2002).

[7] S. Yamaguti, J. Inoue, O. Haeberlé, and K. Ohtaka, Phys. Rev. B **66**, 195202 (2002).

[8] C. Luo, M. Ibanescu, S. G. Johonson, and J. D. Joannopoulos, Science **299**, 368 (2003).

[9] F. J. García de Abajo, A. G. Pattantyus-Abraham, N. Zabala, A. Rivacoba, M. O. Wolf, and P. M. Echenique, Phys. Rev. Lett. **91**, 143902 (2003).

[10] S. J. Smith and E. M. Purcell, Phys. Rev. **92**, 1069 (1953).

[11] G. Doucus, J. H. Mulvey, M. Omori, J. Walsh, and M. F. Kimmitt, Phys. Rev. Lett. **69**, 1761 (1992).

[12] The optical density of states (ODOS) spectrum of a PhC has fine structures reflecting the PB structure. The band widths of the fine structures in ODOS spectrum reflect Q values of the PBs. We confirmed by calculation (not shown) that the light emission intensity correlates quite well to the band widths of the fine structures in the ODOS spectrum of the PhC, which means that strong light emission results from the high Q values of PBs.

[13] T. Kondo, Thesis, Osaka University, Japan (2002).

[14] K. Ohtaka, Y. Suda, S. Nagano, and T. Ueta, A. Imada, T. Koda, J. S. Bae, K. Mizuno,

S. Yano, and Y. Segawa, Phys. Rev. B **61**, 5267 (2000).

[15] T. Kondo, M. Hangyo, S. Yamaguti, S. Yano, Y. Segawa, and K. Ohtaka, Phys. Rev. B **66**, 033111 (2002).

[16] O. Haeberlé, P. Rullhusen, J. -M. Salomé, and N. Maene, Phys. Rev. E **49**, 3340 (1994); **55**, 4675 (1997).

[17] Y. Shibata, S. Hasebe, K. Ishi, S. Ono, M. Ikezawa, T. Nakazato, M. Oyamada, S. Urasawa, T. Takahashi, T. Matsuyama, K. Kobayashi, and Y. Fujita, Phys. Rev. E **57**, 1061 (1998)

[18] K. Ohtaka, J. Phys. C **13**, 667 (1980).

[19] K. Ohtaka and Y. Tanabe, J. Phys. Soc. Jpn. **65**, 2265 (1996).

[20] Although we cannot clarify the origins of the peaks, which are absent in the calculated spectrum, we can speculate that these peaks also arise from the excitation of the photonic band modes. Some of the PBs and the $\mathbf{H}_{-1,0}$ line may cross at the energy of these peaks due to a slight difference in the PB structure from that is calculated. A possible reason of the change in the PB structures is slight deformation of the PhC sample.

[21] The difference in the emission intensity ratios among the peaks between the observed and calculated spectra might partly be caused by the damping effect due to the slight distortion of the PhC lattice structure. Since these modes are strongly confined and stay longer time within the PhC, they are affected more substantially by the damping effect while they stay within the PhC. According to our calculation, the sharp peaks are easily affected by the damping effect, and weaken their intensity. This may especially be the case for the peaks at around 100 GHz.

FIGURES

FIG. 1. (a) A picture of monolayer triangular lattice of PTFE spheres used in the present study as a PhC sample. The charge current, which is shown by a solid arrow, runs in the x direction. (b) Two basis vectors (K_1 and K_2) in the reciprocal lattice space of the PhC used in the present study. The Brillouin zone is enclosed by thick solid lines. (c) Illustration of the umklapp scattering process in the $((k_s)_x, \omega)$ plane. The dispersion line of the evanescent light (broken line) generated by the running charge goes into the light cone (shaded area) to become an $\mathbf{H}_{m,n}$ line (solid lines) by the umklapp momentum transfer in the course of the scattering (see the text). The dispersion curves of PBs are schematically shown by solid curves. The θ-constant spectra obtained in the experiment are the one along the dotted arrows in the $((k_s)_x, \omega)$ plane. The point of intersection between an $\mathbf{H}_{m,n}$ line and a PB dispersion curve and an observation line ($(k_s)_x = \frac{\omega}{c}\cos\theta_2$) is shown by an open circle. (d) Experimental setup. M1, M3: plane mirrors; M2: concave mirror; h: beam height. The position of mirror M1 can be changed from M1' to M1".

FIG. 2. Emission-angle (θ) dependence of the spectra of emitted light (panels (b) and (c)). The emission peaks on the $\mathbf{H}_{m,n}$ lines are indexed as (m, n) (see text). The dotted lines are guide to the eyes. For comparison, panel (a) shows the spectrum with no PhC.

FIG. 3. Contour map of the light emission intensity in the $((k_s)_x, \omega)$ plane. The dotted-broken lines show the boundary of the light cone. The dotted lines show the $\mathbf{H}_{-1,0}$, ((-1, 0)), the $\mathbf{H}_{-2,0}$, ((-2, 0)) and the $\mathbf{H}_{-3,0}$, ((-3, 0)) lines.

FIG. 4. Calculated PB structure of the single layer PTFE PhC (a), and comparison between the theoretical (b) and experimental (c) emission spectra. Dotted curves and a solid line in (a) correspond to the PBs and $\mathbf{H}_{-1,0}$ line, respectively. The emission spectra in (b) and (c) are those along $\mathbf{H}_{-1,0}$ line (see the text). As for the peaks indicated by crosses, see ref. 20.

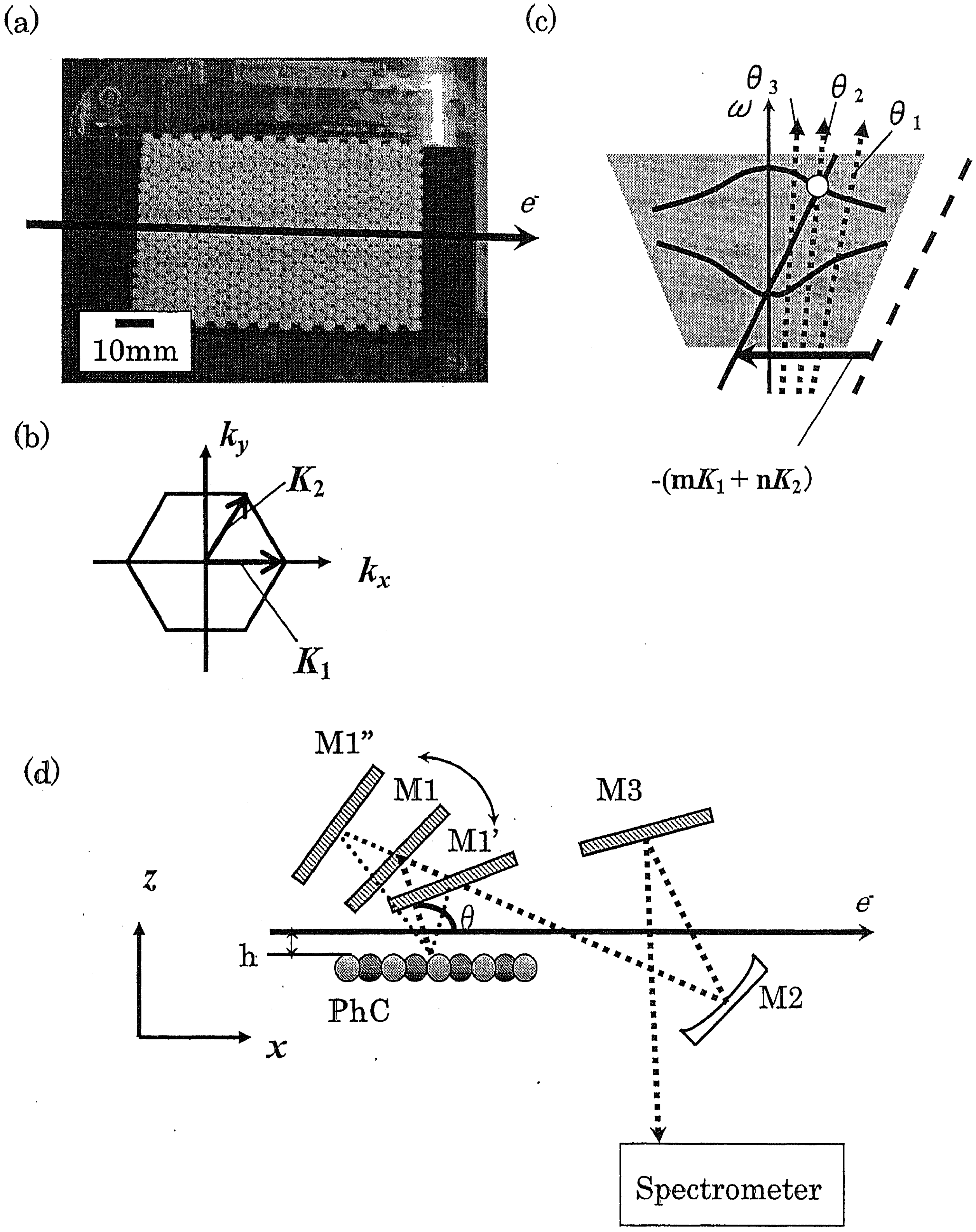

Fig. 1 K. Yamamoto *et al.*

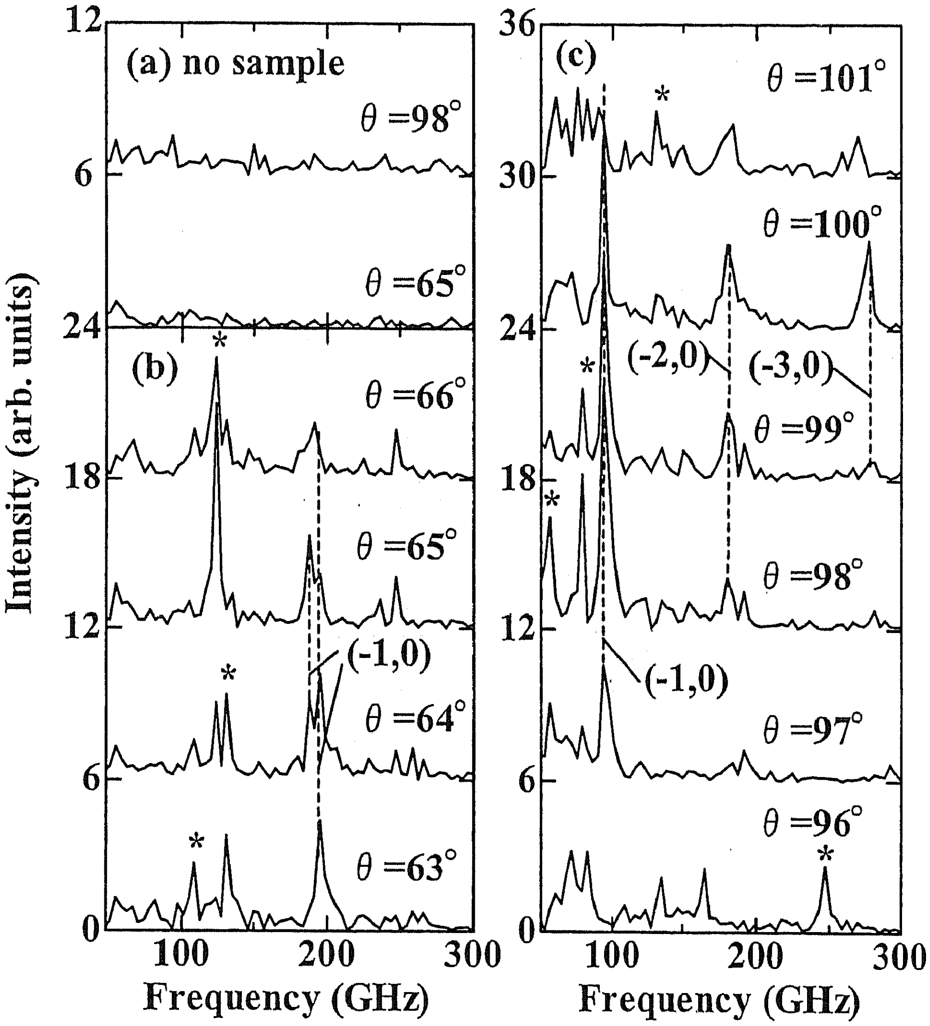

Fig. 2 K. Yamamoto *et al.*

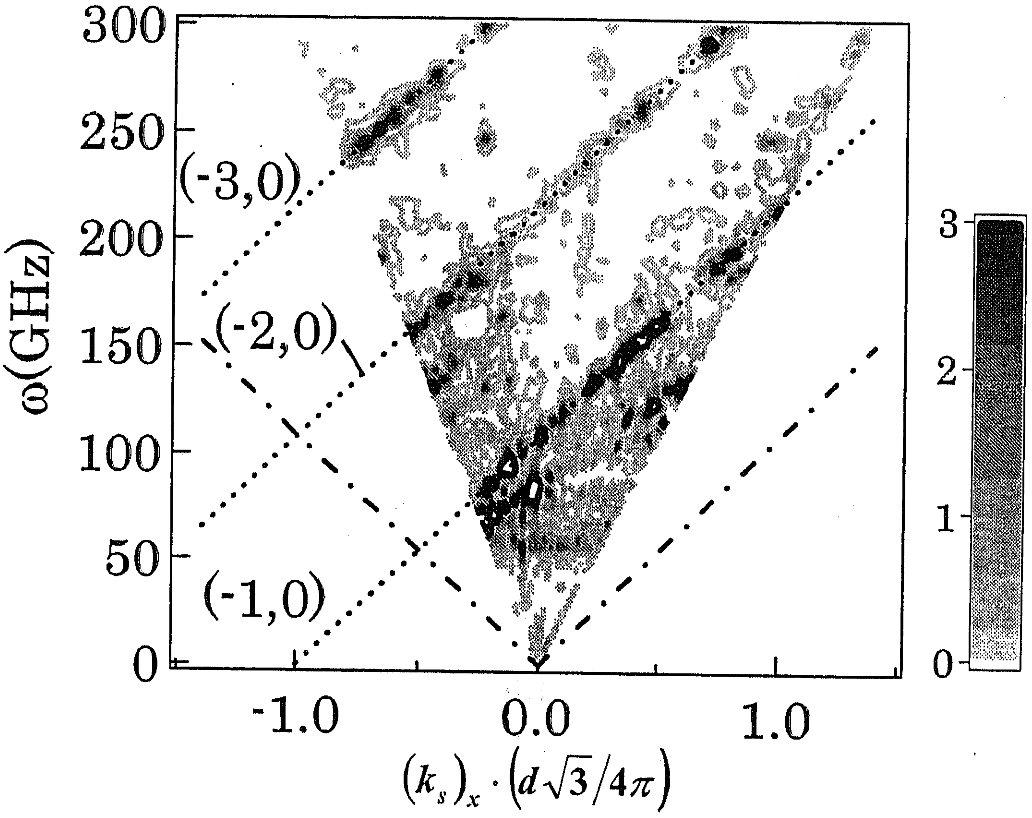

Fig. 3 K. Yamamoto *et al.*

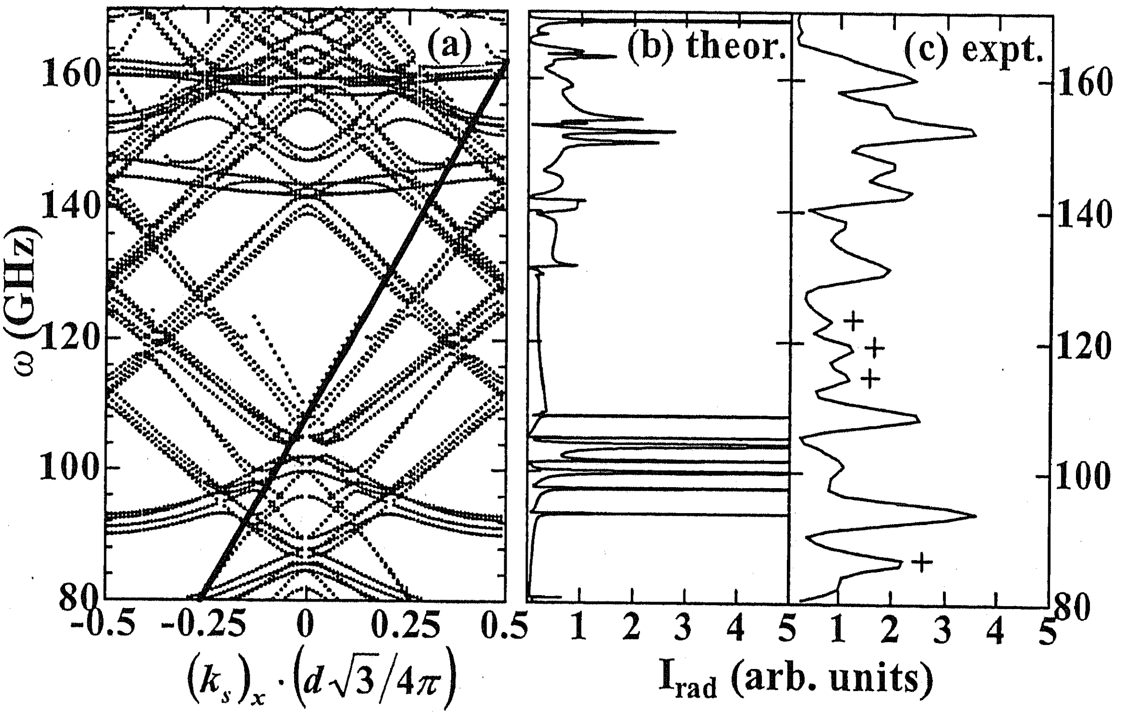

Fig. 4 K. Yamamoto *et al.*

Relativistic electron energy loss and induced radiation emission in two-dimensional metallic photonic crystals I: formalism and surface plasmon polariton

Tetsuyuki Ochiai and Kazuo Ohtaka
Center for Frontier Science, Chiba University, Chiba 263-8522, Japan
(Dated: March 5, 2004)

A fully relativistic description of the electron energy loss and the induced radiation emission in arbitrary arrays of non-overlapping metallic cylinders is presented in terms of the multiple scattering method on the basis of vector cylindrical waves. Numerical analysis is given for dilute and dense arrays of Aluminum cylinders with a nanoscale diameter. The results of the electron energy loss spectrum are well correlated with the dispersion relation of coupled surface plasmon polaritons, and can be interpreted with an effective medium approximation when the electron runs inside the arrays. In addition, the cavity modes localized in the grooves between the cylinders can affect strongly the electron energy loss spectrum.

PACS numbers: 42.70.Qs,73.20.Mf,34.50.Bw

I. INTRODUCTION

Recently, much interest has been attracted in optical properties of composite materials such as cluster of metallic nano-particles[1], photonic crystal[2,3], and left-handed material[4–6]. They have the potential ability to enhance various optical processes with their rich spectrum, and will be a key component of future optoelectronics devices. So far, their properties have been investigated mainly with far-field optical equipment. However, near-field responses of them are of great importance, because much information can be attained from the evanescent light involved in composite materials.

The electron energy loss (EEL) spectroscopy in a scanning transmission electron microscope is closely related to the near-field, and is a quite useful tool to investigate both bulk and surface excitations of samples. In a typical EEL experiment the kinetic energy of electron is on the order of 100 [keV], and a low-energy part of the EEL spectrum is related to a collective excitation such as surface plasmon. Thus, the spectrum is well interpreted in terms of a classical macroscopic theory on the basis of an effective dielectric function, taking account of geometry and anisotropy of samples. For instance, the EEL of a multi-wall fullerene can be well explained with an effective dielectric function of the corresponding Graphite sheets.[7]

There are extensive references on the EEL spectrum for various geometrical objects[8–11], though most works neglect the retardation effect. As for the composite materials, Maxwell-Garnett(MG)-type approximations have been widely used. In the last decade a remarkable progress has been made on this subject. Pendry et al. proposed a new theoretical method for the EEL of periodically arranged nano-structures[12] in terms of the real-space transfer matrix of the electro-magnetic wave.[13] García de Abajo et al. developed a multiple-scattering method for clusters of nano-particles, on the basis of vector spherical waves[14,15] and of the boundary element method.[16,17] These methods are very powerful and in principle can be adapted to various complex geometries. However, owing to the spatial discretization used in the transfer matrix method and in the boundary element method, the accuracy of the results reduces to some extent at high frequencies.

Here, we present a fully relativistic multiple-scattering approach focused on arrays of non-overlapping cylinders by using vector cylindrical waves. Though at present the method works only for the cylinders with isotropic dielectric functions, in principle it can work for anisotropic cylinders such as multi-wall carbon nano-tubes[18]. With this method the light scattering, as well as the EEL and the induced radiation emission in arbitrary arrays of non-overlapping cylinders can be treated in a unified manner by solving exactly the multiple-scattering equation. In addition, since the method utilizes the Fourier decomposition along the cylindrical axis, the local optical responses of a certain wave vector along the axis can be obtained. This property is feasible in order to see the effects of the localized electro-magnetic modes of cylinders in detail. We should note that our method is optimized for arrays of non-overlapping cylinders. In contrast to the methods based on the spatial discretization, it maintains high accuracy even at high frequencies. Though in this paper we restrict ourselves to the low-frequency region, we will deal with the high-frequency region in the paper II.[19]

A certain amount of the EEL in composite materials is caused by the induced radiation emission. As for a metallic nano-particle, this phenomenon is known as the surface plasmon radiation emission.[20] By arranging nano-particles periodically, so-called Smith-Purcell(SP) radiation[21,22] takes place. One of the authors (K.O.) and his collaborators have studied the SP radiation in the photonic crystals composed of dielectric spheres in detail, where a notable enhancement of the intensity of the SP radiation takes place owing to the singular state density of photon in the photonic crystals.[23–25] However, to the best of our knowledge, none has been reported concerning the radiation emission from arrays of cylinders. Thus, the quantitative evaluation of the radiation emission in the arrays is another theme of the paper.

On the other hand, the determination of the effective dielectric function of composite materials is still valuable at low frequencies. It gives a concise explanation of the absorption spectrum as well as the EEL spectrum of the composite materials in bulk.[26] Moreover, the determination is an important issue in the field of left-handed material, which has negative permittivity and permeability simultaneously. Several methods to determine them have been proposed by many authors.[27–29] Here, we propose an alternative method by using the scattering matrix of semi-infinite photonic crystals and compare the EEL in the effective medium with that of photonic crystal.

This paper deals mainly with the formalism of our method as well as the numerical analysis on clusters of Aluminum cylinders whose diameter is a few nanometers, bearing carbon nano-tube arrays in mind. In the paper II we will deal with a metallic photonic crystal whose lattice constant is comparable with the plasma wavelength of the constituent metallic cylinders. Since it is very bulky to present a comprehensive analysis on the EEL and the induced radiation emission in a single paper, we should discuss the above topics separately. In the nano-structures which are analyzed in this paper the relevant range in wavelength, which is near the surface plasma wavelength of metal, is much larger than the diameter and than the pitch of the structure. As a result, effects of usual photonic bands, which come from zone folding and lifting of degeneracy on Bragg planes, do not appear in the EEL spectrum and the induced radiation emission spectrum at relevant frequencies. In particular there is no remarkable feature in the SP radiation emission spectrum. Instead, unusual photonic bands of coupled surface plasmon polaritons have a strong influence on the EEL spectrum at very low frequencies. Moreover, in the relevant frequency range an effective medium approximation can be reasonably adapted to the structure. As for the structure which will be discussed in the paper II, we will show that effects of the usual photonic bands are very pronounced for the EEL and the induced radiation emission spectra.

The paper is organized as follows. In Sec.II we briefly summarize the vector cylindrical wave formalism. Using the formalism the dispersion relation of the surface plasmon polariton in an isolated metallic cylinder is obtained. The multiple scattering method is adapted to the EEL and the induced radiation emission in clusters of metallic cylinders in Sec.III. In Sec. IV the expression of the EEL in metallic photonic crystals is derived. The numerical results of the EEL spectrum are compared both with those of the isolated cylinder and with those of an effective homogeneous medium. Finally, we summarize the results.

II. SURFACE PLASMON POLARITON IN AN ISOLATED CYLINDER

An infinitely long metallic cylinder with a circular cross section can support an electro-magnetic surface-localized mode that is called surface plasmon polariton(SPP). The SPP is characterized by an angular momentum l, a wave number k_z, and an angular frequency ω, owing to the rotation invariance with respect to the cylindrical axis, the translational invariance along the axis, and the translational invariance of time, respectively. Before considering its dispersion relation, it is valuable to note some formulas of the light scattering by an isolated cylinder using vector cylindrical waves.[30] From now on, we take the cylindrical axis to the z-axis. Assume that a monotonic incident wave with a momentum k_z along the cylindrical axis is scattered by an isolated cylinder with a dielectric function $\varepsilon_a(\omega)$ and a radius r embedded in a host with a permittivity ε_b. Throughout the paper ε_b is taken to be 1 in numerical calculations, though we keep it unspecified in the following equations. The incident wave can be written as a superposition of vector cylindrical waves:

$$\mathrm{E}^0(\mathrm{x}) = e^{ik_z z}\left[\left(-\frac{1}{\lambda_b}\hat{z}\times\nabla_\parallel\right)\psi^{M,0}(\mathrm{x}) + \left(\frac{ik_z}{\lambda_b q_b}\nabla_\parallel + \frac{\lambda_b}{q_b}\hat{z}\right)\psi^{N,0}(\mathrm{x})\right], \quad (1)$$

$$\psi^{\beta,0}(\mathrm{x}) = \sum_l J_l(\lambda_b\rho)e^{il\theta}\psi_l^{\beta,0} \quad (\beta = M, N), \quad (2)$$

$$\lambda_b = \sqrt{q_b^2 - k_z^2}, \quad q_b = \sqrt{\varepsilon_b}\frac{\omega}{c}, \quad (3)$$

where c is the speed of light in vacuum, (ρ, θ, z) is the cylindrical coordinate, $\hat{z}$ is the unit vector along the z-direction, and $\nabla_\parallel$ is the differential operator with respect to (ρ, θ). In the present paper we take the following convention of the square root of a complex number: $\mathrm{Im}\sqrt{w} \geq 0$ for $\mathrm{Im}(w) \geq 0$. Sometimes, we call the M(N)-field the P(S) polarization. At $k_z = 0$ the M(N)-field corresponds to the TE(TM) polarization.

A metallic or dielectric cylinder scatters light irrespective of whether the light is evanescent or not. By imposing the boundary condition of Maxwell's equation, we can solve the scattering problem exactly. The induced wave scattered by the cylinder is given by

$$\mathrm{E}^{\mathrm{ind}}(\mathrm{x}) = e^{ik_z z}\left[\left(-\frac{1}{\lambda_b}\hat{z}\times\nabla_\parallel\right)\psi^{M,\mathrm{ind}}(\mathrm{x}) + \left(\frac{ik_z}{\lambda_b q_b}\nabla_\parallel + \frac{\lambda_b}{q_b}\hat{z}\right)\psi^{N,\mathrm{ind}}(\mathrm{x})\right], \quad (4)$$

$$\psi^{\beta,\mathrm{ind}}(\mathrm{x}) = \sum_l H_l(\lambda_b\rho)e^{il\theta}\psi_l^{\beta,\mathrm{ind}}, \quad (5)$$

$$\psi_l^{\beta,\mathrm{ind}} = \sum_{\beta'} t_l^{\beta\beta'}\psi_l^{\beta',0}. \quad (6)$$

Here, H_l is the Hankel function of first kind and $t_l^{\beta\beta'}$

is the *t-matrix* of the cylinder, its analytical expression being

$$\begin{pmatrix} t_l^{MM} & t_l^{MN} \\ t_l^{NM} & t_l^{NN} \end{pmatrix} = - \begin{pmatrix} d_l^{>MM} & d_l^{>MN} \\ d_l^{>NM} & d_l^{>NN} \end{pmatrix} \begin{pmatrix} d_l^{<MM} & d_l^{<MN} \\ d_l^{<NM} & d_l^{<NN} \end{pmatrix}^{-1}, \tag{7}$$

$$\begin{pmatrix} d_l^{>MM} & d_l^{>MN} \\ d_l^{>NM} & d_l^{>NN} \end{pmatrix} = \begin{pmatrix} \rho_b J_l'(\rho_a) J_l(\rho_b) - \rho_a J_l(\rho_a) J_l'(\rho_b) & l\frac{k_z}{q_a}(\frac{\rho_b}{\rho_a} - \frac{\rho_a}{\rho_b}) J_l(\rho_a) J_l(\rho_b) \\ l\frac{k_z}{q_b}(\frac{\rho_b}{\rho_a} - \frac{\rho_a}{\rho_b}) J_l(\rho_a) J_l(\rho_b) & \frac{q_a}{q_b}\rho_b J_l'(\rho_a) J_l(\rho_b) - \frac{q_b}{q_a}\rho_a J_l(\rho_a) J_l'(\rho_b) \end{pmatrix}, \tag{8}$$

$$\begin{pmatrix} d_l^{<MM} & d_l^{<MN} \\ d_l^{<NM} & d_l^{<NN} \end{pmatrix} = \begin{pmatrix} \rho_b J_l'(\rho_a) H_l(\rho_b) - \rho_a J_l(\rho_a) H_l'(\rho_b) & l\frac{k_z}{q_a}(\frac{\rho_b}{\rho_a} - \frac{\rho_a}{\rho_b}) J_l(\rho_a) H_l(\rho_b) \\ l\frac{k_z}{q_b}(\frac{\rho_b}{\rho_a} - \frac{\rho_a}{\rho_b}) J_l(\rho_a) H_l(\rho_b) & \frac{q_a}{q_b}\rho_b J_l'(\rho_a) H_l(\rho_b) - \frac{q_b}{q_a}\rho_a J_l(\rho_a) H_l'(\rho_b) \end{pmatrix}, \tag{9}$$

$$\rho_i = \lambda_i r \quad (i = a, b), \quad \lambda_a = \sqrt{q_a^2 - k_z^2}, \quad q_a = \sqrt{\varepsilon_a}\frac{\omega}{c}. \tag{10}$$

It should be emphasized that except for $k_z = 0$ or $l = 0$, the M(N) polarization mixes with the N(M) polarization in the induced wave. This property is quite distinct from the case of an isolated sphere, where the polarization mixing does not take place. In the light scattering by cylinder there is another distinct point from that by sphere. Since λ_b is the wave number in the (x, y) plane, the induced wave is evanescent when λ_b is pure imaginary. On the other hand the induced wave by the sphere behaves as $h_l(q_b|\mathbf{x}|)$, where h_l is the spherical Hankel function of first kind. This means that induced wave by the sphere is always real and has a net flux at $|\mathbf{x}| = \infty$ irrespective of whether the incident wave is evanescent or not.

Next, we focus on the SPP mode in an isolated metallic cylinder. The SPP mode is a real eigenmode in the cylinder and can exist without the incident light. Therefore, taking account of Eq.(6) the equation that determines the dispersion relation of the SPP is given by

$$\begin{pmatrix} t_l^{MM} & t_l^{MN} \\ t_l^{NM} & t_l^{NN} \end{pmatrix}^{-1} \begin{pmatrix} \psi_l^{M,\mathrm{ind}} \\ \psi_l^{N,\mathrm{ind}} \end{pmatrix} = 0. \tag{11}$$

Like as the SPP on a flat metal/air interface, whose dispersion relation is given by the pole of the interface S-matrix between the metal and air, the dispersion relation of the SPP in a metallic cylinder is given by the pole of the t-matrix. The above equation leads to the following secular equation:

$$\det \begin{pmatrix} d_l^{<MM} & d_l^{<MN} \\ d_l^{<NM} & d_l^{<NN} \end{pmatrix} = 0, \tag{12}$$

for the SPP mode with angular momentum l. Strictly speaking, we must say that the SPP mode is referred to the mode with pure imaginary λ_a, when the cylinder is of metal. The secular equation also determines the dispersion relation of the guided modes, in which λ_a is real and positive, when the cylinder is of dielectric.

For simplicity, from now on, we restrict our consideration to an Aluminum cylinder with diameter 2.5[nm], though the formalism presented in the paper can be adapted to any types of cylinders as long as an isotropic dielectric function of the cylinder is concerned. The dielectric function of the Aluminum can be approximated well with the Drude formula:

$$\varepsilon_a(\omega) = 1 - \frac{\omega_p^2}{\omega(\omega + i\eta)}, \tag{13}$$

$\hbar\omega_p$ and $\hbar\eta$ being 15[eV] and 1[eV], respectively. The small diameter of the cylinder is comparable with that of a carbon nano-tube and the plasma frequency is equal to 3.67×10^{15}[Hz] and to 82.7[nm] in terms of wavelength, which corresponds to ultra-violet light. Though the cylinder has a nano-scale diameter, it seems still reasonable to apply the macroscopic dielectric function to the cylinder.

In Fig.1 the dispersion relation of the SPP modes of the Aluminum cylinder is shown. In this case the SPP mode with $l = 0$, which is the solution of $d_0^{<NN} = 0$, is

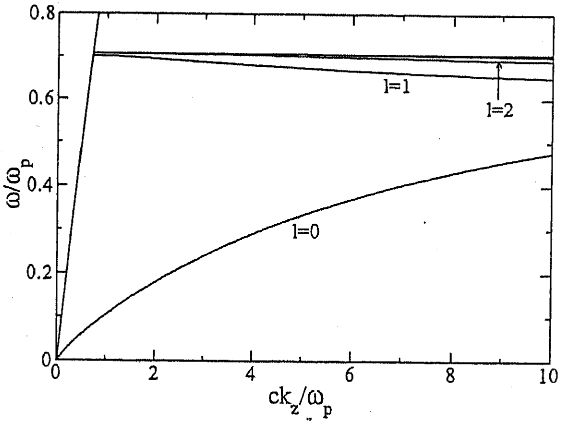

FIG. 1: The dispersion relation of the surface plasmon polariton of the Aluminum cylinder with diameter 2.5[nm] in air. The loss-less Drude dielectric function with $\hbar\omega_p = 15$[eV] was assumed for the Aluminum cylinder. The bold line is the light line $\omega = ck_z$.

quite distinct from those with $l \geq 1$. The mode with $l = 0$ ends at $\omega = 0$ and has positive slope in the (ω, k_z) space, whereas the other modes end at finite ω on the light line $\omega = ck_z$ and have negative slopes. As l increases, the dispersion curves approach to $\omega = \omega_p/\sqrt{2}$. Though the dispersion curves end on the light line, they can be extrapolated inside the light-cone. With this extrapolation we can understand how the SPP resonance occurs when real light is incident on the cylinder. The resonance also affects significantly the induced radiation emission when a charged particle passes near the cylinder.

III. ELECTRON ENERGY LOSS IN CLUSTER OF CYLINDERS

The formalism presented above serves to describe the EEL and the induced radiation emission when a charged particle runs near a cluster of cylinders. In this method the retardation effect is fully taken into account, though the recoil of the charged particle is neglected. In a typical EEL experiment the kinetic energy of the electron is about 100 [keV], whereas the total energy loss is less than 0.01% of it, so that the assumption of neglecting the recoil is fairly justified.

Let us consider a charged point particle with a charge e and a velocity v runs near the cluster composed of non-overlapping metallic cylinders aligned in the z-direction, whose positions are specified by two-dimensional (x and y) vector $\mathbf{x}_\alpha (\alpha = 1, 2, ..., N)$, N being the number of the cylinders. For simplicity, we assume that the charged particle does not penetrate any cylinders in the cluster and the trajectory of the particle is perpendicular to the cylindrical axes. Therefore, without losing generality, the position of the particle at time t is taken to $\mathbf{x}_t = (vt, y_0, z_0)$ in the Cartesian coordinate. As is known well, a running charged particle is accompanied by the electro-magnetic wave that is given by

$$\mathbf{E}^0(\mathbf{x}, \omega) = -\frac{\omega\mu_0 e}{2} \int \frac{dk_z}{2\pi} \epsilon^{\pm} e^{i\frac{\omega}{v}x + i\gamma|y-y_0| + ik_z(z-z_0)} \tag{14}$$

$$\epsilon^{\pm} = \begin{pmatrix} \frac{1}{\gamma}\left(1 - \frac{1}{q_b^2}(\frac{\omega}{v})^2\right) \\ \mp\frac{1}{q_b^2}\frac{\omega}{v} \\ -\frac{1}{q_b^2}\frac{\omega}{v}\frac{k_z}{\gamma} \end{pmatrix}, \tag{15}$$

$$\gamma = \sqrt{q_b^2 - (\frac{\omega}{v})^2 - k_z^2}, \tag{16}$$

in the time-Fourier component. Here, the superscript of ϵ is referred to the sign of $y - y_0$. If the light velocity in the background medium is smaller than v, the electro-magnetic wave becomes real, yielding the Cerenkov radiation. Here, we restrict ourselves to the region $v < c/\sqrt{\epsilon_b}$, so that the electro-magnetic wave is evanescent (γ is pure imaginary).

The above expression can be transformed into a linear combination of the vector cylindrical waves centered at $\mathbf{x} = \mathbf{x}_\alpha$ as

$$\mathbf{E}^0(\mathbf{x}, \omega) = \int \frac{dk_z}{2\pi} e^{ik_z(z-z_0)} \left[\left(-\frac{1}{\lambda_b}\hat{z} \times \nabla_\parallel\right) \psi_\alpha^{M,0}(\mathbf{x}) + \left(\frac{ik_z}{\lambda_b q_b}\nabla_\parallel + \frac{\lambda_b}{q_b}\hat{z}\right) \psi_\alpha^{N,0}(\mathbf{x})\right], \tag{17}$$

$$\psi_\alpha^{\beta,0}(\mathbf{x}) = \sum_l J_l(\lambda_b|\mathbf{x} - \mathbf{x}_\alpha|) e^{il\theta(\mathbf{x}-\mathbf{x}_\alpha)} \psi_{l,\alpha}^{\beta,0}, \tag{18}$$

$$\psi_{l,\alpha}^{M,0} = \frac{\mu_0 e\omega}{2} e^{i\frac{\omega}{v}x_\alpha \pm i\gamma(y_\alpha - y_0)} \left(\pm\frac{i}{\lambda_b}\right) i^l e^{-il\theta_{K^\pm}}, \tag{19}$$

$$\psi_{l,\alpha}^{N,0} = \frac{\mu_0 e\omega}{2} e^{i\frac{\omega}{v}x_\alpha \pm i\gamma(y_\alpha - y_0)} \left(\frac{k_z\omega}{q_b v\gamma\lambda_b}\right) i^l e^{-il\theta_{K^\pm}} \tag{20}$$

Here, $\theta_{K^\pm}$ is the argument of two-dimensional vector $K^\pm \equiv (\omega/v, \pm\gamma)$ for a real γ. In the case of a pure imaginary γ we must define $\theta_{K^\pm}$ as

$$e^{il\theta_{K^\pm}} = \left(\frac{\omega/v \pm i\gamma}{\lambda_b}\right)^l \tag{21}$$

Moreover, ± in Eq.(19) and (20) corresponds to the sign of $y_0 - y_\alpha$ and $\psi_{l,\alpha}^{\beta,0}$ is the multi-pole coefficient of the incident wave for cylinder α. We should note that the k_z integration is involved in Eq.(17). However, since k_z is a conserved quantity for the cluster, each cylindrical wave with fixed k_z is independently scattered by the cluster.

The incident evanescent wave is multiply scattered in the cluster of the cylinders. By using the multiple-scattering method, the induced radiation field is self-consistently determined as follows.[14] If we focus on cylinder α, the incident wave consists of the direct term (Eq.(17)) plus the sum of the induced wave scattered by another cylinder α'. Therefore, the induced wave from cylinder α is obtained by multiplying the t-matrix of cylinder α to the multi-pole components of the incident wave re-expanded around $\mathbf{x} = \mathbf{x}_\alpha$. As a result, the self-consistent induced wave is determined as

$$\mathbf{E}^{\text{ind}}(\mathbf{x}, \omega) = \int \frac{dk_z}{2\pi} e^{ik_z(z-z_0)} \left[\left(-\frac{1}{\lambda_b}\hat{z} \times \nabla_\parallel\right) \psi^{M,\text{ind}}(\mathbf{x}) + \left(\frac{ik_z}{\lambda_b q_b}\nabla_\parallel + \frac{\lambda_b}{q_b}\hat{z}\right) \psi^{N,\text{ind}}(\mathbf{x})\right], \tag{22}$$

$$\psi^{\beta,\text{ind}}(\mathbf{x}) = \sum_{l,\alpha} H_l(\lambda_b|\mathbf{x} - \mathbf{x}_\alpha|) e^{il\theta(\mathbf{x}-\mathbf{x}_\alpha)} \psi_{l,\alpha}^{\beta,\text{ind}}, \tag{23}$$

$$\psi_{l,\alpha}^{\beta,\text{ind}} = \sum_{\beta'} t_{l,\alpha}^{\beta\beta'} (\psi_{l,\alpha}^{\beta',0} + \sum_{l'} \sum_{\alpha' \neq \alpha} G_{l\alpha,l'\alpha'} \psi_{l',\alpha'}^{\beta',\text{ind}}), \tag{24}$$

$$G_{l\alpha,l'\alpha'} = H_{l'-l}(\lambda_b \rho_{\alpha\alpha'}) e^{i(l'-l)\theta_{\alpha\alpha'}}. \tag{25}$$

Here, $G_{l\alpha,l'\alpha'}$ is the propagator from cylinder α' to α, and in its expression $\rho_{\alpha\alpha'}$ and $\theta_{\alpha\alpha'}$ are the magnitude and the argument of $\mathbf{x}_\alpha - \mathbf{x}_{\alpha'}$, respectively.

As was mentioned in Sec. II, the induced wave contains propagating components with real λ_b, which have a net flux at $\rho \to \infty$. This implies that a radiation emission takes place when a charged particle passes near the cluster. As a result, the charged particle losses its energy via the emission. In addition, if the cylinders are lossy having positive imaginary part in $\varepsilon_a(\omega)$, a part of the energy is absorbed in the cylinders. The total energy loss is then the sum of the radiation emission and the absorption. Qualitatively, the loss can be calculated with the exerted force by the induced field reacting on the particle. Thus, its expression is given by

$$P_{el}(\omega) = -\frac{e}{2}\mathrm{Re}\int dt e^{-i\omega t}\mathbf{v}\cdot\mathbf{E}^{\mathrm{ind}}(\mathbf{x}_t,\omega) \tag{26}$$

per unit angular frequency. The integral over t yields

$$P_{el}(\omega) = \int \frac{dk_z}{2\pi}P_{el}(\omega,k_z), \tag{27}$$

$$P_{el}(\omega,k_z) = -e\sum_{l,\alpha}\mathrm{Re}\Big[e^{-i\frac{\omega}{v}x_\alpha \pm i\gamma(y_0-y_\alpha)} \times (-i)^l e^{il\theta_{K\pm}}\left(\pm\frac{i}{\lambda_b}\psi_{l,\alpha}^{M,\mathrm{ind}} - \frac{k_z\omega}{vq_b\lambda_b\gamma}\psi_{l,\alpha}^{N,\mathrm{ind}}\right)\Big] \tag{28}$$

Here, ± in the above equation is referred as the sign of $y_0 - y_\alpha$.

On the other hand the net flux of the induced radiation emission is obtained by

$$P_{em}(\omega) = \lim_{\rho\to\infty}\frac{1}{2}\int dz d\theta\rho \tag{29}$$

$$\times\mathrm{Re}\left[(\mathbf{E}^{\mathrm{ind}}(\mathbf{x},\omega))^* \times \mathbf{H}^{\mathrm{ind}}(\mathbf{x},\omega)\right]\cdot\hat{\rho}. \tag{30}$$

per unit angular frequency. Using the asymptotic form of the induced field (Eq.(22)), the net flux turns out to be

$$P_{em}(\omega) = \int_{-q_b}^{q_b}\frac{dk_z}{2\pi}P_{em}(\omega,k_z), \tag{31}$$

$$P_{em}(\omega,k_z) = \frac{\lambda_b}{2\mu_0\omega}\int d\theta(|f^M(\theta)|^2 + |f^N(\theta)|^2) \tag{32}$$

$$f^\beta(\theta) = \sqrt{\frac{2}{\pi\lambda_b}}\sum_{l,\alpha}e^{-i\lambda_b\hat{\rho}\cdot\mathbf{x}_\alpha + il\theta}(-i)^{l+1}\psi_{l,\alpha}^{\beta,\mathrm{ind}}. \tag{33}$$

The cutoff of the k_z integral comes from the fact that the scattered wave becomes evanescent when $|k_z| > q_b$. If there is no absorption in the cylinder, the energy loss must be equal to the net flux of the radiation emission, that is,

$$P_{el}(\omega,k_z) = P_{em}(\omega,k_z). \tag{34}$$

This equality serves as a criterion of the correctness and the convergence of numerically calculated EEL spectrum.

In the case of an isolated cylinder, the integration over θ in Eq.(32) can be performed analytically, yielding

$$P_{em}(\omega,k_z) = \frac{2}{\mu_0\omega}\sum_{l\beta}|\sum_{\beta'}t_l^{\beta\beta'}\psi_l^{\beta'0}|^2. \tag{35}$$

First of all, let's consider the EEL in the isolated Aluminum cylinder. The EEL spectrum of the cylinder has a sequence of peaks at the frequencies of the SPP modes. This is because the t-matrix has a SPP pole on the real axis in the complex plane of ω as can be understood in Eq.(7) and (12). To see the correspondence of the dispersion relation of the SPP, Fig.2 shows the integrand $P_{el}(\omega,k_z)$ of the EEL spectrum, changing the k_z value from 0 to 10 in units of ω_p/c. Here, the velocity and the impact parameter of the charged particle were taken to 0.4c and $2r$, respectively. One can find the main EEL peak appears near $\omega = \omega_p/\sqrt{2}$, where the SPP bands with $l \geq 1$ exist. In contrast to the fine structure of these bands in Fig.1, no fine structure can be observed in the peak. This is a direct consequence of rather large imaginary part in the dielectric function of Aluminum, which yields a broadening and mixing of the SPP bands with $l \geq 1$. The peak frequency decreases with increasing k_z, reflecting the negative slopes of these bands. In addition to the main EEL peak another EEL peak appears much below $\omega = \omega_p/\sqrt{2}$. This peak comes from the SPP mode with $l = 0$, as can be understood clearly by comparing with the dispersion relation of the SPP mode with $l = 0$. In fact the peak frequency increases quite remarkably with increasing k_z, tracing the dispersion curve of the SPP with $l = 0$. As a general tendency, $P_{el}(\omega,k_z)$ decreases with increasing $|k_z|$.

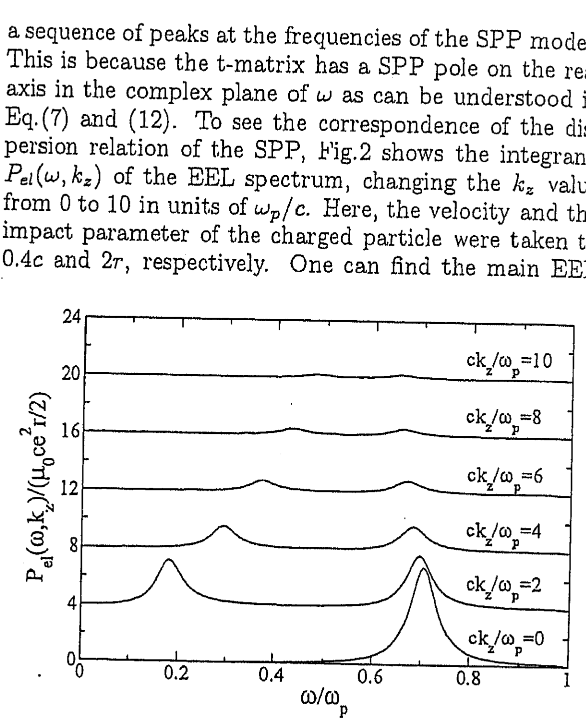

FIG. 2: The electron energy loss spectrum in an isolated Aluminum cylinder with diameter $2r$ = 2.5[nm]. The spectrum is given in units of $\mu_0 ce^2 r/2$ and consecutive curves are shifted 4 (in the same units) upward for readability. The velocity of the charged particle was taken to be v = 0.4c. The impact parameter, i.e., the distance between the cylindrical axis and the trajectory of the charged particle, is 2.5[nm].

Next, we consider how the imaginary part affects the percentage of the radiation emission in the EEL. To this end, we show in Fig.3 the integrated EEL spectrum $P_{el}(\omega)$ and the integrated radiation emission spectrum $P_{em}(\omega)$ at η=0,1[eV]. At η = 0 these must coincide. As can be seen, when the imaginary part in ε_a is introduced, the radiation emission spectrum is almost unchanged from that in the loss-less cylinder except for the SPP frequency region. However, the EEL spectrum

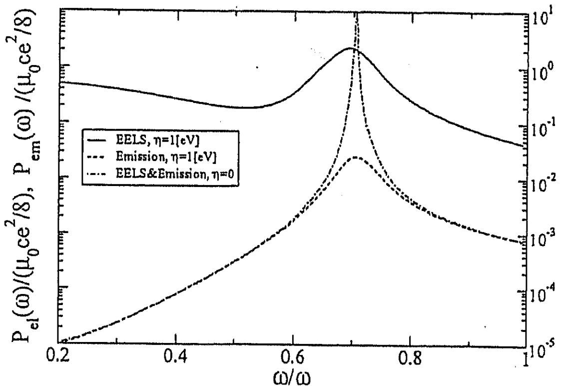

FIG. 3: The integrated EEL and the radiation emission spectra in the isolated Aluminum cylinder. The same parameters as for Fig.2 were used.

receives a drastic change. According to the figure, the EEL is dominated by the absorption in the cylinder under study. Therefore, the efficiency for converting the kinetic energy of the charged particle to the radiation via surface plasmon is very low.

Finally, we consider how the spectra change when another cylinder is added. In this case, the multiple-scattering of the induced radiation significantly affects the spectra. As we will see, almost touched metallic cylinders causes a drastic change in the spectra as well as in the near-field configuration. This phenomena is closely related to the surface-enhanced Raman scattering,[31–34] in which the intensity of the induced electro-magnetic field is enhanced more than thousand times as large as that of the incident intensity. As an example, we explored the EEL for various spatial arrangements of the two identical Aluminum cylinders. Fig.4 shows the EEL spectra $P_{el}(\omega, k_z)$ with $k_z = 0$ corresponding to the arrangements shown in the insets. In (a) and (b) the two-cylinders are well-separated, the distance between the two cylindrical axes being $4r$ ($r = 1.25$[nm]), whereas in (c) and (d) they are very close to each other, the distance being $2.16r$. The distance between the two cylindrical axes and the trajectory of the charged particle is $2r$ in (a) and (b), and is $1.08r$ in (c) and (d). As expected, if the two cylinders are well separated along the trajectory (case (a)), the EEL spectrum per cylinder has a single peak near $\omega = \omega_p/\sqrt{2}$, though an asymmetry of the peak is observed. In case (b) the two cylinders are separated along the normal direction of the trajectory. This geometry still yields a single peak in the EEL spectrum at $\omega \simeq \omega_p/\sqrt{2}$. Since there is the parity symmetry with respect to the trajectory, No electro-magnetic modes with the odd parity is involved in case (b). On the other hand, if the two cylinders are very close to each other, several loss peaks appear at the frequencies far from $\omega_p/\sqrt{2}$. In particular, the spectrum of the case (d) has two marked peaks at $\omega/\omega_p \simeq 0.52$ and 0.84. The latter peak is shared also by case (c). The peak at $\omega/\omega_p \simeq 0.52$ is related to the weakly resonant cavity modes localized in the groove between the two cylinders. To confirm this, we show the field intensity $|H_z(\mathrm{x})|^2$ at the peak frequency in Fig.5. In the figure we can see clearly that the peak is caused by the cavity mode in the groove. As for the peak at $\omega/\omega_p \simeq 0.84$ we couldn't find a clear evidence of the resonant cavity mode, as the field intensity at the peak frequency has another local maximum at a boundary of the cylinder beside that in the grooves. This feature suggests that this peak to be caused by a strong mixing of a cavity mode and the SPP modes. If the electron runs across the groove of the almost touched cylinders (case (c)), the peak at $\omega \simeq 0.52\omega_p$ disappears owing to the symmetry mismatch and the peak at $\omega \simeq 0.84\omega_p$ receives an enhancement.

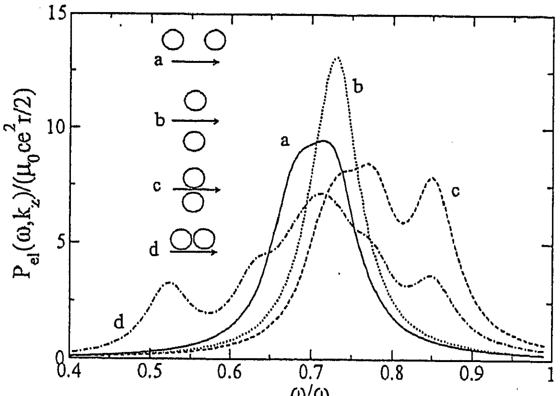

FIG. 4: The EEL spectra in the two identical Aluminum cylinders with various spatial arrangements shown in the insets. $k_z = 0$ was assumed. See text for the other parameters.

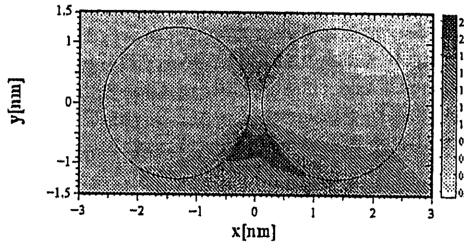

FIG. 5: The field intensity $|H_z(\mathrm{x})|^2$ induced by a running charged particle whose velocity is $0.4c$ is plotted at $(k_z, \omega) = (0, 0.523\omega_p)$, where a peak is observed in the EEL spectrum. The solid line stands for the edges of the two cylinders. The trajectory of the charged particle is at $y = -1.35$[nm].

Regarding the radiation emission spectrum in the two cylinders, its features are more or less similar to those in Fig.4, though the magnitude of $P_{em}(\omega, k_z)$ is much smaller than that of $P_{el}(\omega, k_z)$.

IV. ELECTRON RUNNING OUTSIDE PHOTONIC CRYSTAL

A photonic crystal that consists of a periodic array of metallic cylinders has a rich spectrum in it, including infinite SPP bands for the TE polarization[35,36] and a low-frequency cutoff for the TM polarization.[37] Combining these properties with a running charged particle, the system can react as a novel light emitter. In fact, when a charged particle passes near the photonic crystal, it induces the emission of real photon as was first pointed out by Smith and Purcell for a metallic grating.[21] In the photonic crystal, this phenomenon can be interpreted in two ways. One interpretation is as follows. The incident evanescent wave from the charged particle acquires an Umklapp momentum transfer in the photonic crystal, thereby coming into the light cone in the $(\omega, k_\parallel)$ space, $k_\parallel$ being the wave vector parallel to the boundary of the photonic crystal. As a result, real photon is emitted from the photonic crystal. The other interpretation is to regard the phenomena as a coherent radiation emission from different cylinders. Though these two interpretations are equivalent, the two points of view give us a deep insight of the Smith-Purcell(SP) radiation in the photonic crystal.

In the case of an isolated cylinder, the induced radiation emission is possible when $q_b^2 > k_z^2$, i.e.,when the emitted light is inside the light cone of the (ω, k_z) space. On the other hand, the condition that the evanescent light turns out to be a real photon via the Umklapp momentum transfer in the photonic crystal is given by

$$q_b^2 - k_z^2 - (\frac{\omega}{v} - n\frac{2\pi}{a})^2 > 0, \tag{36}$$

a being the pitch of the photonic crystal. Therefore, the allowed frequency range of the SP radiation is

$$\tilde{\omega}_- < \tilde{\omega} < \tilde{\omega}_+, \quad \tilde{k_z}^2 < \frac{n^2\varepsilon_b}{(\frac{c}{v})^2 - \varepsilon_b}, \tag{37}$$

$$\tilde{\omega}_\pm = \frac{n\frac{c}{v} \pm \sqrt{n^2\varepsilon_b - ((\frac{c}{v})^2 - \varepsilon_b)\tilde{k_z}^2}}{(\frac{c}{v})^2 - \varepsilon_b}, \tag{38}$$

where $\tilde{\omega} = \omega a/2\pi c$ and $\tilde{k_z} = k_z a/2\pi$. If the above condition is not satisfied in the light cone, a destructive interference among the induced radiation fields from different cylinders occurs, leading to the prohibition of the radiation emission. This also implies that if there is no absorption in the photonic crystal, the concerned range in the (ω, k_z) space does not contribute to the EEL in the photonic crystal. The phase diagram of the radiation emission at $v = 0.4c$ is shown in Fig.6. In Fig.6 the SP radiation is allowed in the shaded region. The allowed region has the low-frequency cutoff which increases with increasing v value. Beside, in the allowed region of the SP radiation the photonic density of state is in general singular including the Van Hove singularity. Therefore, we may expect a quite rich spectrum of the SP radiation in the photonic crystals.

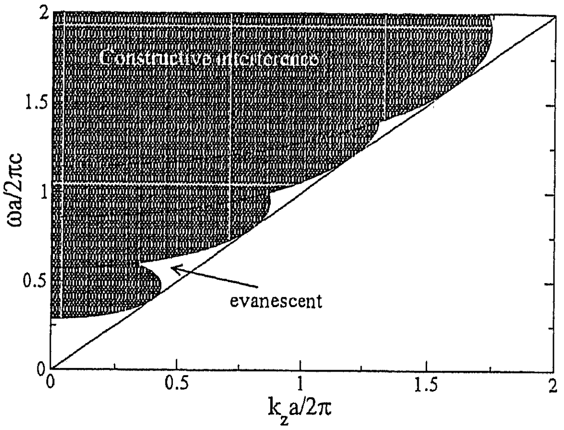

FIG. 6: The phase diagram of the induced radiation emission in a periodic array of cylinders with lattice constant a is shown. The Smith-Purcell radiation is possible only in the shaded region of the (k_z, ω) plane. The velocity of the charged particle was taken to be $v = 0.4c$. The solid line is the light line $\omega = ck_z$.

The rich spectrum is not limited in the SP radiation. We should mention that the photonic band structure exists also outside the shaded region of Fig.6. As long as the imaginary part in ϵ_a is non-zero, the absorption of the induced radiation is inevitable in the photonic crystal. This causes the EEL outside the shaded region, and the EEL is affected significantly by the photonic band structure therein. Inside the shaded region the EEL consists of the radiation emission and the absorption, and they are independent physical observables.

Like as in the case of cluster of cylinders, the EEL and the SP radiation in the photonic crystals can be treated in a unified framework with the multiple-scattering method on the basis of vector cylindrical waves. Pendry and Martin-Moreno presented for the first time an unified framework in terms of the transfer matrix method to argue the EEL and the SP radiation in photonic crystals.[12], The method is based on a discretization of Maxwell's equation on a spatial mesh in order to obtain the real-space transfer matrix.[13] They found that the scattering matrix, which is obtained from the transfer matrix, is directly related to the EEL and SP radiation spectra. Their algorithm is easily adapted to the two-dimensional counterpart[30,38,39] of the layer Korringa-Kohn-Rostoker-Ohtaka (KKRO) method[40–45], which is a generalization of the multiple scattering method to periodic systems. The layer-KKRO method has very high accuracy for the photonic crystal under consideration. We should note that the three-dimensional layer-KKRO method was already used for discussing the EEL and the SP radiation in three-dimensional photonic crystals composed of spheres.[23–25,46]

Let's assume that a running charged particle passes outside a finite-thick photonic crystal composed of a periodic array of the Aluminum cylinders. The particle runs with distance s from the boundary ($y = y_{\rm in}$) parallel to the (1,0) direction of the square lattice. Here, we take the x axis to be parallel to the (1,0) direction. A schematic illustration of the system under study is shown in Fig.7. In this case the induced radiation field in the outer region of the photonic crystal including the particle trajectory is given by

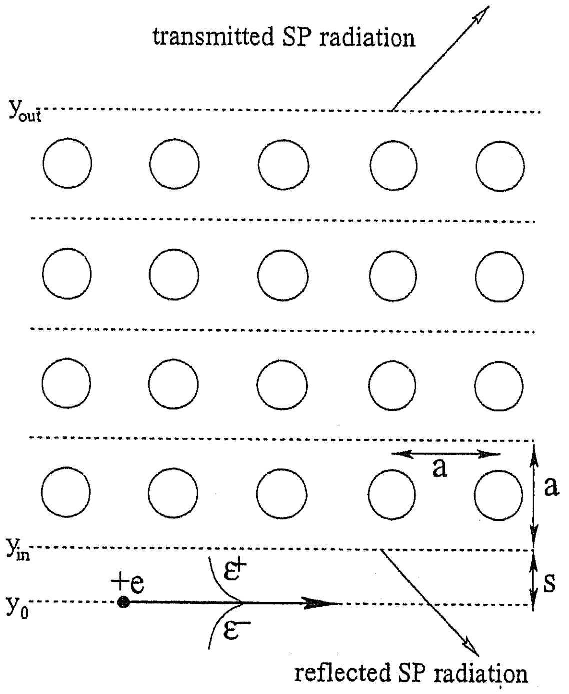

FIG. 7: A charged particle runs with distance s from the boundary of the finite-thick photonic crystal, which is composed of a square array of cylinders with pitch a. The polarization vector of the evanescent wave accompanied by the charged particle is denoted by $\epsilon^{\pm}$.

$$\mathbf{E}^{\rm ind}(\mathbf{x},\omega) = -\frac{\mu_0 e\omega}{2}\sum_h \int \frac{dk_z}{2\pi} e^{i\mathbf{K}_h^-\cdot(\mathbf{x}-\mathbf{x}_{\rm in})} \times Q_{-+}(h,h_0)\epsilon^+ e^{i\gamma_{h_0}s}, \tag{39}$$

$$\mathbf{K}_h^{\pm} = (k_x + h, \pm\gamma_h, k_z), \tag{40}$$

$$\frac{\omega}{v} = k_x + h_0, \tag{41}$$

$$\gamma_h = \sqrt{q_b^2 - (k_x+h)^2 - k_z^2}, \tag{42}$$

where $Q_{\pm\pm}(h,h')$, which has spatial tensor index, is the scattering matrix of the photonic crystal,[30] k_x is the Bloch momentum in the irreducible surface Brillouin zone associated with the boundary, $h(= 2\pi\mathrm{Z}/a)$ is a reciprocal lattice vector, and $\mathbf{x}_{\rm in} = (0, y_{\rm in}, z_0)$ in the Cartesian coordinate. In the opposite outer region of the photonic crystal the induced radiation field (transmitted SP radiation in Fig.7) is given by

$$\mathbf{E}^{\rm ind}(\mathbf{x},\omega) = -\frac{\mu_0 e\omega}{2}\sum_h \int \frac{dk_z}{2\pi} e^{i\mathbf{K}_h^+\cdot(\mathbf{x}-\mathbf{x}_{\rm out})} \times Q_{++}(h,h_0)\epsilon^+ e^{i\gamma_{h_0}s}, \tag{43}$$

where $\mathbf{x}_{\rm out} = (0, y_{\rm out}, z_0)$, $y_{\rm out}$ being the y-coordinate of the upper boundary. Quantitatively, the EEL per unit length of the particle trajectory is expressed by the following equation:

$$P_{el}(\omega,k_z) = \frac{1}{4}\mu_0 e^2\omega e^{-2|\gamma_{h_0}|s} \times|\gamma_{h_0}|\mathrm{Im}\left[(\epsilon^+)^\dagger Q_{-+}(h_0,h_0)\epsilon^+\right]. \tag{44}$$

On the other hand the SP radiation spectrum per unit length is given by

$$P_{em}(\omega,k_z) = \frac{1}{8}\mu_0 e^2\omega e^{-2|\gamma_{h_0}|s} \times\sum_{h\in\mathrm{open}} \gamma_h(|Q_{++}(h,h_0)\epsilon^+|^2 + |Q_{-+}(h,h_0)\epsilon^+|^2) \tag{45}$$

where the summation is taken over the open diffraction channels.

If the cylinders are loss-less in the photonic crystal, again $P_{el}(\omega,k_z) = P_{em}(\omega,k_z)$. This can easily be confirmed by considering flux conservation of through the photonic crystal:

$$\sum_{h\in\mathrm{open}} \gamma_h\left(|Q_{++}(h,h_0)\epsilon^+|^2 + |Q_{-+}(h,h_0)\epsilon^+|^2\right) = 2|\gamma_{h_0}|\mathrm{Im}\left[(\epsilon^+)^\dagger Q_{-+}(h_0,h_0)\epsilon^+\right] \tag{46}$$

Here, we study two kinds of metallic photonic crystals. One is a dilute photonic crystal that is composed of the square array of the Aluminum cylinders with the lattice constant $a = 4r = 5$[nm]. The other is its dense version which corresponds to the cases (c) and (d) of the coupled two cylinders treated in the last section ($a = 2.16r = 2.7$[nm]). The photonic band structures of these photonic crystals at $k_z = 0$ projected on the surface Brillouin zone associated with the boundary parallel to the (1,0) direction of the square lattice are shown in Fig.8. The band structures were calculated by using the two-dimensional layer-KKRO method taking $l_{\rm max} = 5$ and 12 in the dilute and dense photonic crystals, respectively. Here, we dropped the band diagram of the S(TM)-polarization, because it is not relevant to our problem. However, at non-zero k_z we must take account of both the S and P polarizations.

In both the photonic crystals the plasma frequency of the cylinder is much smaller than the lattice scale, so that the photonic band structure is very close to that of the empty lattice at high frequencies. However, below

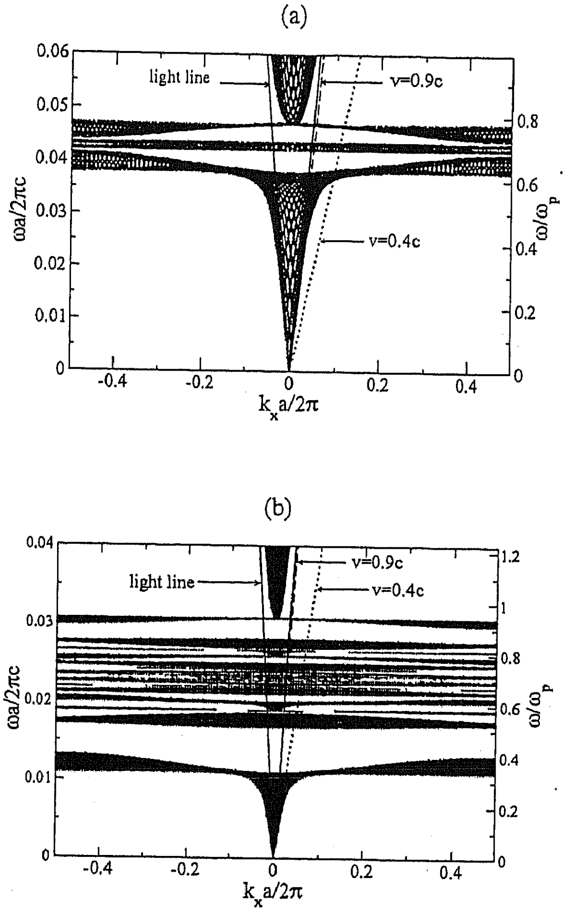

FIG. 8: The photonic band structure of the square lattice of the loss-less (i.e. $\eta = 0$) Aluminum cylinders at $k_z = 0$ was projected on the surface Brillouin zone associated with the boundary parallel to the (1,0) direction of the square lattice. In (a) the cylinders are well separated(lattice constant $a = 4r$=5[nm]), whereas in (b) the cylinders nearly touch($a = 2.16r$=2.7[nm]).

$\omega = \omega_p$ many flat bands which characterize the metallic photonic crystals appear. These bands are generally anisotropic, reflecting the C_{4v} symmetry of the square lattice, and have a singular state density. In the dilute photonic crystal, many bands are concentrated near $\omega = \omega_p/\sqrt{2}$. This indicates that they are merely a tight-binding coupling of the SPP of the isolated cylinder. In principle, we can find infinite numbers of the flat bands around $\omega = \omega_p/\sqrt{2}$, and they are quite difficult to distinguish. On the other hand, in the dense photonic crystal the flat bands are diverse in frequency, whereas their center is still at $\omega = \omega_p/\sqrt{2}$. Some of the bands are originated from the cavity mode localized in the groove of the two cylinders. However, most flat bands are considered to be related with the SPP of an Aluminum cylinder.

In Fig.8 the dispersion line of the radiation involved in the EEL, i.e., $\omega = v(k_x + h)$ (which is referred to as the v line) as well as the light line $\omega = \pm ck_x$ are also shown. Here, v is assumed to be either $0.4c$ or $0.9c$ and h is taken to be 0. In the frequency range concerned only the line with $h = 0$ is relevant, because the threshold of the SP radiation occurring along the v line of $h = 2\pi/a$ is rather high ($\tilde{\omega}_- \simeq 0.286$ and 0.474 in Eq.(38) for $v = 0.4c$ and $0.9c$, respectively). As a result, the EEL is caused solely by the absorption in the frequency range concerned. When the v line meets the shaded region of the projected band diagram, the charged particle can excite an eigenmode in the photonic crystal and thus causes an enhanced absorption loss in EEL. Strictly speaking, the projected band scheme should be used to understand the feature of the photonic crystal with infinite thickness along the $\Gamma - X$ direction. Since we are considering a finite-thick photonic crystal, the shaded region in Fig.8 must be regarded as a set of the dispersion curves of the eigenmodes in the finite-thick photonic crystal. Apparently, as the thickness increases, the dispersion curves fills up with the shaded region.

Fig.9 shows $P_{el}(\omega, k_z)$ with $k_z = 0$ of the two photonic crystals, varying number of layers. The velocity of the charged particle was taken to $0.4c$ and the parameter s was taken to zero. Concerning the dilute photonic crystal, the EEL spectrum has the double peaks near $\omega = \omega_p/\sqrt{2}$ in the mono-layer case. This feature already appeared in the result of the two separated cylinders (see Fig.4), where an asymmetry of the loss peak is observed. As the number of layers increases, the double peaks disappear and the spectrum converges to a certain function which has single peak near $\omega = \omega_p/\sqrt{2}$. The converged spectrum is not so far from the EEL spectrum of the isolated cylinder in which the single peak is found at $k_z = 0$. These features are consistent with the numerical results on the projected band structure (Fig.8): The v line of $v = 0.4c$ hits only the flat bands near $\omega = \omega_p/\sqrt{2}$. As in the isolated cylinder, we can infer that the single peak in the EEL spectrum is caused by the broadening and mixing of the flat bands owing to the non-zero imaginary part in ε_a.

As for the dense photonic crystal, there are several loss peaks whose positions change as the number of layers increases. Compared with the case of coupled two cylinders, the peak positions of the EEL spectrum in the photonic crystal are well correlated with those of case (d) of Fig.4. In particular, the two peaks at $\omega \simeq 0.55\omega_p$ and $0.82\omega_p$ at $N = 32$ are of reminiscences of those in case (d), and the corresponding flat bands, which have relatively large widths in frequency, can be observed in Fig.8(b). Again, above $\omega a/2\pi c \simeq 0.01$ the EEL spectrum converges to a certain function with increasing number of layers, though the convergence progresses slowly compared with that in the dilute photonic crystal. A remarkable feature in this case appears below $\omega a/2\pi c = 0.01$, where a frequency shift of a small loss peak is observed with increasing N. In contrast to the dilute photonic crystal, in such low frequency region the v line lies in the shaded region of the lowest band even for $v = 0.4c$,

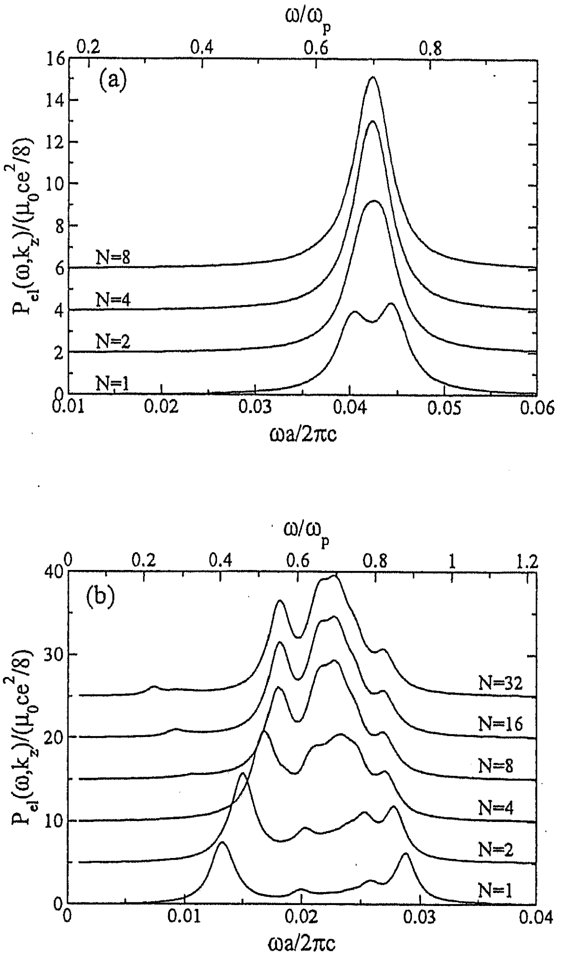

FIG. 9: The EEL spectrum of the photonic crystals at $k_z = 0$, varying the number of layers. The velocity of the charged particle was taken to $v = 0.4c$. In (a) the cylinders are well separated(lattice constant $a = 4r$), whereas in (b) the cylinders nearly touch($a = 2.16r$). The trajectory of the charged particle is just on the boundary of the photonic crystal (i.e. $s = 0$). Consecutive curves are shifted $2 \times \mu_0 ce^2/8$ and $5 \times \mu_0 ce^2/8$ upward in (a) and (b), respectively.

as can be seen in Fig.8. This band does not originate from the SPP modes, and thus the loss peaks found below $\omega a/2\pi c = 0.01$ is different in feature from that by the SPP bands.

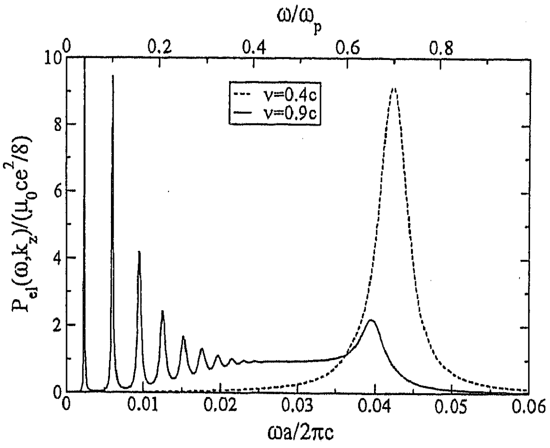

FIG. 10: The EEL spectrum of the dilute photonic crystal having 256 layers at $k_z = 0$. The velocity of the charged particle was taken to 0.4c (dashed line) and 0.9c (solid line).

The effects of the lowest band in the EEL spectrum can be clearly demonstrated in the dilute photonic crystal with large thickness, using a charged particle impinging with such high-speed that the v line is in the lowest band in Fig.8(a). Fig.10 shows the two EEL spectra of $v = 0.4c$ and $0.9c$ in the dilute photonic crystal having 256 layers. As can be seen in the figure, the lowest band causes very sharp loss peaks whose positions are distributed below $\omega a/2\pi c \simeq 0.025$. In order to understand this feature, we must remark that outside the light cone the band becomes the set of the guided modes in the corresponding finite-thick photonic crystal. Moreover, as mentioned later, we can reasonably introduce an effective dielectric function $\varepsilon_{\rm eff}(\omega)$, which is very close to that of Maxwell-Garnett,[27] to the photonic crystal under consideration. The effective dielectric function of Maxwell-Garnett is given by

$$\varepsilon_{\rm eff}^{\rm MG}(\omega) = \varepsilon_b \left(1 + \frac{2f\alpha}{1-f\alpha}\right), \tag{47}$$

$$\alpha = \frac{\varepsilon_a - \varepsilon_b}{\varepsilon_a + \varepsilon_b}, \tag{48}$$

f being the filling ration of the cylinders. Using this effective dielectric function, the dispersion relation of the guided modes in the (loss-less) effective medium is determined by

$$1 - \left(\frac{-\gamma/\varepsilon_b + \gamma'/{\rm Re}(\varepsilon_{\rm eff}^{\rm MG})}{\gamma/\varepsilon_b + \gamma'/{\rm Re}(\varepsilon_{\rm eff}^{\rm MG})}\right)^2 \exp(2i\gamma d) = 0, \tag{49}$$

$$\gamma = \sqrt{(\frac{\omega}{c})^2 \varepsilon_b - k_x^2}, \tag{50}$$

$$\gamma' = \sqrt{(\frac{\omega}{c})^2 {\rm Re}(\varepsilon_{\rm eff}^{\rm MG}) - k_x^2} \tag{51}$$

d being the thickness of the photonic crystal. By imposing the matching condition of frequency ω and wave vector $k_x (= \omega/v)$, the above equation has a sequence of solutions, which agree with the positions of the sharp loss peaks of $v = 0.9c$ in Fig.10 fairly well.

The convergence of $P_{el}(\omega, k_z)$ is a direct consequence of the convergence of the scattering matrix Q_{-+} itself. As was discussed by Botten et al, the converged value of Q_{-+} gives the reflectance of the semi-infinite photonic crystal.[39] This also implies that using the converged value of Q_{-+}, we can extract the effective dielectric function via Fresnel's formula of the interface S-matrix. That is, for the P-polarized incident wave, the scattering matrix Q_{-+} of the semi-infinite photonic crystal can be regarded as the interface S-matrix between the background medium and the effective medium:

$$[Q_{-+}(h_0,h_0)]_{pp} \simeq \frac{\gamma/\varepsilon_b - \gamma'/\varepsilon_{\text{eff}}}{\gamma/\varepsilon_b + \gamma'/\varepsilon_{\text{eff}}}, \tag{52}$$

$$\gamma' = \sqrt{(\frac{\omega}{c})^2\varepsilon_{\text{eff}} - (\frac{\omega}{v})^2}. \tag{53}$$

Here, $k_z = 0$ was assumed. The effective dielectric function ε_{eff} obtained in this way, along with that of Maxwell-Garnett for the dense photonic crystal are shown in Fig.11. The function is not so far from the effective dielectric function of Maxwell-Garnett, though some extra features at $\omega a/2\pi c \simeq 0.019$ and 0.026 are observed. In the next section we will see that the EEL spectrum in the photonic crystal, when the charged particle runs inside the photonic crystal, is well reproduced with the effective dielectric function having the extra features. As for the dilute photonic crystal, our effective dielectric function is very close to that of Maxwell-Garnett.

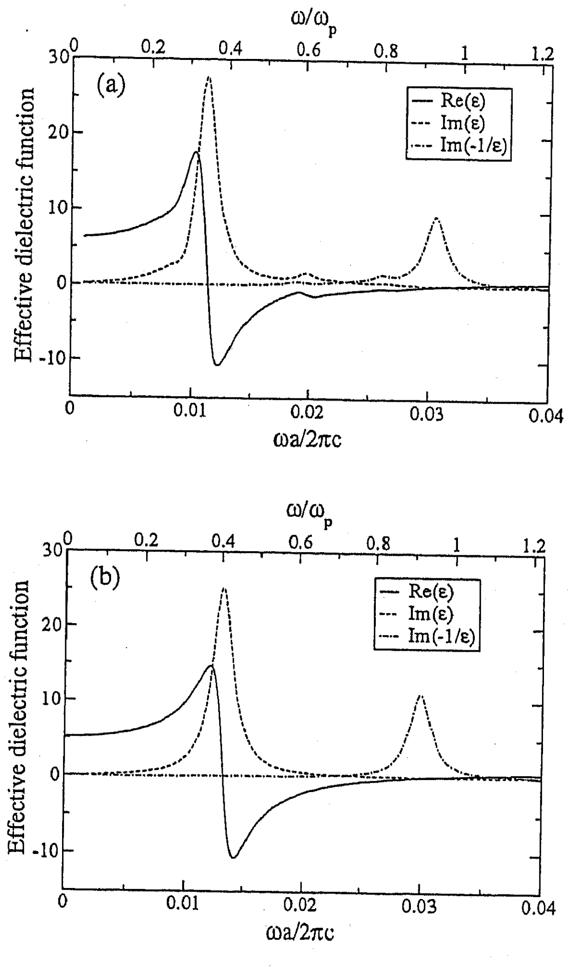

FIG. 11: (a) The effective dielectric function for the P-polarized light in the dense photonic crystal($a = 2.16r$). The case $k_z = 0$ was assumed. (b) The effective dielectric function of Maxwell-Garnett in the dense photonic crystal.

V. ELECTRON RUNNING INSIDE PHOTONIC CRYSTAL

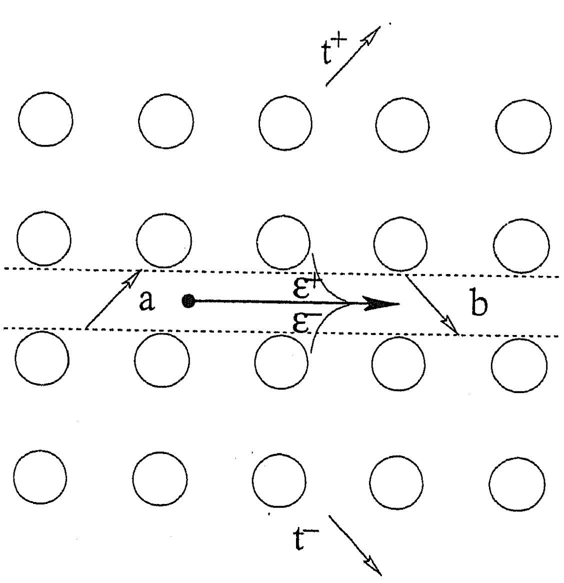

FIG. 12: A charged particle runs inside the photonic crystal with an equal distance from the upper and lower nearest layers of the trajectory. The plane wave coefficients of the induced wave in the void stripe including the trajectory are denoted by **a** and **b**.

When a charged particle runs inside the photonic crystals, the induced radiation field is rather involved owing to the multiple-scattering among the layers above and below the trajectory. However, the scattering matrix formalism is readily adapted to the case as long as the particle does not penetrate any cylinders in the photonic crystals. A schematic illustration of the system under consideration is shown in Fig.12. In this case the induced radiation field reacting back to the charged particle is determined as

$$\mathbf{E}^{\text{ind}}(\mathbf{x},\omega) = -\frac{\mu_0 e\omega}{2}\sum_h \int \frac{dk_z}{2\pi} \times \left(\mathbf{a}_h e^{i\mathbf{K}_h^+\cdot(\mathbf{x}-\mathbf{x}_0)} + \mathbf{b}_h e^{i\mathbf{K}_h^-\cdot(\mathbf{x}-\mathbf{x}_0)}\right), \tag{54}$$

$$\mathbf{a}_h = (1 - Q^d_{+-}Q^u_{-+})^{-1}Q^d_{+-}(\epsilon^- + Q^u_{-+}\epsilon^+), \tag{55}$$

$$\mathbf{b}_h = (1 - Q^u_{-+}Q^d_{+-})^{-1}Q^u_{-+}(\epsilon^+ + Q^d_{+-}\epsilon^-), \tag{56}$$

where $Q^{u(d)}_{\pm\pm}$ is the scattering matrix of the upper(lower) layers above(below) the trajectory and $\mathbf{x}_0 = (0, y_0, z_0)$. Beside, the Fourier coefficients of the upper and lower transmitted wave, denoted by $\mathrm{t}_h^{\pm}$, is also obtained as

$$\mathrm{t}_h^{+} = \sum_{h'} Q^{u}_{++}(h,h')(\epsilon^{+}\delta_{h'h_0} + \mathrm{a}_{h'}), \qquad (57)$$

$$\mathrm{t}_h^{-} = \sum_{h'} Q^{d}_{--}(h,h')(\epsilon^{-}\delta_{h'h_0} + \mathrm{b}_{h'}). \qquad (58)$$

Therefore, the EEL and SP radiation spectra per unit length becomes

$$P_{el}(\omega,k_z) = -\frac{1}{4}\mu_0 e^2\omega|\gamma_{h_0}|\mathrm{Im}\left(\mathrm{a}^{*}_{h_0}\cdot\epsilon^{-} - \mathrm{b}_{h_0}\cdot(\epsilon^{+})^{*}\right) \qquad (59)$$

$$P_{sp}(\omega,k_z) = \frac{1}{8}\mu_0 e^2\omega \sum_{h\in\mathrm{open}} \gamma_h\left(|\mathrm{t}_h^{+}|^2 + |\mathrm{t}_h^{-}|^2\right). \qquad (60)$$

Again, the flux conservation in a loss-less photonic crystal leads

$$\sum_{h\in\mathrm{open}} \gamma_h\left(|\mathrm{t}_h^{+}|^2 + |\mathrm{t}_h^{-}|^2\right)$$
$$= -2|\gamma_{h_0}|\mathrm{Im}\left(\mathrm{a}^{*}_{h_0}\cdot\epsilon^{-} - \mathrm{b}_{h_0}\cdot(\epsilon^{+})^{*}\right), \qquad (61)$$

which implies that the EEL is equal to the SP radiation emission.

At low frequencies we may expect that the EEL in a photonic crystal is somehow approximated by that of a lossy effective homogeneous medium. As is known well, the relativistic EEL in such a medium with permittivity ε_{eff} is given by

$$P_{el}(\omega,k_z) = \frac{1}{4}\mu_0 e^2\omega\mathrm{Re}\left[\frac{1}{\gamma}\left(1-(\frac{c}{v})^2\frac{1}{\varepsilon_{\text{eff}}}\right)\right], \qquad (62)$$

per unit length. When ε_{eff} is real and the condition $v > c/\sqrt{\varepsilon_{\text{eff}}}$ is satisfied, the above equation is equal to the Cerenkov loss. Otherwise, Eq.(62) can be regarded as the EEL by the absorption. In a homogeneous metal the bulk plasmon dominantly contributes to the EEL, because of the factor $1/\varepsilon_{\text{eff}}$.

Fig.13 shows the EEL spectra of the dense photonic crystal and its simulation using the effective dielectric function obtained by Eqs (52) and (53). Here, the charged particle runs with velocity 0.4c between the 32th and 33th layer of the 64-layer thick slab of the dense photonic crystal.

One can observe that the frequency of the main loss peak is larger than $\omega = 0.9\omega_p$, which is close to the bulk plasmon frequency. This is quite reasonable, taking account that the dense photonic crystal has a large filling ratio ($\simeq$ 67%) and thus is close to the bulk metal of Aluminum. Beside the main loss peak, two small peaks are observed in the EEL spectrum. Using the homogeneous medium approximation with the effective dielectric function obtained in the previous section the above features are well reproduced. It should be emphasized that the small two peaks in the dense photonic crystal can not be explained with the effective medium theory of Maxwell-Garnett based on $\varepsilon_{\text{eff}}^{\text{MG}}$ given by Eq.(47).

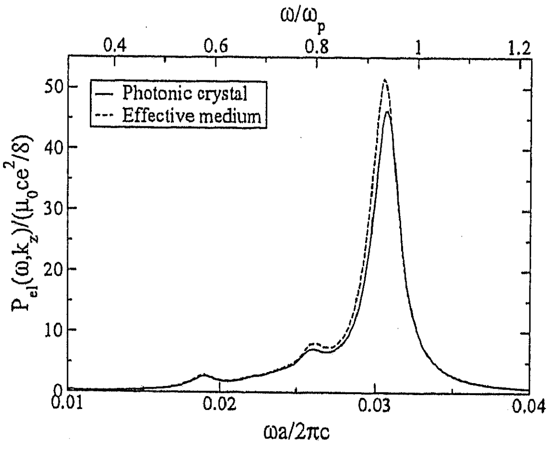

FIG. 13: The EEL spectrum in the dense photonic crystal having 64 layers along the $\Gamma-X$ direction is shown. The EEL spectrum in the effective medium whose dielectric function is given by Fig.11 is also plotted. The velocity of the charged particle is taken to 0.4c.

Regarding the EEL spectrum in the dilute photonic crystal, our effective dielectric function as well as the Maxwell-Garnett approximation reproduce the spectrum having a single peak near $\omega = \omega_p/\sqrt{2}$ fairly well.

VI. SUMMARY

In this paper we have presented a fully-relativistic analysis of the EEL and the induced radiation emission in various spatial arrangements of metallic cylinders by using the multiple scattering method and the layer-KKRO method. In an isolated metallic cylinder with a nanoscale diameter we showed that the EEL is dominated by the absorption rather than the induced radiation emission. Thus, the efficiency of converting the kinetic energy of the charged particle to the radiation emission is very low. In the two identical metallic cylinders a variety of EEL peaks appear. Some of them are attributed to the cavity mode localized in the groove between the cylinders. Such a cavity mode as well as the SPP modes become the seed of the flat bands in a dense periodic arrangement of the metallic cylinders. After presenting a mathematical description of the EEL and the SP radiation emission in two-dimensional photonic crystals composed of cylinders, we showed the numerical results of the EEL spectra in both dilute and dense periodic arrays of the metallic cylinders. In the dilute photonic crystal the EEL spectrum has a simple structure. The spectrum has a single peak near $\omega = \omega_p/\sqrt{2}$ and is not so far from the EEL spectrum in the isolated cylinder. However, when a high speed charged particle passes near the photonic crystal, a sequence of very sharp loss peaks, which comes from the lowest photonic band guided in the finite-thick photonic crystal, are observed. The peaks are comparable in magnitude with that by the SPP bands. On the other hand in the dense photonic crystal the EEL spectrum is very complicated reflecting the photonic band structure, though a good correspondence to the EEL spectrum in the almost touched two cylinders is observed. In both the photonic crystals the effective dielectric functions, which are obtained with the reflectance of the corresponding semi-infinite photonic crystals, fairly reproduce the EEL spectra when the charged particle runs inside the photonic crystals.

In this paper we have restricted ourselves to various arrangements of Aluminum cylinders whose diameter is a few nanometers, bearing carbon nano-tube arrays in mind. Since the plasma wavelength of Aluminum is much larger than the above scale, a metallic photonic crystal composed of the cylinders behaves as if it has an effective dielectric function reflecting the coupled SPPs, in the frequency range concerned. In addition the SP radiation from the photonic crystal is completely absent. However, it is of great importance to study the EEL and the SP radiation emission spectra when the lattice constant is comparable with the plasma wavelength of the constituent cylinders. In this case an effective medium approximation cannot be adapted and usual photonic bands affect strongly the EEL and induced radiation emission spectra. To explorer the spectra in such metallic photonic crystals with and without a structural defect is the main theme of the paper II.

Acknowledgments

The authors would like to thank J. Inoue and S. Yamaguti of Chiba University for useful comments. This work was supported by "Promotion of Science and Technology" from the Ministry of Education, Sports, Culture, Science and Technology of Japan.

---

[1] U. Kreibig and M. Vollmer, *Optical properties of metal clusters* (Springer-Verlag, Berlin, 1995).

[2] J.D. Joannopoulos, R.D. Meade, and J.N. Winn, *Photonic Crystals* (Princeton University Press, Princeton, 1995).

[3] K. Sakoda, *Optical Properties of Photonic Crystals*, (Springer-Verlag, Berlin, 2001).

[4] V.G. Veselago, Sov. Phys. Usp. **10**, 509 (1968).

[5] J.B. Pendry, Phys. Rev. Lett. **85**, 3966 (2000).

[6] R.A. Shelby, D.R. Smith, and S. Shultz, *Science* **292**, 77 (2001).

[7] A.A. Lucas, L. Henrard, and Ph. Lambin, Phys. Rev. B **49**, 2888 (1994).

[8] R.H. Ritchie and A. Howie, Philos. Mag. A **58**, 753 (1988).

[9] M. Schmeits, Phys. Rev. B **39**, 7567 (1988).

[10] J.M. Pitarke and A. Rivacoba, Surf. Sci. **377-379**, 294 (1997).

[11] G.F. Bertsch, H. Esbensen, and B.W. Reed, Phys. Rev. B **58**, 14031 (1998).

[12] J.B. Pendry and L. Martin-Moreno, Phys. Rev. B **50**, 5062 (1994).

[13] J.B. Pendry and A. MacKinnon. Phys. Rev. Lett. **69**, 2772 (1992).

[14] F.J. García de Abajo, Phys. Rev. Lett. **82**, 2776 (1999).

[15] F.J. García de Abajo, Phys. Rev. B **60**, 6103 (1999).

[16] F.J. García de Abajo and A. Howie, Phys. Rev. Lett. **80**, 5180 (1998).

[17] F.J. García de Abajo and A. Howie, Phys. Rev. B **65**, 115418 (2002).

[18] F.J. García-Vidal and J.M. Pitarke, Eur. Phys. J. B **22**, 257 (2001).

[19] T. Ochiai and K. Ohtaka, following paper, Phys. Rev. B .

[20] N. Yamamoto, K. Araya, and F.J. García de Abajo, Phys. Rev. B **64**, 205419 (2001).

[21] S.J. Smith and E. M. Purcell, Phys. Rev. **92**, 1069 (1953).

[22] F.J. García de Abajo, Phys. Rev. E **61**, 5743 (2000).

[23] K. Ohtaka and S. Yamaguti, Opt. Spectrosc. **91**, 477 (2001).

[24] S. Yamaguti, J. Inoue, and K. Ohtaka, Phys. Rev. B **66**, 085209 (2002).

[25] S. Yamaguti, J. Inoue, O. Haeberlé and K. Ohtaka, Phys. Rev. B **66**, 195202 (2002).

[26] L.D. Landau, E.M. Lifshitz, and L.P. Pitaevskii, *Electrodynamics of Continuous Media* (Pergamon Press, Oxford, 1984).

[27] J.C. Maxwell-Garnett, Philos. Trans. R. Soc. London A **203**, 385 (1904).

[28] J.M. Pitarke, F.J. García-Vidal, and J.B. Pendry, Phys. Rev. B **57**, 15261 (1998).

[29] D.R. Smith, S. Schultz, P. Markos, and C.M. Soukoulis, Phys. Rev. B **65**, 195104 (2002).

[30] K. Ohtaka, T. Ueta, and K. Amemiya, Phys. Rev. B **57**, 2550 (1998).

[31] M. Inoue and K. Ohtaka, Phys. Rev. B **26**, 3487 (1982).

[32] M. Inoue and K. Ohtaka, J. Phys. Soc. Jpn **52**, 1457 (1983).

[33] M. Inoue and K. Ohtaka, J. Phys. Soc. Jpn **52**, 3853 (1983).

[34] F.J. García-Vidal and J.B. Pendry. Phys. Rev. Lett. **77**, 1163 (1997).

[35] T. Ito and K. Sakoda, Phys. Rev. B **64**, 045117 (2001).

[36] T. Ochiai and J. Sánchez-Dehesa, Phys. Rev. B **65**, 245111 (2002).

[37] V. Kuzmiak, A.A. Maradudin, and F. Pincemin, Phys. Rev. B **50**, 16835 (1994).

[38] K. Ohtaka and H. Numata, Phys. Lett. **73A**, 411 (1979).

[39] L.C. Botten, N.A. Nicorovici, R.C. McPhedran, C. Martijn de Sterke, and A.A. Asatryan, Phys. Rev. E **64**, 046603 (2001).

[40] J. Korringa, Physica **13**, 392 (1947).

[41] W. Kohn and N. Rostoker, Phys. Rev. **94** 1111 (1954).

[42] K. Ohtaka, Phys. Rev. B **19**, 5057 (1979).

[43] K. Ohtaka, J. Phys. C **13**, 667 (1980).

[44] A. Modinos, Physica A **141**, 575 (1987).

[45] N. Stefanou, V. Karathanos, and A. Modinos, J. Phys. Condens. Matter **4**, 7389 (1992).

[46] F.J. García de Abajo and L.A. Blanco, Phys. Rev. B **67**, 125108 (2003).

Relativistic electron energy loss and induced radiation emission in two-dimensional metallic photonic crystals II: Photonic band effects

Tetsuyuki Ochiai and Kazuo Ohtaka
Center for Frontier Science, Chiba University, Chiba 263-8522, Japan
(Dated: March 5, 2004)

This paper presents a fully relativistic analysis of the electron energy loss and the induced radiation emission in a metallic photonic crystal. The crystal's lattice constant is comparable with the plasma wavelength, and the analysis is presented in terms of the multiple scattering method based on vector cylindrical waves. The electron energy loss and the Smith-Purcell radiation emission spectra are well correlated with the photonic band structures, both with and without a structural defect. In particular, surface-localized modes and waveguide modes localized in a linear defect can be identified in the spectra. In addition, we show that highly directive radiation emission is possible by using a waveguide mode at the Γ point.

PACS numbers: 42.70.Qs,73.20.Mf,34.50.Bw

I. INTRODUCTION

In the preceding paper[1] (referred to as Paper I) we presented a fully relativistic description of electron energy loss (EEL) and induced radiation emission in arbitrary arrays of non-overlapping metallic cylinders. The description is given in terms of the multiple scattering method based on vector cylindrical waves. As an example, we have explored arrays of aluminum cylinders whose diameters are a few nanometers, considering carbon nano-tube arrays and other metallic nano-structures. Using a nanoscale periodic structure, the induced radiation emission is prohibited kinetically in the frequency range of interest which is near the plasma frequency of aluminum. Thus, the EEL consists solely of the absorption in the structure. Moreover, an effective medium approximation can be reasonably applied to the structure because the wavelength is much greater than the pitch of the periodic structure.

However, if the diameter of the cylinders and the pitch in an array of metallic cylinders are comparable to or exceeds the plasma wavelength, the EEL and the induced radiation emission have a pronounced feature reflecting the photonic band structure. In particular, Smith-Purcell radiation (SPR) occurs in the frequency range of interest. As a consequence, a significant part of the EEL is caused by the SPR.

In this paper, we focus on the effects of photonic bands in a periodic array of metallic cylinders. As a model system, we choose a silver cylinder with radius r (160 [nm]) since silver has a low imaginary part in the dielectric function at the frequencies of visible light. Thus, we may expect that the absorption in the photonic crystal is quite small, so that the EEL is dominated by the SPR. The dielectric function of silver at these frequencies can be approximated with the Drude formula:

$$\varepsilon_a(\omega) = \varepsilon_\infty - \frac{\omega_p^2}{\omega(\omega + i\eta)}, \tag{1}$$

where ε_∞=5.7, $\hbar\omega_p = 9$[eV], and $\hbar\eta = 0.04$[eV]. The surface plasmon polariton in a flat silver-air interface can be found at

$$\omega = \frac{\omega_p}{\sqrt{\varepsilon_\infty + 1}} \tag{2}$$

in the non-retardation limit. The above dielectric profile of silver, as well as copper and nickel, can be utilized as the ingredient of a three-dimensional photonic crystal with an omni-directional band gap.[2] In fact, a dense face-centered cubic array of silver spheres with the same diameter has the complete photonic band gap far below the plasma frequency. Since the gap opens between the fifth and the sixth bands, it is robust against disorder. This is compared with the inverse opal, in which the complete band gap opens between the eighth and ninth bands.

This feature repeats in a dense square array of the silver cylinders in air. In contrast to metallic spheres, an array of metallic cylinders gives rise to polarization-sensitive light propagation because of the anisotropy of the structure. As is common knowledge, a periodic array of metallic cylinders behaves as if it is a bulk metal, with the low-frequency plasmon for the TM-polarized light[3], whose electric field is parallel to the cylindrical axis, traveling in-plane perpendicular to the cylindrical axis. The plasma frequency of the low-frequency plasmon is roughly estimated as

$$\omega_c \simeq \sqrt{\frac{f}{1 - f + f\varepsilon_\infty}}\,\omega_p, \tag{3}$$

f being the filling fraction of the silver cylinders. Below $\omega = \omega_c$ there is no bulk eigenmode of the TM polarization in the photonic crystal. For TE polarization, in which the magnetic field is parallel to the cylindrical axis, the photonic band structure has a wide band gap between the first and the second bands at $k_z = 0$. Therefore, the metallic photonic crystal has the polarization-independent in-plane gap as long as ω_c exceeds the upper gap edge of the TE polarization. Owing to the band gap, a variety of localized defect modes may appear when structural defects are introduced. It is important to explore in detail what happens when a charged particle passes near a metallic photonic crystal with such a band gap. We address this issue in the present paper.

The paper is organized as follows. In Section II the photonic band structure of a metallic photonic crystal is studied in connection with the SPR. We explore how the bulk eigenmodes as well as the surface-localized mode of the metallic photonic crystal affect the EEL and SPR spectra in Section III. Section IV discusses a possible scenario of directive SPR in the photonic crystal. Finally, we summarize the results.

II. PHOTONIC BAND AND SMITH-PURCELL RADIATION

Photonic band effects play a crucial role in the EEL and SPR spectra in a photonic crystal, particularly in the frequency range comparable with the lattice scale. Here we study a metallic photonic crystals composed of a square array of silver cylinders with the lattice constant $a = r/0.45 \simeq 355.6$[nm]. The photonic crystal is assumed to have infinite extent in the (1,0) direction of the square lattice and to have a finite thickness along the (0,1) direction. As in Paper I, the x, y, and z axes are considered to be parallel to (1,0), (0,1), and the cylindrical axis, respectively. The photonic band structure of P(TE)-polarization at $k_z = 0$ projected onto the surface Brillouin zone associated with the boundary parallel to (1,0) is shown in Fig.1. The band structure was calculated by using the two-dimensional layer Korringa-Kohn-Rostoker-Ohtaka method taking $l_{\max} = 10$. Here, we dropped the band diagram of the S(TM)-polarization because it is not relevant to our problem. However, at non-zero k_z we must take account of both the S and P polarizations owing to polarization mixing. In Fig.1 the shaded regions correspond to the bulk eigenmodes, whereas the blank regions correspond to the (pseudo) gaps. The photonic crystal has a large in-plane band gap between the first and the second bands. The gap-width/mid-gap ratio is about 36% at $k_z = 0$. We should note that the in-plane band gap is polarization-independent because the cutoff frequency ω_c for the TM polarization is about 0.92 in units of $2\pi c/a$. The in-plane gap, nevertheless, opens at small k_z even after mixing of the polarizations, whereas the gap increases in frequency. In addition, at high frequencies near $\omega a/2\pi c = 1$, there are infinite flat bands of surface plasmon polariton (SPP) origin. This is logical, taking into account that $\omega_p/\sqrt{\varepsilon_\infty + 1} = 0.997$ in units of $2\pi c/a$. The following discussion is restricted to the frequency region below $\omega a/2\pi c \leq 0.9$, such that the flat bands of SPP origin can be neglected.

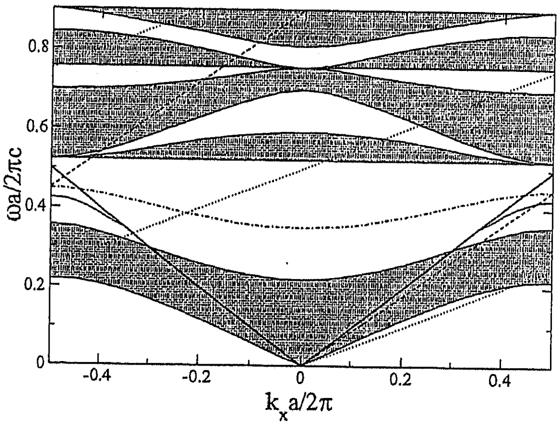

FIG. 1: The TE photonic band structure of the square lattice of the silver cylinders at $k_z = 0$ was projected onto the surface Brillouin zone associated with the boundary parallel to the (1,0) direction of the square lattice. The lattice constant is $a = r/0.45 \simeq 355.6$[nm], where r is the radius of the cylinders, which was taken to be 160[nm]. The shaded regions correspond to the bulk eigenmodes, whereas the blank regions correspond to the (pseudo) gaps. The thick solid line is the light line ($\omega = \pm ck_x$) and the dotted(dashed) lines are the v lines ($\omega = v(k_x + h)$), which represent the the dispersion of the radiation accompanied by the charged particle traveling with velocity $v = 0.5c(0.9c)$. The charged particle is supposed to travel parallel to the boundary of the photonic crystal. The dispersion curve of the surface-localized mode (discussed in Sec. III) and that of the waveguide mode, which is obtained by removing a single column of the cylinders from the photonic crystal (discussed in Sec. IV), are also shown (solid and dash-dotted lines).

Before discussing the effects of the photonic bands on the EEL and SPR, we should recall the kinetics involved in the EEL and SPR. A schematic illustration of the system under study is shown in Fig.2. When a charged particle passes near the photonic crystal with its trajectory parallel to the (1,0) direction, the particle produces a source term of the external current in Maxwell's equation of the system. The term is proportional to $\delta(x - vt)$, where δ is Dirac's delta function. Therefore, the Fourier transform with respect to x and t yields the dispersion relation $\omega = vk_x$ (referred to as the v line) for the radiation accompanied by the charged particle. In a vacuum, this dispersion is outside the light cone, and thus the radiation is evanescent. However, the radiation is scattered by the photonic crystal, acquiring an Umklapp momentum shift for k_x owing to the periodicity of the photonic crystal. After the scattering, The shifted v line $\omega = v(k_x + h)$ lies partially inside the light cone. Here, $h (= 2\pi n/a,\ \ n$: integer) stands for a reciprocal lattice associated with the (1,0) direction. Therefore, the evanescent radiation can transform into a propagating one. In order to visualize this, the v lines of different velocities ($v = 0.5c$ and $0.9c$) and the light line $\omega = \pm ck_x$ (provided $k_z = 0$) are overlaid onto the projected band structure in Fig.1. As can be seen in Fig.1, the shifted v line of $v = 0.5c$ and $h = 1$ in units of $2\pi/a$ is inside the light cone if $\omega a/2\pi c \geq 0.333$. For the shifted v line of $v = 0.9c$ and $h = 1$, the line is inside the light cone if $\omega a/2\pi c \geq 0.474$. In general, the shifted v line of velocity v and $h = 1$ is

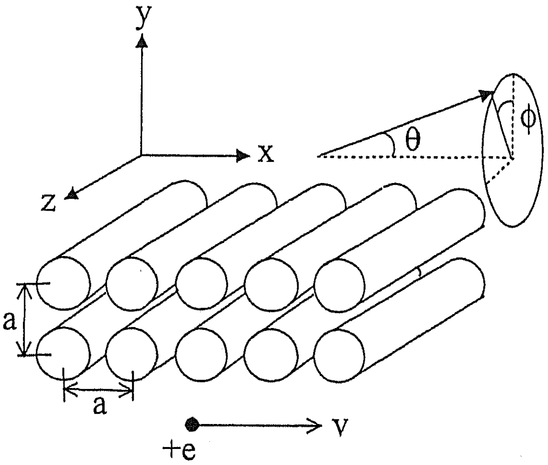

FIG. 2: Schematic illustration of the system under study. The photonic crystal has infinite extent in the xz plane and has a finite thickness along the y direction (just two layers in the figure). A charged particle travels below the photonic crystal and induces the Smith-Purcell radiation(SPR). The polar angle θ of the SPR is defined as the inner angle between the unit vector directed to a far-field observation point and the x axis. The azimuthal angle ϕ is defined on the yz plane. The $y(z)$ axis corresponds to $\phi = 0°(90°)$.

inside the light cone if the following condition is satisfied:

$$\frac{\omega a}{2\pi c} \geq \frac{\frac{v}{c}}{1+\frac{v}{c}}. \qquad (4)$$

This provides the low-frequency threshold of the SPR.

To describe the propagating direction of the SPR, it is convenient to introduce the polar coordinate (Fig.2). The polar angle (θ) is defined as the inner angle between the unit vector directed to a far-field observation point and the x axis. The azimuthal angle (ϕ) is defined on the yz plane. Since the x component of the wave number vector of the SPR is given by $k_x = \omega/v - h$, the polar angle of the SPR is fixed as

$$\cos\theta_h = \frac{\frac{\omega}{v} - h}{\frac{\omega}{c}}, \qquad (5)$$

at a given frequency ω. The azimuthal angle of the SPR depends on both ω and k_z, and is given by

$$\tan\phi = \frac{k_z}{\sqrt{(\frac{\omega}{c})^2 - (\frac{\omega}{v} - h)^2 - k_z^2}}. \qquad (6)$$

Since the k_z integral is involved in the SPR spectrum, as was derived in Paper I, the azimuthal angle of the SPR is not fixed.

In the photonic crystal we must combine the above kinetics with the photonic dispersion relation $\omega = \omega_n(k_x, k_y, k_z)$ inside the crystal. We can expect that a large enhancement of the EEL and SPR when the v lines (including the shifted ones) hit the photonic bands. This is caused by exciting photonic eigenstates on the v lines. As depicted in Fig.1, the v lines are partially in the shaded regions that correspond to the bulk eigenstates and are also in the pseudo gaps. The shaded region does not truly represent a continuous distribution of photonic eigenstates. Rather, it represents a dense but discrete distribution of them. This is due to our using a finite-thickness photonic crystal, and the quantization of the momentum along the direction of thickness must be considered. Therefore, by scanning ω, the v lines hit a sequence of discrete-level eigenstates. Thus, the EEL and SPR spectra reveal a rapid oscillation inside the shaded regions. Let us suppose that one of the eigenstates on the v line causes a strong enhancement in the SPR spectrum. This yields a monochromatic radiation with a particular frequency, and thus the radiation is directed to a certain polar angle determined by Eq.(5). However, it does not generally imply that the radiation is also directive as it relates to the azimuthal angle. In Sec.IV, we will discuss how to obtain a directive SPR relating to both polar and azimuthal angles.

III. BULK AND SURFACE STATES

Let us consider the EEL and SPR when a charged particle passes near the finite-thickness photonic crystal. In Fig.1 the v lines of $v = 0.5c$ lie in the shaded region of the lowest band at $0.2 \leq \omega a/2\pi c \leq 0.33$. The lines are inside the photonic band gap in the frequency region between $\omega a/2\pi c \simeq 0.33$ and 0.52 and in the pseudo gaps near $\omega a/2\pi c \simeq 0.6, 0.73$ and 0.85. In contrast, the v lines of $v = 0.9c$ lie in the shaded region of the lowest band up to $\omega a/2\pi c \simeq 0.33$. The lines are also inside the photonic band gap and in the three pseudo gaps near $\omega a/2\pi c =$ 0.53, 0.73, and 0.8. Inside the band gap, the v line of $v = 0.9c$ lies partially outside the light cone.

As was mentioned, when the v line lies in a shaded region, the charged particle excites a sequence of bulk discrete-level eigenmodes in the region. Thus, the EEL and the SPR spectra reveal a rapid oscillation. Fig.3 shows both of these spectra in the eight-layer-thick photonic crystal along the (0,1) direction, where $v = 0.5c$ and $k_z = 0$ were assumed. The distance between the trajectory of the charged particle and the plane bisecting the boundary layer is $0.5a$. As was derived in Paper I, the two spectra must coincide if there is to be no absorption in the photonic crystal. Owing to the small imaginary part in the dielectric function of silver, the EEL spectrum is nearly equal to the SPR spectrum in a wide frequency region including the band gap. Below the threshold of the SPR the EEL spectrum has a sequence of very sharp peaks that appear when the v line lies in the shaded region of the lowest band in Fig.1. Since this happens at rather low frequencies, an effective medium approximation is plausibly applied, so that the positions of these peaks can be estimated by the same procedure

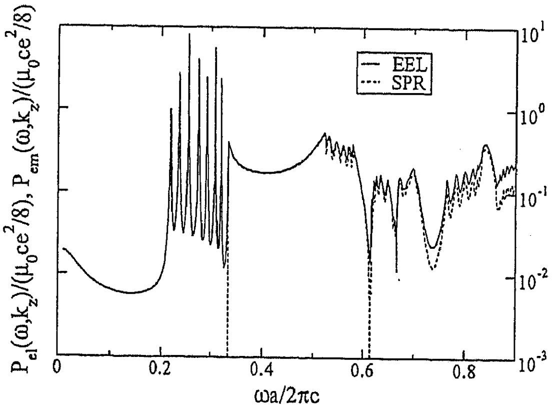

FIG. 3: The EEL (solid line) and SPR (dashed line) spectra in the eight-layer-thick photonic crystal under consideration (See the caption of Fig.1). The charged particle travels with velocity $v = 0.5c$, maintaining a distance of $0.5a$ from the plane bisecting the boundary layer. $k_z = 0$ was assumed.

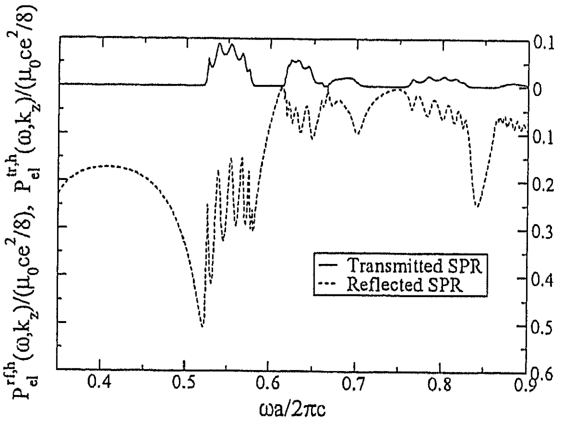

FIG. 4: Transmitted and reflected SPR spectra of Umklapp shifted channel $h = 1$ in the eight-layer-thick photonic crystal under study. The transmitted(reflected) SPR spectrum is shown above(below) the horizontal axis. The same parameters as in Figs.1 and 2 were used.

used in Paper I. Above the SPR threshold, both spectra reveal a rich structure. At approximately $\omega a/2\pi c = 0.4$, where the in-plane gap opens, the spectra have no pronounced structure. Moreover, one can find a marked dip at $\omega a/2\pi c \simeq 0.61$, where a pseudo-gap opens. Here, the deviation of the SPR from the EEL is quite pronounced. Generally, above the threshold, this deviation becomes large at high frequencies even if the v line is in the shaded regions.

Though the band gap and the pseudo gap can be identified in the EEL and the SPR spectra, their effects can be clearly demonstrated when we divide the SPR spectrum into the transmitted and reflected SPR spectra with fixed h, with focus on the transmitted spectrum. The transmitted and reflected SPR spectra are defined by

$$P_{\rm em}(\omega,k_z) = \sum_{h\in{\rm open}} \left(P_{\rm em}^{{\rm tr},h}(\omega,k_z) + P_{\rm em}^{{\rm rf},h}(\omega,k_z)\right), \tag{7}$$

$$P_{\rm em}^{{\rm tr},h}(\omega,k_z) = \frac{1}{8}\mu_0 e^2 \omega e^{-2|\gamma_{h_0}|s}\gamma_h |Q_{++}(h,h_0)\epsilon^+|^2 \tag{8}$$

$$P_{\rm em}^{{\rm rf},h}(\omega,k_z) = \frac{1}{8}\mu_0 e^2 \omega e^{-2|\gamma_{h_0}|s}\gamma_h |Q_{-+}(h,h_0)\epsilon^+|^2 \tag{9}$$

$$\gamma_h = \sqrt{(\frac{\omega}{c})^2 - (k_x+h)^2 - k_z^2}, \tag{10}$$

where $Q_{\pm\pm}$ is the scattering matrix of the finite-thickness photonic crystal, ϵ^+ is the plane-wave coefficient of the incident evanescent wave accompanied by the charged particle, and ω/v is divided into the momentum in the first Brillouin zone k_x and a reciprocal lattice h_0 (See Paper I for details).

Fig.4 shows both the transmitted and reflected SPR spectra for the same structure as in Fig.3. As illustrated in Fig.4, the transmitted SPR spectrum is almost zero in the gap and the pseudo-gaps. However, this does not imply that the reflected SPR spectrum has a peak there, because the total SPR spectrum is a complicated function of frequency. Instead, the reflected SPR spectrum has no rapid oscillation in these gaps. Apparently, the the transmitted SPR intensity decreases as the number of layers increases owing to light absorption. In contrast, the reflected SPR spectrum converges to a certain function as the number increases.

In Figs.3 and 4, there is another dip at $\omega a/2\pi c \simeq 0.67$, which does not correspond to any pseudo gap in the photonic band structure. In fact, the dip is located inside the shaded region in Fig.1. The dip appears at the intersection of the shifted v line of $h = 1$ and the line of the Bragg diffraction threshold ($\omega = -ck_x + 2\pi/a$). Thus, the dip is somehow related to the Rayleigh-Wood anomaly of diffraction grating.[4]

In the band gap, the v lines may intersect the dispersion curve of a surface-localized mode on the interface between the photonic crystal and air. This is the case for the structure under consideration. As shown in Fig.1, the v line of $v = 0.9c$ lies outside the light cone in the band gap, so that it can excite a surface-localized mode. Fig.5 shows both the EEL and the total SPR spectra in the 32-layer-thick photonic crystal, where the charged particle travels with velocity $v = 0.9c$. There is a remarkable peak of the EEL spectrum at $\omega a/2\pi c \simeq 0.42$. The peak is higher than any other peaks found in the shaded region. Since the peak is found in the in-plane band gap outside the light cone, the peak is attributed to the surface-localized mode. By changing the velocity of the charged particle, we can trace the dispersion curve of the surface mode. The result was already implemented in Fig.1. With this analysis, the electron energy loss spectroscopy is capable of experimentally determining the dispersion relation of the surface-localized mode.

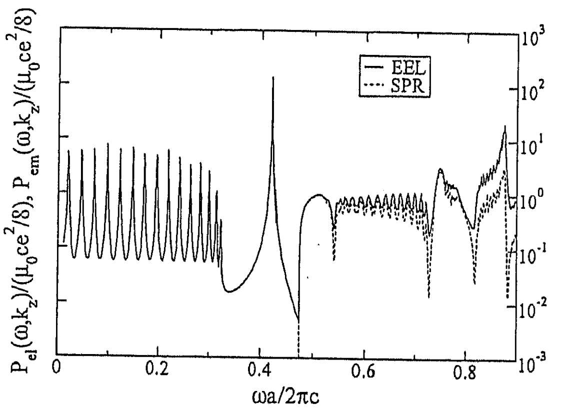

FIG. 5: EEL and SPR spectra in the 32-layer-thick photonic crystal along the (0,1) direction. The charged particle travels with velocity $v = 0.9c$, maintaining distance $0.5a$ from the plane bisecting the boundary layer.

IV. DIRECTIVE SMITH-PURCELL RADIATION

In the previous sections, we studied the effects of photonic bands on the EEL and SPR spectra in a finite-thickness photonic crystal. There, the spectra were compared with the projected band diagram, which is obtained from the photonic bands of the corresponding infinitely thick sample along the stacking direction. In the eight- or 32-layer thick samples, fine structures of the EEL and SPR spectra can be clearly observed. However, as the number of layers increases, the fine structures become hidden, owing to the non-zero imaginary part of the dielectric function of silver. As a result, no marked peak of high quality can be found in the SPR spectrum of the thick samples, whereas the EEL spectrum still has the very sharp peak of the surface-localized mode. In view of coherent light source, it is advantageous to have a sharp peak in the SPR spectrum at a particular frequency. Moreover, the SPR is more useful when highly directive.

When we consider the photonic band structure in bulk, the wave vectors of the matched eigenstates to the charged particle are distributed on a surface in the first Brillouin zone because the matching condition is given by

$$\omega = \omega_n(k_x, k_y, k_z), \tag{11}$$

$$\frac{\omega}{v} = k_x \quad (\text{mod.}\frac{2\pi}{a}), \tag{12}$$

which generally has a two-dimensional solution in the momentum space. Therefore, it is difficult to realize a directive SPR in a thick sample.

The above difficulty can be overcome either by considering a monolayer of silver or by introducing a linear defect into the photonic crystal. In the former case, we can no longer adapt the concept of the projected band structure because it assumes infinite thickness along the stacking direction. Instead, the band structure of the quasi-guided modes with finite lifetimes must be taken into account. The modes have a two-dimensional dispersion relation $\omega = \omega_n(k_x, k_z)$ in which confinement of light in the y-direction removes the k_y dependence in ω_n. In the latter case, the linear defect can support a waveguide mode localized in it. The waveguide mode also has the two-dimensional dispersion relation. As a result, the wave vectors of the matched eigenstates in these structures are distributed on a curve in the first Brillouin zone. Thus, it is simple to have a directive SPR.

First, let us consider the monolayer case. Fig.6 illustrates the photonic band structure of the quasi-guided modes in the light cone as well as the true guided modes outside the light cone. Again, we set $k_z = 0$ for simplicity. The quasi-guided modes in the figure were identified with the method given in Ref.5, whereas the true guided modes were obtained by solving the secular equation $\det(S^{-1}) = 0$, where S is the scattering matrix of the monolayer. It should be stressed that if the shifted v line hits a quasi-guide mode at the Γ point, it yields a directive SPR emission normal to the monolayer as long as no Bragg channels open. This scenario of the directive radiation emission is the same as that in dipole radiation[6], where very high directivity is achieved by exciting a quasi-guided mode at the Γ point.

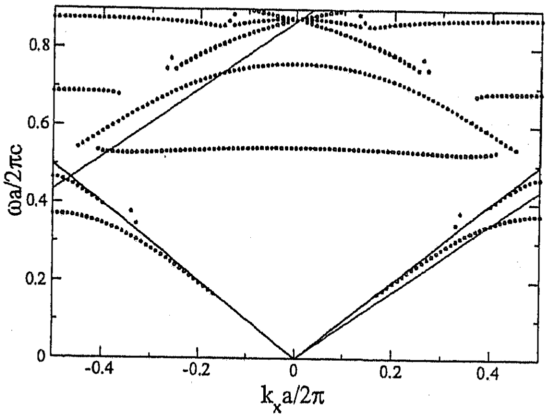

FIG. 6: Photonic band structure in the monolayer of silver cylinders. The same parameters as Fig.1 were assumed. The open(solid) circles are the even(odd) modes with respect to the plane bisecting the monolayer, The thick solid line represents the boundary of the light cone; the thin solid line is the v line of $v = 0.87c$.

To explore the directivity of the SPR in the monolayer, the elastic differential cross section is introduced. At a far-field observation point specified by solid angle $\Omega = (\theta, \phi)$ (see Fig.2), the only plane-wave components that contribute to the differential cross section at Ω are those with the wave vector parallel to the solid angle. Thus, the elastic differential cross section of the SPR is given by

$$\frac{dP}{d\phi} = \cos^2\phi \sin^2\theta_h |t_h^+(\omega, k_z)|^2, \tag{13}$$

per unit azimuthal angle. Here, since the polar angle of the propagating direction is fixed as in Eq.(5) in the SPR, the polar angle dependence of the differential cross section, which is given by a Dirac's delta function at $\theta = \theta_h$, was integrated out. In Eq.(13), t_h^+, which stands for the plane-wave coefficient of the electric field above the photonic crystal, has argument k_z equal to $(\omega/c)\sin\theta_h \sin\phi$.

In order to attain a directive SPR normal to the monolayer, θ_h must be equal to 90°.[7] This can be achieved by imposing $\omega/v = h$ and by taking ω to be the frequency ω_Γ of one of the quasi-guided modes at the Γ point. For instance, putting $v = \omega_\Gamma a/2\pi n$ (n: integer) yields $\theta_h = 90°$ for the channel of $h = n$ in units of $2\pi/a$. We should note, however, at a typical velocity of the electron used in the EEL spectroscopy in a scanning transmission electron microscope($v \simeq 0.5c$), only the channel of $h = 1$ (in units of $2\pi/a$) is favorable for the directive SPR. This is because in the frequency region relevant to the higher channels of $h \geq 2$ the photonic band structure is so dense in frequency that we will not be able to obtain the SPR of monotonic frequency. In the following discussion we thus restrict ourselves to the channel of $h = 1$.

As presented in Fig.6, the quasi-guided modes appear at $\omega a/2\pi c = 0.544$, 0.759, and 0.870-0.877. However, the lower two modes yield very broad peaks in the SPR spectrum, reflecting that the corresponding peaks of the optical density of state are very broad in frequency. In contrast, the latter three modes combined yield a sharp peak in the SPR spectrum. Thus, we may expect a directive SPR normal to the monolayer to take place.

The scattering cross section of the SPR at $\omega a/2\pi c = 0.870$, provided $v = 0.870c$, is shown in Fig.7. In this case, the directivity of the SPR is not so high owing to the rather flat dispersions of the relevant quasi-guided modes along k_z. Furthermore, two small peaks of the angular distribution of the differential cross section are observed at $\phi \simeq 120°$ and 240° in the reflected SPR. They represent the simultaneous excitation of another quasi-guided mode. In fact, we found that the band that terminates the quasi-guided mode of $\omega a/2\pi c = 0.759$ at $k_z = 0$ intersects the line of $\omega a/2\pi c = 0.870$ near the light line $\omega = ck_z$. The quasi-guide mode at the intersection is responsible for the small peaks. Therefore, in order to obtain directive SPR using the quasi-guide modes, the dispersion of the quasi-guided mode must be optimized.

Next, we consider a linear defect introduced in the silver photonic crystal employed in the previous section. We first assume a nine-layer-thick photonic crystal, i.e., a stack of nine identical monolayers of the cylinders. We then remove the fifth layer altogether, leaving the linear defect parallel to the xz plane, which is sandwiched by four layers on each side. The resultant EEL and SPR spectra reveal a sharp resonance at the frequency of the waveguide mode. Thus, by tracking the peak frequencies as a function of k_x and k_z, we can determine the dispersion relation of the waveguide mode. The dispersion curve obtained in this way is plotted in Fig.1. Moreover, an ordinary transmission calculation across the linear defect can also determine the dispersion curve in the light cone.[8] We have examined both methods, and the results are wholly consistent. As seen in Fig.1, the dispersion curve lies mostly in the light cone, so that the SPR spectrum is strongly affected by the waveguide mode.

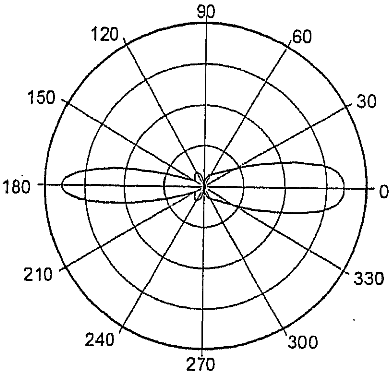

FIG. 7: The azimuthal angle (ϕ) distribution of the SPR in the monolayer of the silver cylinders. The velocity of the charged particle and the frequency were taken to be $v = 0.870c$ and $\omega a/2\pi c = 0.870$, in order to excite the quasi-guided mode at the Γ point. The distance between the trajectory of the charged particle and the plane bisecting the monolayer is $0.5a$.

A waveguide mode can also be utilized for directive SPR because it also has a two-dimensional dispersion relation. It should be stressed here that the in-plane gap shifts upward in frequency with increasing $|k_z|$. The dispersion curve of the waveguide mode behaves similarly, as will be seen later. Moreover, the Γ point is a minimum as a function of k_x. This yields the dispersion relation approximated around $(k_x, k_z) = (0, 0)$ with

$$\omega = \omega_0 + \alpha k_x^2 + \beta k_z^2 \quad (\alpha, \beta > 0), \tag{14}$$

ω_0 being the eigenfrequency of the waveguide mode at $(k_x, k_z) = (0, 0)$. When ω and v are chosen such that $\omega = \omega_0$ and $k_x = 0$, $k_z = 0$ is also derived. Thus, the shifted v line only hits the waveguide mode at $k_x = k_z = 0$ at this frequency. This yields a highly directive emission of SPR toward $(\theta, \phi) = (90°, 0°)$.

A similar directive radiation emission was studied in connection with the antenna application. Temelkuran et al., reported that by introducing a planar defect in a woodpile structure with a complete photonic band gap, highly directive dipole radiation is achieved with the aid of the resonance of the planar defect mode.[9]

The scattering cross section of the SPR at $\omega a/2\pi c = 0.351$, which corresponds to the waveguide mode at $(k_x, k_z) = (0, 0)$ (the value of the dash-dotted curve at $k_x = 0$ in Fig.1), is shown in Fig.8. Here, we assumed

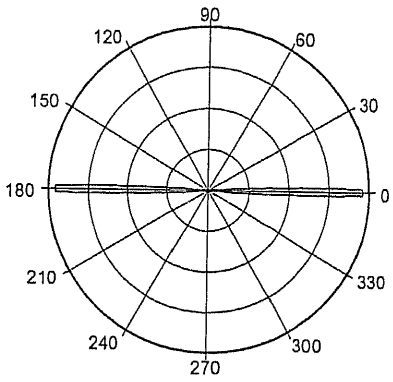

FIG. 8: The azimuthal angle (ϕ) distribution of the SPR in the photonic crystal with a linear defect. The velocity of the charged particle and the frequency were taken to be $v = 0.351c$ and $\omega a/2\pi c = 0.351$, in order to excite the waveguide mode at $(k_x, k_z) = (0, 0)$. The SPR is highly directive, compared with the monolayer case.

that the charged particle travels with velocity $v = 0.351c$ inside the linear defect, keeping the same distance from the layers that sandwich the defect. In this case, only a waveguide mode with even parity with respect to the trajectory can be excited because of the even symmetry of the incident evanescent wave accompanied by the charged particle. In addition, the upper and lower transmitted SPRs are identical. As depicted in Fig.8, the azimuthal angle distribution of the cross section is especially concentrated around $\phi = 0°$ (transmitted) and $180°$ (reflected). The high concentration is caused by the fact that there is no matched bulk eigenstate inside the light cone other than the waveguide mode at $(k_x, k_z) = (0, 0)$. This can be clearly seen in Fig.9. In this figure the photonic band structure is projected onto the the k_z axis provided $k_x = 0$, that is, the Γ point of the surface Brillouin zone. Outside the light cone the frequency $\omega a/2\pi c = 0.351$ is matched to the bulk eigenmodes, which cannot couple to external radiation. Though these modes cause light absorption in the photonic crystal, the emitted light of the SPR is highly directive at that frequency.

V. SUMMARY

In this paper, we analyzed how photonic bands affect the EEL and SPR spectra in a two-dimensional metallic photonic crystal composed of silver cylinders whose plasma wavelength is comparable with the lattice constant. The spectra are well correlated with the photonic band structure of the sample with and without a structural defect. In particular, photonic band gaps, pseudo gaps, surface-localized modes, and waveguide modes in the spectra can be identified. Thus, the EEL spectroscopy and the SPR measurement in a scanning transmission electron microscope provide an experimental method to determine such gaps and modes. However, possible fine structures in these spectra are hidden in a thick sample because of a non-zero imaginary part in the dielectric function of silver. This precludes the use of the SPR as a coherent light source in regular metallic photonic crystals. We proposed two routes to avoid this problem. One is to use the monolayer of the cylinders; the other is to use a linear defect introduced in the metallic photonic crystal. In both cases, we can obtain highly directive SPRs by tuning the frequency as well as the velocity of the charged particle.

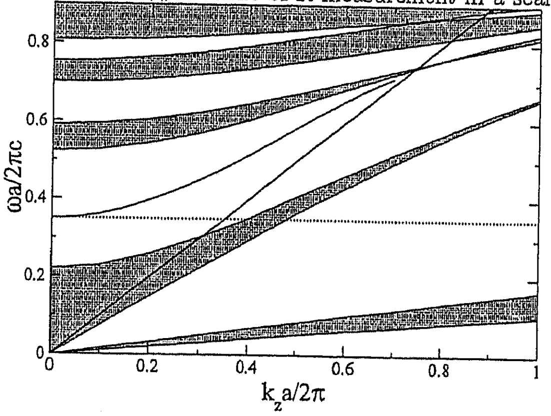

FIG. 9: The photonic band structure of the square photonic crystal under consideration (See Fig.1 caption) is projected onto the k_z axis, provided $k_x = 0$. The shaded regions correspond to the bulk eigenmodes, whereas the blank regions correspond to the (pseudo) gaps. The thick solid line is the light line $\omega = ck_z$ and the thin solid line stands for the dispersion relation of the waveguide mode localized in the linear defect of a missing column. The dotted line is of $\omega a/2\pi c = 0.351$.

Acknowledgments

This work was supported by the program "Promotion of Science and Technology" of the Ministry of Education, Sports, Culture, Science and Technology of Japan.

---

[1] T. Ochiai and K. Ohtaka, preceding paper, Phys. Rev. B .

[2] Z. Wang, C.T. Chan, W. Zhang, N. Ming, and P. Sheng, Phys. Rev. B 64, 113108 (2001).

[3] J.B. Pendry, A.J. Holden, W.J. Stewart, and I. Youngs, Phys. Rev. Lett. 76, 4773 (1996)

[4] Lord Rayleigh, Proc. R. Soc. London A 79, 399 (1907).

[5] K. Ohtaka, Y. Suda, S. Nagano, T. Ueta, A. Imada, T. Koda, J.S. Bae, K. Mizuno, S. Yano, and Y. Segawa, Phys. Rev. B **61**, 5267 (2000).

[6] T. Ochiai and K. Ohtaka, unpublished.

[7] Observation with $\theta = \theta_h = 90°$ is the easiest from the experimental point of view.

[8] T. Ueta, K. Ohtaka, N. Kawai, and K. Sakoda, J. Appl. Phys. **84**, 6299 (1998).

[9] B. Temelkuran, M. Bayindir, E. Ozbay, R. Biswas, M.M. Sigalas, G. Tuttle, and K.M. Ho, J. Appl. Phys. **87**, 603 (2000).

Means of sending a photon to an optically inactive photonic-band mode

Syuichi Yamaguti
Graduate School of Science and Technology, Chiba University
1-33 Yayoi-cho, Inage-ku, Chiba 263-8522, Japan

Tetsuyuki Ochiai, Jun-ichi Inoue, and Kazuo Ohtaka
Center for Frontier Science, Chiba University
1-33 Yayoi-cho, Inage-ku, Chiba 263-8522, Japan

(Dated: March 10, 2004)

We propose theoretically a means to send a photon to an optically inactive state at the Γ point of the Brillouin zone of a photonic crystal. It is shown that by using the light scattering of attenuated-total-reflection (ATR) geometry, a combined system of a photonic crystal and a prisim placed nearby, an optically inactive mode at the Γ point can be excited. The excitation is demonstrated by calculating the ATR signal for a photonic crystal of spheres arrayed in a square lattice, which presents a distinct dip due to excitation of the inactive mode. To confirm that the excited mode is indeed the one of the Γ point, we checked that equipartition of the energy of the excited mode is established among four diffracted plane-waves associated with the four shortest reciprocal-lattice-vectors of the excited Bloch wave.

PACS numbers: 42.70.Qs

Photonic crystals (PCs) have been attracting much interest in recent years due to their potential technological applications[1,2]. One of the key concepts for realizing such applications is the high Q value, or strong confinement effect, of the modes set up in a PC.

In the band structure of a PC, peculiar electromagnetic modes that are inactive to external optical probes exist at wave vectors of high symmetry in the Brillouin zone[2–8]. When the wave vector **k** is on, say, the Γ-X axis of a cubic PC, each of the photonic-band (PB) modes at that **k** is inactive to an external light of a particular polarization due to the polarization mismatch. When the wave vector is exactly at the Γ point ($\mathbf{k} = 0$), however, there are special PB modes which are decoupled completely from any of external plane-wave lights. We call here these special modes as optically inactive modes (OIMs). They are characterized by complete confinement. More than half of PB modes at the Γ point are generally OIMs. They are free from radiative damping due to leakage of the mode energies to the outer free space, despite the fact that they exist in the radiative region of the ω-$\mathbf{k}_\parallel$ space, ω and $\mathbf{k}_\parallel$ being the frequency and wave vector component parallel to the surface of the PC, respectively.

When a PB has an OIM at the Γ point, leakage to the outer space gradually increases from zero as the wave vector goes away from the Γ point along the dispersion curve. Recently, Fan et al. examined these modes near the Γ point and proposed the use of their huge Q values in the design of novel photonic devices[8]. Their idea is to make use of a very small but finite leak from a PC, i.e., a weak optical activity due to good, but not complete, confinement. In this paper, we focus on the OIMs at the Γ point of exactly zero optical activity. We propose a means to excite OIMs by using an external optical signal.

Suppose a slab of a PC that is bounded in the thickness direction by two surface layers. For simplicity, we assume the lattice structure in the lateral plane (x-y plane) to be a two-dimensional (2D) square lattice of point group C_{4v}. The 2D Brillouin zone in the k_x-k_y plane is then defined by the region of $-\pi/d \le k_x,\ k_y \le \pi/d$, d being the lattice constant of the square lattice.

We restrict ourselves to the excitation of PB modes of $\mathbf{k}_\parallel = 0$, i.e., the modes at the Γ point of the 2D Brillouin zone. To excite them by a plane-wave light, we must use a light of normal incidence by momentum conservation. The point group of the group of wave vector at the Γ point, $\mathcal{G}(\mathbf{k}_\parallel)$ with $\mathbf{k}_\parallel = 0$, is C_{4v}, which has five irreducible representations, A_1, A_2, B_1, B_2 and E, in the notation of group theory[9]. A_1, A_2, B_1 and B_2 are one-dimensional irreducible representations, and E is a two-dimensional irreducible representation. The modes that belong to one-dimensional irreducible representations are all optically inactive[3,10]. Thus, a plane-wave light from an external source can excite only PBs of E representation.

For later discussion, let us examine this situation in more detail. When $\mathbf{k}_\parallel = 0$, the electric field of a PB of one-dimensional irreducible representation is expressed as ($-\infty < z < \infty$)

$$\begin{aligned}\mathbf{E}(\mathbf{r}_\parallel, z; \mathbf{k}_\parallel = 0) &= \sum_{\rm nn} \mathbf{e}_{\mathbf{h}}^{(\rm nn)}(z) \exp(i\mathbf{h}\cdot\mathbf{r}_\parallel) \\ &+ \sum_{\rm 2nn} \mathbf{e}_{\mathbf{h}}^{(\rm 2nn)}(z) \exp(i\mathbf{h}\cdot\mathbf{r}_\parallel) + \cdots . \end{aligned} \quad (1)$$

Here, **h** stands for a 2D reciprocal lattice vector and the symbol $\sum_{\rm nn}$ represents the sum over the **h** points on the shell nearest-neighbor (nn) to the origin $\mathbf{h} = 0$, which consists of four points, $\mathbf{h}^{(\rm nn)} = (\pm1, 0)$ and $(0, \pm1)$ (in units of $2\pi/d$). The sum over the second nearest-neighbor (2nn) shell is the sum over $\mathbf{h}^{(\rm 2nn)} = (\pm1, 1)$ and $(\pm1, -1)$. The amplitudes $\mathbf{e}_{\mathbf{h}}^{(\rm nn)}(z)$, $\mathbf{e}_{\mathbf{h}}^{(\rm 2nn)}(z)$, etc. are generally finite even for z

outside the PC. The functions $\mathrm{e}_{\mathbf{h}}^{(\mathrm{nn})}(z)$ for four different h's of the nn shell transform within themselves by any operation of $\mathrm{C}_{4\mathrm{v}}$. To see it, let us take $g = \mathrm{C}_4$, a $\pi/2$ rotation about the z axis, as an example of the operator g of the group $\mathrm{C}_{4\mathrm{v}}$. In order for the Bloch functions given by Eq. (1) to be a basis function of a one-dimensional irreducible representation, operating g on it is equivalent to multiplying a constant C. That is, it holds that

$$g\left(\sum_{\mathrm{nn}} \mathrm{e}_{\mathbf{h}}^{(\mathrm{nn})}(z)\exp(i\mathbf{h}\cdot\mathbf{r}_{\|})\right) = C\sum_{\mathrm{nn}} \mathrm{e}_{\mathbf{h}}^{(\mathrm{nn})}(z)\exp(i\mathbf{h}\cdot\mathbf{r}_{\|}) \tag{2}$$

and the same relation for the 2nn or higher shell, with the same C. For example, $\mathbf{h} = (1, 0) \equiv \mathbf{h}_1$ in Eq. (2), operation on the left goes as

$$\begin{aligned} g\left(\mathrm{e}_{\mathbf{h}_1}(z)\exp(i\mathbf{h}_1\cdot\mathbf{r}_{\|})\right) &= (g\mathrm{e}_{\mathbf{h}_1}(z))\exp(i\mathbf{h}_1\cdot g^{-1}\mathbf{r}_{\|}) \\ &= (g\mathrm{e}_{\mathbf{h}_1}(z))\exp(i(g\mathbf{h}_1)\cdot\mathbf{r}_{\|}) \end{aligned} \tag{3}$$

The vector $g\mathrm{e}_{\mathbf{h}_1}(z)$ is a $\pi/2$ rotation of $\mathrm{e}_{\mathbf{h}_1}(z)$. Therefore, from Eq. (2), it should hold that

$$g\mathrm{e}_{\mathbf{h}_1}(z) = C\mathrm{e}_{\mathbf{h}_2}(z), \tag{4}$$

where $\mathbf{h}_2$ stands for the vector $g\mathbf{h}_1 = (0, 1)$. That is, $\mathrm{e}_{\mathbf{h}_1}(z)$ and $\mathrm{e}_{\mathbf{h}_2}(z)$, generally $\mathrm{e}_{\mathbf{h}}(z)$ for all h's in the nn shell, should be related mutually[5].

If Eq. (1) had a term belonging to the 0-shell with a vector amplitude $\mathrm{e}_0(z)$, it should satisfy

$$g\mathrm{e}_0(z) = C\mathrm{e}_0(z) \tag{5}$$

with the same C as used in Eq. (2), because $g0 = 0$. Therefore, by the operation of $g = \mathrm{C}_4$, the direction of $\mathrm{e}_0(z)$ should be invariant (for $C > 0$) or reversed (for $C < 0$). This is possible either when $\mathrm{e}_0(z)$ is directed in the z direction or when it is zero identically. When $\mathrm{e}_0(z) = 0$ (second case), the mode cannot be excited by a light of $\mathbf{k}_{\|} = 0$ because the mode has no term to be connected to the incoming field. When $\mathrm{e}_0(z)$ is directed in the $\pm z$ direction (first case), the mode cannot be excited either, because $\mathrm{e}_0(z)$ is perpendicular to the polarization of the incoming plane-wave light of $\mathbf{k}_{\|} = 0$. In dropping the 0-shell term in Eq. (1), we have omitted this irrelevant longitudinal case. Thus, the PB modes at $\mathbf{k}_{\|} = 0$ of one-dimensional irreducible representation are all OIMs.

Now we turn our attention to sending a photon to an OIM. We begin by finding an OIM numerically. Figure 1(a) shows the calculated reflectance of an s-polarized plane-wave light of $k_y = 0$. It is shown as a function of the frequency ω for a monolayer of dielectric spheres of refractive index $n = 1.437$ arrayed in a 2D square lattice ($a/d = 0.5$, a being the radius of a sphere). The value 1.437 is that of polytetrafluoroethylene (PTFE) in the millimeter wave region[11]. Thus, we are considering a millimeter light in this paper. We used the vector KKR algorithm to obtain Fig. 1[3,12]. The results are given in the region $0.78 < \omega < 0.8$ for several values of k_x. With decreasing k_x, we are approaching the case of normal incidence. With decreasing k_x, the frequency of the reflectance peak, which proves the existence of a mode of a slab PC[13], increases with both width and height of the peak becoming progressively smaller. Finally, at $k_x = 0$, we can no longer observe any trace of peak in the reflectance. This feature shows that the peak arises due to the excitation of an s-active PB when $k_x \neq 0$ and the mode tends to an OIM in the extreme limit of $k_x = 0$; i.e., at the Γ point[8].

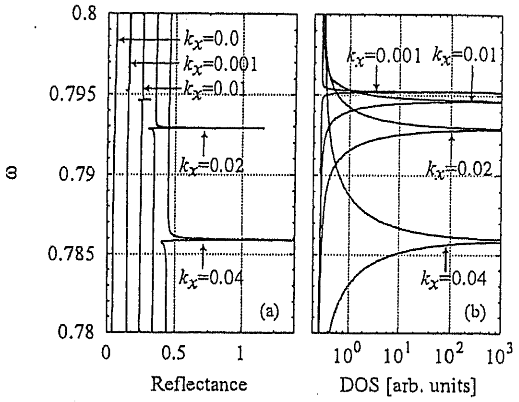

FIG. 1: Reflectance of s-polarized light (a) and DOS of the s-active modes (b) as functions of normalized frequency ω with k_x kept fixed. The frequency ω and wave vectors k are expressed in units of $2\pi c/d$ and $2\pi/d$, respectively. Here, c is the speed of light. Each of the spectra in (a) is displaced horizontally for clarity. The reflectance of $k_x = 0$ in (a) is that of normal incidence.

Figure 1(b) shows the calculated density of states (DOS) of PBs of the same system. The results were obtained by using the method described in Ref. 13, which yields DOS of optically active PBs. In accordance with the reflectance shown in Fig. 1(a), the frequency of the DOS peak becomes gradually higher and the width of the peak shows a rapid narrowing as k_x approaches 0. The narrowing of peak width shows that the radiative damping rate decreases towards the Γ point[8]. Figure 1 thus shows that in the limit $k_x \to 0$, the mode becomes unable to couple to the incident s-polarized light.

In this way, we have confirmed the existence of an OIM at the Γ point in the scanned frequency range. The OIM (its frequency ω_0 being $0.7954\times(2\pi c/d)$ at the Γ point) is identified to be an A_2 mode by the symmetry of $\mathrm{e}_{\mathbf{h}}^{(\mathrm{nn})}$ calculated for h's in the nn shell. We focus on this mode in the following.

To excite this OIM, which has a wave function of Eq. (1), we need to use an external probe having a lateral component $\mathbf{k}_{\|}$, which is equal to a reciprocal lattice vector $\mathbf{h}$ in nn or higher shells. In the free space, an incident plane-wave light of frequency ω with $\mathbf{k}_{\|} = \mathbf{h}$ exists in the frequency region $\omega/c > |\mathbf{h}|$, for it then has a real z component of the wave vector, equal to $(\omega^2/c^2 - |\mathbf{h}|^2)^{1/2}$. We assume $\mathbf{h}$ of the incident light to be one of the vectors in the nn shell, i.e., $\mathbf{h} = \mathbf{h}_1 = (1, 0)$. Thus, for ω

in the region $\omega > 2\pi c/d$, the mode at the Γ point is actually coupled to an outside plane-wave light of $\mathbf{k}_{\parallel} = \mathbf{h}$: in other words, PB modes of one-dimensional representation at the Γ point have a finite lifetime in this frequency region, due to radiation damping through the diffracted plane-waves. Strictly speaking, therefore, true OIMs of infinite lifetime at the Γ point exist only in the region $\omega < 2\pi c/d$. If we could somehow forward a photon in this frequency region to an OIM, it would remain there forever (in neglect of decay channels other than radiation). The absence of radiative leakage is, however, equivalent to the absence of its time-reversal counterpart, i.e., the absence of an external excitation probe that couples to this OIM. Let us next discuss a means to send a photon to this mode.

In the frequency region $0 < \omega < 2\pi c/d$, the incident light of $\mathbf{k}_{\parallel} = \mathbf{h}^{(nn)}$ is evanescent. In this case, we can use attenuated total reflection (ATR) geometry for our purpose, as shown in Fig. 2. Figure 3(a) shows the band structure along the Γ-X axis near the Γ point obtained by plotting the peak positions of DOS (including those shown in Fig. 1(b)). We present the band structure near the Γ point with the point $k_x = 2\pi/d$ taken at the center of the horizontal axis, making use of the periodicity of the band structure with respect to k_x. The three straight lines show the dispersion relations of the evanescent light that are obtained when the total reflection occurs in the prism of refractive index n_p. Inside the prism, ω and k_x are related by

$$k_x = \frac{\omega}{c} n_p \sin\theta_p, \qquad (6)$$

where θ_p is the angle of plane-wave light at the exit surface of the prism, as shown in Fig. 2. For simplicity, we treat a prism with semi-infinite thickness to eliminate unessential Fabry-Perot type oscillations. For the case of $n_p = 2$, the case we study in what follows, total reflection occurs for $\theta_p > 30.0°$, where it is an evanescent light of $k_x = 2\pi/d$ that comes into the PC. We consider the case of varying ω with fixed θ_p in the ATR geometry. To observe an OIM present at the Γ point with a frequency ω_0, it is necessary to adjust θ_p so that the evanescent light has $k_x = 2\pi/d$ just at $\omega = \omega_0$. From Eq. (6), this matching is realized when $\theta_p = 39.0°$. In Fig. 3(a), three dispersion curves of evanescent light for $\theta_p = 39.0°$, $40.0°$ and $42.0°$ are shown.

The ATR spectrum, the ω dependence of the squared amplitude of the totally reflected light inside the prism, is calculated by taking into account the multiple scattering between the PC and the prism[14]. If the evanescent light from the prism excites a mode in the PC, the ATR spectrum has a dip because a part of the energy of the incident light escapes to the excited PB. Thus, once the OIM of the Γ point is indeed excited, the spectrum obtained with $\theta_p = 39.0°$ has a dip. Photonic modes excited by probes other than that of $\theta_p = 39.0°$ have a finite k_x value and can be excited by the incident light as a usual leaky mode.

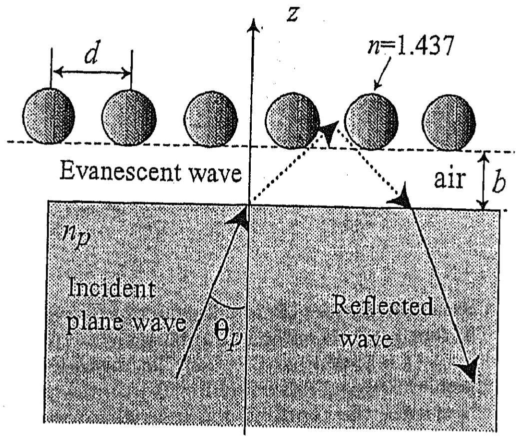

FIG. 2: ATR geometry composed of a prism and a slab photonic crystal. Solid and dotted arrows show the direction of the flows of a plane-wave and evanescent wave, respectively. The refractive index of the prism is n_p, and the spacing between the prism and the photonic crystal is b.

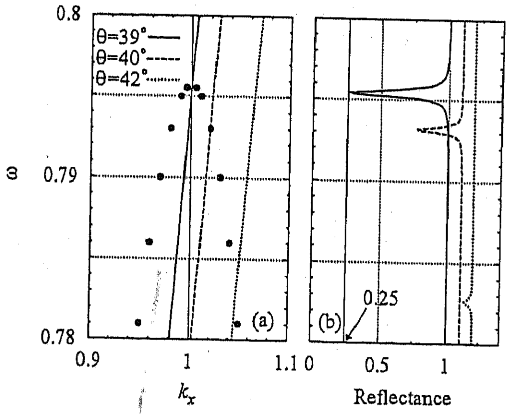

FIG. 3: Band diagram around $k_x = 2\pi/d$ (a) and ATR spectra (specular reflectance) (b). The three straight lines in (a) show the dispersion relations of the evanescent waves for three θ_p with $n_p = 2.0$. Panel (b) shows ATR spectra of the three θ_p of (a) for $b = d/2$ (see Fig. 2). For clarity, the spectra are offset horizontally by 0.1 from one another. To emphasize the value 0.25 of the reflectance dip, the vertical line is given by a thin solid line.

Figure 3(b) shows ATR spectra (specular reflectance) of the incident light of $\mathbf{k}_{\parallel} = \mathbf{h}_1 \equiv (1, 0)$ for the three values of θ_p examined in Fig. 3(a). It shows that the evanescent light incident with $\theta_p = 39.0°$ (solid line) indeed excites the OIM. The breadth of the dip is a measure of the lifetime of the excited OIM, which is now caused by its coupling with the plane-wave lights in the prism region. The signal due to the OIM just at $\theta_p = 39.0°$ is seen to be the most prominent in the ATR signal. The other two fine structures for $\theta_p = 40.0°$ and $42.0°$ are smaller, implying that the coupling between the evanes-

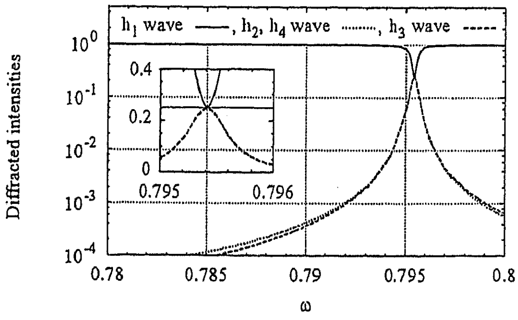

FIG. 4: Intensities of four diffracted plane-waves in the prism. The four $\mathbf{h}$ points of the nn shell are $\mathbf{h}_1 = (1, 0)$, $\mathbf{h}_2 = (0, 1)$, $\mathbf{h}_3 = (-1, 0)$ and $\mathbf{h}_4 = (0, -1)$. The intensity of the $\mathbf{h}_1$ wave is the ATR signal shown in Fig. 3(b). In the magnified panel of the inset, the horizontal line is given at the intensity 0.25.

cent light and a leaky mode is relatively small.

We can thus catch OIMs at the Γ point by ATR geometry. This result can find the following application; if we switch off the ATR coupling by some means immediately after forwarding a photon to the OIM, it stays there for a long time. In an ideal case, we can thereby use a PC as a temporary container of photons.

The fact that the minimum value of the ATR dip at exact resonance ($\theta_p = 39.0°$) is 0.25 in Fig. 3(b) is not accidental. As shown in Eq. (1), the OIM consists of four plane-waves of $\mathbf{h}$ in the nn shell, whose amplitudes $e_{\mathbf{h}}^{(nn)}(z)$ are of equal magnitudes by symmetry. Excitation of the Bloch state of Eq. (1) is equivalent to the excitation of these four plane-waves in the nn shell with equal amplitudes. They then give rise to four evanescent lights in the region between the PC and prism, which are finally converted into plane-waves in the prism region. Reflecting the identical magnitudes $|e_{\mathbf{h}}^{(nn)}|$ for four $\mathbf{h}$'s, these plane-waves should have equal intensities. Their intensities in the prism are plotted in Fig. 4. The inset shows that the intensity of each of the four plane-waves is indeed 0.25 at $\omega = \omega_0$. Thus, the light of unit intensity incident at $\theta = 39.0°$ is equipartitioned by four diffracted plane-wave lights of $\mathbf{h}_1$, $\mathbf{h}_2$, $\mathbf{h}_3$ and $\mathbf{h}_4$, as is explicit in the wave form at the Γ point given by Eq. (1). Interestingly, the value 0.25 is guaranteed by the equipartition, however large the distance may be between the PC and prism. Namely, as the distance b becomes larger and the prism-PC coupling gets smaller, the signal profiles of the OIM excitation become sharper reflecting the increase of the induced lifetime of the OIM but the dip and peak values remain fixed at the value 0.25.

Finally, the scaling property of Maxwell's equations shows that the present results may be applied to PCs of arbitrary lattice constant. Also, the use of a monolayer PC such as that examined in this paper is not essential. Results for stacked PCs can be easily obtained by using the layer doubling method[3], which produces essentially the same results except for quantitative details.

In summary, we have shown that optically inactive modes appearing at the Γ point of the Brillouin zone can be detectable by using a plane-polarized incident light of oblique incidence in the ATR geometry.

This work was financially supported by a Grant-in-Aid from the Ministry of Education, Sports and Culture of Japan and from a grant for "Promotion of Science and Technology" from the same ministry.

---

[1] J. D. Joannopoulos, R. D. Meade, and J. N. Winn, *Photonic Crystals* (Princeton University Press, Princeton, 1995).

[2] K. Sakoda, *Optical Properties of Photonic Crystals* (Springer Veriag, Berlin, 2001).

[3] N. Stefanou, V. Karathanos, and A. Modinos, J. Phys.: Condens. Matter **4**, 7389 (1992).

[4] W. M. Robertson, G. Arjavalingam, R. D. Meade, K. D. Brommer, A. M. Rappe, and J. D. Joannopoulos, Phys. Rev. Lett. **68**, 2023 (1993).

[5] K. Ohtaka and Y. Tanabe, J. Phys. Soc. Jpn, **65**, 2670 (1996).

[6] P. Paddon and J. F. Young, Phys. Rev. B **61**, 2090 (2000).

[7] T. Ochiai and K. Sakoda, Phys. Rev. B **63**, 125107 (2001).

[8] S. Fan and J. D. Joannopoulos, Phys. Rev. B **65**, 235112 (2002).

[9] See, e.g., T. Inui, Y. Tanabe, and Y. Onodera, *Group Theory and Its Applications in Physics* (Springer, Berlin, 1990).

[10] H. Miyazaki and K. Ohtaka, Phys. Rev. B **58**, 6920 (1998).

[11] We are planning to carry out an experiment using this photonic crystal.

[12] K. Ohtaka, Phys. Rev. B **19**, 5057 (1979).

[13] K. Ohtaka, Y. Suda, S. Nagano, T. Ueta, A. Imada, T. Koda, J. S. Bae, K. Mizuno, S. Yano, and Y. Segawa, Phys. Rev. B **61**, 5267 (2000).

[14] Y. Kurokawa and H. Miyazaki, Phys. Rev. B **65**, 201102 (2002).

Derivation of the density of states of leaky photonic bands

Kazuo Ohtaka and Jun-ichi Inoue
Center for Frontier Science, Chiba University
1-33 Yayoi-cho, Inage-ku, Chiba 263-8522, Japan

Syuuichi Yamaguti
Graduate School of Science and Technology, Chiba University
1-33 Yayoi-cho, Inage-ku, Chiba 263-8522, Japan

(Dated: March 12, 2004)

This paper presents the formula for the density of states (DOS) of photonic bands (PBs) in the leaky region of the phase space of a slab-type photonic crystal. It is expressed by the eigenphase shifts of the scattering matrix defined in terms of the complex transmission and reflection amplitudes of plane-wave external incident light. The derivation is given for the general case where a number of diffracted plane-wave lights are produced by the incident lights. The DOS profile calculated as a function of frequency and wave vector enables us to obtain the dispersion relation and lifetime of leaky PBs. The usefulness of the derived formula is demonstrated by applying it to the PB structure of dielectric spheres, arrayed periodically to form a photonic crystal of finite thickness.

PACS numbers: 42.70.Qs

I. INTRODUCTION

Photonic crystals (PCs) are usually practically applied by preparing a system of finite thickness. When a photonic band (PB) mode is leaky, i.e. when its momentum and frequency lie within the light cone in phase space $(\mathbf{k}, \omega)$, its finite lifetime decisively influences the capability of that mode in technological applications. Due to the lack of translational symmetry in a PC of finite thickness, the treatment of the lifetime caused by the leakage of PB modes through the PC surfaces is not at all straightforward. This is in clear contrast to an ideal PC of infinite size, where we can formulate a band-structure calculation as a standard eigenvalue problem of real eigenvalues.[1] In calculating the lifetime of a leaky PB mode, we must take account of its coupling with the plane-wave states of the exterior region of a PC,[2,3] which by definition have a continuous spectrum of the density of states (DOS). For electrons, the finite lifetime of an electronic state resulting from its coupling with the other states of a continuous spectrum has been given much attention in the physics of metal, giving us some interesting topics, such as the Kondo effect and heavy fermions in Kondo lattices.[4] Although the basic mixing mechanisms of electrons and photons are conceptually very similar, one important point in the photonic problem in PCs is the need to obtain the lifetime and dispersion relation of PBs with a precision high enough to be integrated into a device design.

The purpose of the present paper is to present a method of calculating the DOS of leaky PBs of slab PCs, from which the dispersion and lifetime of PBs are both obtained precisely. The method is based on the calculation of a scattering matrix (S matrix) for a set of external lights incident simultaneously on the slab PC. We diagonalize the S matrix to obtain the eigenphase shifts, which determine the phase changes of the incident light passing through or reflecting back from the system. Conceptually, the scattering phase shift of an external probe relative to its free-space propagation is a standard quantity used to examine a target black box (for example, the Friedel sum rule for the screening of an impurity potential by electron cloud[5]). The formula of the DOS of PBs derived in this paper is expressed by the frequency derivative of the sum of the eigenphase shifts. The derivation of the DOS formula is given for a general case, where an arbitrary number of diffracted lights emerge simultaneously from a PC slab. Such a general treatment is important because the presence of diffraction characterizes the light scattering from PCs. Although the method proposed here to derive the DOS of PBs is applicable only to the leaky modes, its usefulness is obvious in the practical applications of PCs; any PB mode to be excited by an external light or to be used as a source of emitted light should be regarded as leaky in the sense that it is used through the coupling to the exterior free space. Some examples are light transmission and reflection in slab PCs,[6] extraction of laser light through PC surfaces,[7] and Smith-Purcell radiation from a charge traveling parallel to PC surfaces.[8–10] The efficiency of these phenomena depends critically on the lifetime of the leaky PBs involved. In other words, precise estimation of their lifetime is a crucial task in the physical and technological applications of PBs.

In Sec. 2, we define the S matrix of a slab PC and derive the eigenvalue equation for the PB modes set up in it, taking into account their leakage. The formula is obtained in Sec. 3 for the increment of DOS due to the presence of a slab PC relative to that of free space by counting the number of solutions of the eigenvalue equation. An application of the derived formula is given in Sec. 4 for a number of slab PCs of arrayed spheres. We illustrate there how to calculate the dispersion relation and lifetime of leaky PBs from the DOS profile. A brief summary is given in Sec. 5.

II. SCATTERING MATRIX AND ITS EIGENVALUES

A. Definition of scattering channels

We consider a slab PC extending in the x, y direction with the origin of coordinates $\mathbf{r} = 0$ taken at its center. The periodicity of the slab is assumed to be perfect in the lateral plane $-\infty < x, y < \infty$. We use a symbol $\mathbf{h}$ to denote a two dimensional (2D) reciprocal lattice (RL) point in the xy plane. The vector $\mathbf{h}$ specifies a diffracted wave, reflected or transmitted. Let ω be the frequency and $\mathbf{k}$ the wave vector of an incident plane-wave light. We make explicit the direction of propagation of a light by assigning a superscript $\pm$ to various quantities, $+$ to the quantities associated with the waves propagating to the $+z$ side of the slab from the $-z$ side. For example, the inciden light of $\mathbf{k}^+$ ($\mathbf{k}^-$) stands for the light which is incident on the slab towards the $+z$ ($-z$) side, i.e., the light coming to the slab PC from below (above). Let $\mathbf{k}_\parallel$ be the component of the wave vector of $\mathbf{k}$ parallel to the xy plane.

$$\mathbf{k}_\parallel = (k_x,\, k_y) \tag{1}$$

The translational invariance in the lateral plane shows that all the normal modes (actually they may be lifetime-broadened) of this system are specified by the lateral wave-vector components.

From the dispersion relation of light in free space,

$$\mathbf{k}^\pm = (\mathbf{k}_\parallel, \pm\Gamma_0) = (k_x, k_y, \pm\Gamma_0) \tag{2}$$

with

$$\Gamma_0 = \sqrt{\omega^2/c^2 - k_\parallel^2}. \tag{3}$$

In the same way, the wave vector $\mathbf{k}^\pm_{\mathbf{h}}$ of diffracted light in the region outside the PC is defined to be

$$\mathbf{k}^\pm_{\mathbf{h}} = (\mathbf{k}_\parallel + \mathbf{h}, \pm\Gamma_{\mathbf{h}}) \tag{4}$$

with

$$\Gamma_{\mathbf{h}} \equiv \Gamma_{\mathbf{h}}(\omega) = \sqrt{\omega^2/c^2 - (\mathbf{k}_\parallel + \mathbf{h})^2}. \tag{5}$$

Only in the case where

$$\omega > c|\mathbf{k}_\parallel + \mathbf{h}|, \tag{6}$$

$\mathbf{h}$ diffracted light comes out of the PC as plane-wave light, which is observable at an observation point far from the PC. If Eq. (6) does not hold, the $\mathbf{h}$-wave is evanescent with a pure imaginary $\Gamma_{\mathbf{h}}$. We call the channel $\mathbf{h}$ of real $\Gamma_{\mathbf{h}}$ an open channel and $\mathbf{h}$ of imaginary $\Gamma_{\mathbf{h}}$as a closed channel. For a fixed ω, each $\mathbf{h}$ defines one diffraction channel. All the channels other than those with smaller $|\mathbf{h}|$ are closed. The number of open channels at a given ω equals the number of $\mathbf{h}$'s that satisfy Eq. (6).

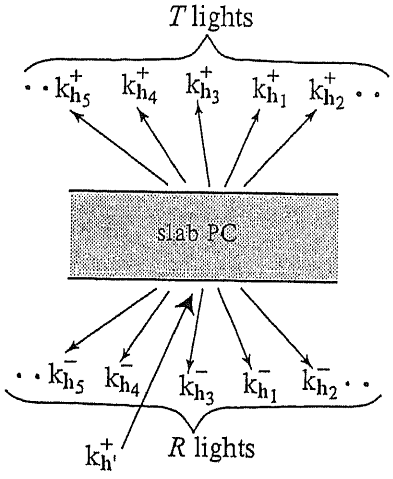

FIG. 1: T and R lights, both N in number, produced by an incident $\mathbf{k}^+_{\mathbf{h}'}$ light.

Let us suppose that we are in the frequency region where there are N diffraction channels open (one is the channel $\mathbf{h} = 0$). The incident light $\mathbf{k}^+$ coming from below the slab then gives rise to N transmitted lights (T lights) on the $+z$ side and N reflected lights (R lights) on the $-z$ side. Let

$$\mathbf{k}^+_{\mathbf{h}_1}, \mathbf{k}^+_{\mathbf{h}_2}, \ldots, \mathbf{k}^+_{\mathbf{h}_N}, \tag{7}$$

be the wave vectors of the T lights and

$$\mathbf{k}^-_{\mathbf{h}_1}, \mathbf{k}^-_{\mathbf{h}_2}, \ldots, \mathbf{k}^-_{\mathbf{h}_N}, \tag{8}$$

be those of the R lights. Let $\mathbf{h}_1$ stand for the channel $\mathbf{h} = 0$, which is open for any ω.

Suppose in an open channel $\mathbf{h}'$ we have an incident light of wave vector $\mathbf{k}^+_{\mathbf{h}'}$, which propagates towards the slab from below. This wave, too, is diffracted to produce T and R lights, each composed of N waves, as shown in Fig. 1. If the incident light has the form

$$\mathbf{a}^+_{\mathbf{h}'} e^{i\mathbf{k}^+_{\mathbf{h}'}\cdot\mathbf{r}} \tag{9}$$

with a specified complex vector amplitude $\mathbf{a}^+_{\mathbf{h}'}$, it produces the T (R) lights of wave vector $\mathbf{k}^+_{\mathbf{h}}$ ($\mathbf{k}^-_{\mathbf{h}}$), which are expressed by

$$\begin{aligned} &\mathbf{T}^{++}_{\mathbf{h}\mathbf{h}'} a^+_{\mathbf{h}'} \exp(i\mathbf{k}^+_{\mathbf{h}} \cdot \mathbf{r}), \\ &\mathbf{R}^{-+}_{\mathbf{h}\mathbf{h}'} a^+_{\mathbf{h}'} \exp(i\mathbf{k}^-_{\mathbf{h}} \cdot \mathbf{r}). \end{aligned} \tag{10}$$

The 3×3 tensor $\mathbf{T}^{++}_{\mathbf{h}\mathbf{h}'}$ of transmission describes the complex amplitude of the $\mathbf{h}$-wave in the process of the up-propagating $\mathbf{k}^+_{\mathbf{h}'}$ light being converted to the up-propagating $\mathbf{k}^+_{\mathbf{h}}$ wave. The tensor $\mathbf{R}^{-+}_{\mathbf{h}\mathbf{h}'}$ stands for the

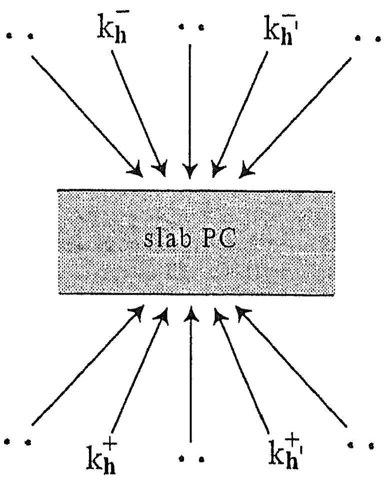

FIG. 2: Simultaneous incidence of N lights in the open channels from above and below the photonic crystal.

process of a $\mathbf{k}^+_{\mathbf{h}'}$ wave being reflected back as a $\mathbf{k}^-_{\mathbf{h}}$ wave. The element xy of, e.g., the tensor $\mathbf{T}^{++}_{\mathbf{hh}'}$,

$$(\mathbf{T}^{++}_{\mathbf{hh}'})_{xy}$$

is equal to the complex amplitude of the x component of the $\mathbf{k}^+_{\mathbf{h}}$ light, produced by a y-polarized $\mathbf{k}^+_{\mathbf{h}'}$ light, which is incident on the PC with unit amplitude. For an incident amplitude $\mathbf{a}^+_{\mathbf{h}'}$, the x component of the reflected light with wave vector $\mathbf{k}^-_{\mathbf{h}}$ is given by

$$(\mathbf{R}^{-+}_{\mathbf{hh}'}\mathbf{a}^+_{\mathbf{h}'})_x = \sum_{i=x,y,z} (\mathbf{R}^{-+}_{\mathbf{hh}'})_{xi}\,(\mathbf{a}^+_{\mathbf{h}'})_i\,. \tag{11}$$

We will now consider the situation of the simultaneous incidence of the N plane-waves. Let

$$\mathbf{k}^+_{\mathbf{h}_1}, \mathbf{k}^+_{\mathbf{h}_2}, \ldots, \mathbf{k}^+_{\mathbf{h}_N}$$

and

$$\mathbf{k}^-_{\mathbf{h}_1}, \mathbf{k}^-_{\mathbf{h}_2}, \ldots, \mathbf{k}^-_{\mathbf{h}_N}$$

be the wave vectors of the incident lights from below and above the PC. This situation is shown in Fig. 2. This incidence condition still gives T and R lights, each composed of N plane-waves. After the scattering by the PC of all these incident lights, the amplitude of the $\mathbf{k}^+_{\mathbf{h}}$ wave that appears on the $+z$ side of the PC has the form

$$\sum_{\mathbf{h}'} \left(\mathbf{T}^{++}_{\mathbf{hh}'}\mathbf{a}^+_{\mathbf{h}'} + \mathbf{R}^{+-}_{\mathbf{hh}'}\mathbf{a}^-_{\mathbf{h}'}\right), \tag{12}$$

where the summation over $\mathbf{h}'$ runs over open channels.

B. Flux conservation and S matrix

Here, we examine the conservation of the energy flow in the scattering event described above. We enclose the slab PC in a large box as shown in Fig. 3. The z component of the Poynting vector of the $\mathbf{k}^+_{\mathbf{h}}$ wave, i.e. the outflow of energy towards the $+z$ direction through the surface of the box in the $+z$ side, is

$$c\left(\frac{\Gamma^+_{\mathbf{h}}}{\omega/c}\right)\frac{\varepsilon_0}{2}$$

times the absolute square of the electric field; the quantity in the parenthes being the directional cosine of the outgoing wave vector $\mathbf{k}^+_{\mathbf{h}}$ with the z axis. If we consider the flux conservation for the Poynting vector averaged over one unit cell of the 2D lattice of a lateral plane, the interference terms between different $\mathbf{h}$'s disappear and the sum of the energy flows of all the open channels provides the total outflow in the $+z$ direction. Similarly, we can express the outflow in the $-z$ direction below the PC. The sum of the two then gives

$$[P^+_z - P^-_z]_{\text{outflow}} = \frac{\varepsilon_0}{2}\frac{c^2}{\omega}\sum_{\mathbf{h}}\Gamma_{\mathbf{h}}\left|\sum_{\mathbf{h}'}(\mathbf{T}^{++}_{\mathbf{hh}'}\mathbf{a}^+_{\mathbf{h}'} + \mathbf{R}^{+-}_{\mathbf{hh}'}\mathbf{a}^-_{\mathbf{h}'})\right|^2 + \frac{\varepsilon_0}{2}\frac{c^2}{\omega}\sum_{\mathbf{h}}\Gamma_{\mathbf{h}}\left|\sum_{\mathbf{h}'}(\mathbf{R}^{-+}_{\mathbf{hh}'}\mathbf{a}^+_{\mathbf{h}'} + \mathbf{T}^{--}_{\mathbf{hh}'}\mathbf{a}^-_{\mathbf{h}'})\right|^2. \tag{13}$$

Here P^+_z and P^-_z are the z components of the Poynting vectors of the $+$ waves and $-$ waves. This quantity equals the energy inflow of the incident lights, which has the form

$$[P^+_z - P^-_z]_{\text{inflow}} = \frac{\varepsilon_0}{2}\frac{c^2}{\omega}\sum_{\mathbf{h}'}\left(\Gamma_{\mathbf{h}'}|\mathbf{a}^+_{\mathbf{h}'}|^2 + \Gamma_{\mathbf{h}'}|\mathbf{a}^-_{\mathbf{h}'}|^2\right) \tag{14}$$

in the simultaneous incidence.

In expressing the flux conservation

$$[P^+_z - P^-_z]_{\text{inflow}} = [P^+_z - P^-_z]_{\text{outflow}}, \tag{15}$$

which should hold for arbitrary incident amplitudes $\{\mathbf{a}^+_{\mathbf{h}'}\}$ and $\{\mathbf{a}^-_{\mathbf{h}'}\}$, we introduce the matrix notation. First, $3N\times$

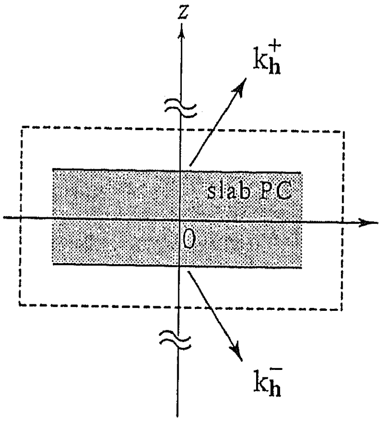

FIG. 3: A box surrounding the slab PC to consider the flux conservation between the incoming and outgoing lights.

$3N$ matrices $\mathbf{T}^{++}$ are defined by

$$\mathbf{T}^{++} = \begin{pmatrix} \mathbf{T}^{++}_{\mathbf{h}_1\mathbf{h}_1} & \mathbf{T}^{++}_{\mathbf{h}_1\mathbf{h}_2} & \mathbf{T}^{++}_{\mathbf{h}_1\mathbf{h}_3} & \cdots & \mathbf{T}^{++}_{\mathbf{h}_1\mathbf{h}_N} \\ \mathbf{T}^{++}_{\mathbf{h}_2\mathbf{h}_1} & \mathbf{T}^{++}_{\mathbf{h}_2\mathbf{h}_2} & \mathbf{T}^{++}_{\mathbf{h}_2\mathbf{h}_3} & \cdots & \mathbf{T}^{++}_{\mathbf{h}_2\mathbf{h}_N} \\ \mathbf{T}^{++}_{\mathbf{h}_3\mathbf{h}_1} & \mathbf{T}^{++}_{\mathbf{h}_3\mathbf{h}_2} & \mathbf{T}^{++}_{\mathbf{h}_3\mathbf{h}_3} & \cdots & \mathbf{T}^{++}_{\mathbf{h}_3\mathbf{h}_N} \\ \vdots & \vdots & \vdots & \ddots & \vdots \\ \mathbf{T}^{++}_{\mathbf{h}_N\mathbf{h}_1} & \mathbf{T}^{++}_{\mathbf{h}_N\mathbf{h}_2} & \mathbf{T}^{++}_{\mathbf{h}_N\mathbf{h}_3} & \cdots & \mathbf{T}^{++}_{\mathbf{h}_N\mathbf{h}_N} \end{pmatrix} \qquad (16)$$

in terms of a 3×3 tensor $\mathbf{T}^{++}_{\mathbf{h}_1\mathbf{h}_2}$ introduced in Eq. (10). Matrices $\mathbf{T}^{--}$ and $\mathbf{R}^{+-}$ are similarly defined using the tensors $\mathbf{T}^{--}_{\mathbf{h}_1\mathbf{h}_2}$ and $\mathbf{R}^{+-}_{\mathbf{h}_1\mathbf{h}_2}$. Also, we introduce the $3N \times 3N$ diagonal matrix $\mathbf{\Gamma}$ defined by

$$\mathbf{\Gamma} = \begin{pmatrix} \mathbf{\Gamma}_{\mathbf{h}_1} & 0 & 0 & \dots & 0 \\ 0 & \mathbf{\Gamma}_{\mathbf{h}_2} & 0 & \dots & 0 \\ 0 & 0 & \mathbf{\Gamma}_{\mathbf{h}_3} & \dots & 0 \\ \vdots & \vdots & \vdots & \ddots & \vdots \\ 0 & 0 & 0 & \dots & \mathbf{\Gamma}_{\mathbf{h}_N} \end{pmatrix} = \mathbf{\Gamma}_{\mathbf{h}_n} \delta_{\mathbf{h}_n\mathbf{h}_m}, \qquad (17)$$

where the 3×3 matrix $\mathbf{\Gamma}_{\mathbf{h}_n}$ is

$$\mathbf{\Gamma}_{\mathbf{h}_n} = \begin{array}{c} \\ x \\ y \\ z \end{array} \begin{array}{c} \begin{array}{ccc} x & y & z \end{array} \\ \begin{pmatrix} \Gamma_{\mathbf{h}_n} & 0 & 0 \\ 0 & \Gamma_{\mathbf{h}_n} & 0 \\ 0 & 0 & \Gamma_{\mathbf{h}_n} \end{pmatrix} \end{array}. \qquad (18)$$

Using four block matrices, $\mathbf{T}^{++}$, etc., and $\mathbf{\Gamma}$, we introduce the following $6N \times 6N$ matrices $\widehat{\mathbf{S}}'$ and $\widehat{\mathbf{\Gamma}}'$

$$\widehat{\mathbf{S}}' = \begin{pmatrix} \mathbf{T}^{++} & \mathbf{R}^{+-} \\ \mathbf{R}^{-+} & \mathbf{T}^{--} \end{pmatrix} \qquad (19)$$

and

$$\widehat{\mathbf{\Gamma}}' = \begin{pmatrix} \mathbf{\Gamma} & 0 \\ 0 & \mathbf{\Gamma} \end{pmatrix}. \qquad (20)$$

They are both $6N \times 6N$ matrices because one RL point $\mathbf{h}$ has two channels ($\mathbf{h}+$) and ($\mathbf{h}-$) and each of the two channels has three degrees of freedom.

The flux conservation Eq. (15) is then expressed simply as

$$\left[\widehat{\mathbf{S}}'\right]^\dagger \widehat{\mathbf{\Gamma}}'\widehat{\mathbf{S}}' = \widehat{\mathbf{\Gamma}}', \qquad (21)$$

where the dagger stands for the hermitian conjugate. Finally, we define matrix $\widehat{\mathbf{S}}$ by

$$\widehat{\mathbf{S}} = \left[\widehat{\mathbf{\Gamma}}'\right]^{\frac{1}{2}} \widehat{\mathbf{S}}' \left[\widehat{\mathbf{\Gamma}}'\right]^{-\frac{1}{2}}. \qquad (22)$$

An explicit form of the ($\mathbf{h}+$, $\mathbf{h}'-$) block of $\widehat{\mathbf{S}}$ is

$$\left[\widehat{\mathbf{S}}\right]^{+-}_{\mathbf{hh}'} = \Gamma_{\mathbf{h}}{}^{\frac{1}{2}} [\mathbf{R}^{+-}]_{\mathbf{hh}'} \Gamma_{\mathbf{h}'}{}^{-\frac{1}{2}}. \qquad (23)$$

The ($\mathbf{h}-$, $\mathbf{h}'+$), ($\mathbf{h}+$, $\mathbf{h}'+$), and ($\mathbf{h}-$, $\mathbf{h}'-$) blocks of the S matrix are given by replacing $\mathbf{R}^{+-}$ of this equation by $\mathbf{R}^{-+}$, $\mathbf{T}^{++}$, and $\mathbf{T}^{--}$, respectively, according to the definition of $\widehat{\mathbf{S}}'$ [Eq. (19)].

The flux conservation expressed by Eq. (21) is now rewritten compactly as

$$\widehat{\mathbf{S}}^\dagger \widehat{\mathbf{S}} = \mathbf{I}. \qquad (24)$$

The matrix $\widehat{\mathbf{S}}$ is thus a $6N \times 6N$ unitary matrix. Therefore, it has $6N$ eigenvalues of the form $e^{2i\delta^{(j)}}$ (j = 1, 2, ..., $6N$) with a real phase $\delta^{(j)}$. The matrix element of S,

$$S_{\mathbf{h}'+x,\mathbf{h}-y},$$

for example, is a complex scattering amplitude in the process of the incident light of unit amplitude of $(\mathbf{h}, -, y)$ [a y-polarized light in the ($\mathbf{h}-$) channel] exiting out of the PC as an $(\mathbf{h}', +, x)$ light. We call $\delta^{(j)}$ an eigenphase shift. For $N = 1$, i.e. when only a direct transmitted light and a specularly reflected light of $\mathbf{h} = \mathbf{0}$ are produced by an incident light, we have six eigenphase shifts. We should have four eigenphase shifts instead of six, because we are dealing with the scattering of the incident *transverse* waves that give rise to *transverse* outgoing waves after the scattering.[11] This implies that out of six eigenphase shifts, two are meaningless. In the general case of N open channels, having $6N$ eigenphase shifts from a $6N \times 6N$ matrix S, $2N$ out of $6N$ eigenphase shifts are meaningless; they appear due to the longitudinal component of polarization.

Such irrelevant eigenphase shifts had better be eliminated from a practical point of view. For this purpose, the local coordinate systems defined in reference to each of the open channels are convenient. For a wave of channel ($\mathbf{h}+$) or ($\mathbf{h}-$), we define the right-handed system {123} using the three orthonormal vectors

$$\left(\mathbf{e_h}^{\pm}(1), \mathbf{e_h}^{\pm}(2), \mathbf{e_h}^{\pm}(3)\right), \qquad (25)$$

$\mathbf{e}^+_{\mathbf{h}}(1)$ and $\mathbf{e}^+_{\mathbf{h}}(2)$ being perpendicular to $\mathbf{k}^+_{\mathbf{h}}$ and $\mathbf{e}^+_{\mathbf{h}}(3)$ being parallel to it. Thus, component 3 stands for the longitudinal polarization of $\mathbf{k}_{\mathbf{h}}^{+}$ light and axis 2 is always taken to be in the lateral plane, irrespective of $\mathbf{h}$. For the $\{123\}$ coordinates of the $(\mathbf{h}-)$ channel, we choose three orthonormal vectors $\mathbf{e}_{\mathbf{h}}^{-}(i)$ $(i = 1, 2, 3)$ to be the mirror images of $\mathbf{e}_{\mathbf{h}}^{+}(i)$. Note that the $\{123\}$ system differs from one channel to another. In this sense, we call the $\{123\}$ system a local coordinate system.

We may then rewrite the S matrix using the 1 and 2 components of each channel in place of x, y, z components. The actual procedure is given in Appendix A. This procedure removes all the longitudinal components, and we are left with a 2×2 matrix, which is denoted as $\widehat{\mathrm{T}}_{\mathbf{hh}'}^{++}$, etc.. By arranging $\widehat{\mathrm{T}}_{\mathbf{hh}'}^{++}$, $\widehat{\mathrm{R}}_{\mathbf{hh}'}^{+-}$, etc., according to the channel labels, we may construct a $4N \times 4N$ S matrix. Let us denote the matrix thus obtained as S

$$\mathrm{S} = \begin{pmatrix} \widehat{\mathrm{T}}^{++} & \widehat{\mathrm{R}}^{+-} \\ \widehat{\mathrm{R}}^{-+} & \widehat{\mathrm{T}}^{--} \end{pmatrix}, \qquad (26)$$

where $\widehat{\mathrm{T}}^{++}$ are block matrices formed by the array of 2×2 matrix $\widehat{\mathrm{T}}_{\mathbf{hh}'}^{++}$. Hereafter, we call S the S matrix.

When S operates on a $4N$-dimensional column vector composed of the incident amplitudes of open channels (expressed in the local coordinates), Eq. (12) shows that the result is the transmitted and reflected amplitudes produced by the simultaneous incidence in all the open channels. The eigenvalues of S are obtained by the equation

$$\mathrm{S}\mathbf{v}^{(j)} = \lambda^{(j)}\mathbf{v}^{(j)}, \qquad (27)$$

with

$$\lambda^{(j)} = e^{2i\delta^{(j)}}, \qquad (28)$$

for $j = 1, 2, \ldots, 4N$. Explicitly, the eigenvector $\mathbf{v}^{(j)}$, a $4N$-dimensional column vector, has the form

$$\left(\mathbf{v}^{(j)}\right)^{t} = \left(v_{\mathbf{h}_1+}^{(j)}(1), v_{\mathbf{h}_1+}^{(j)}(2), \ldots, v_{\mathbf{h}_n+}^{(j)}(1), v_{\mathbf{h}_n+}^{(j)}(2),\ v_{\mathbf{h}_1-}^{(j)}(1), v_{\mathbf{h}_1-}^{(j)}(2), \ldots, v_{\mathbf{h}_n-}^{(j)}(1), v_{\mathbf{h}_n-}^{(j)}(2)\right). \qquad (29)$$

The form of the transposed vector of $\mathbf{v}^{(j)}$ has been given with (1) and (2) specifying two transverse components of each channel. Note that S and hence $\lambda^{(j)}$ and $\mathbf{v}^{(j)}$ all depend on $\mathbf{k}_{\|}$. For simplicity, we use the symbols S, $\lambda^{(j)}$ and $\mathbf{v}^{(j)}$ without adding the suffix $\mathbf{k}_{\|}$ to indicate the $\mathbf{k}_{\|}$ dependence.

The purpose of introducing $\delta^{(j)}$ for the eigenvalue $\lambda^{(j)}$ in Eqs. (27) and (28) is to express the frequencies of normal-modes and hence their DOS by using the eigenphase shifts. To proceed further, we assume the mirror symmetry with respect to the xy plane. Most artificially fabricated PCs belong to this category.

When the xy plane is a mirror plane (for the case of no mirror symmetry, see the comment at the end of this section), we can classify the modes by their parities of this mirror reflection. Since S commutes with this mirror operation, we have even- and odd-parity modes with the property of the eigenvector given by

$$\begin{aligned} v_{\mathbf{h}_l+}^{(j)}(1) &= v_{\mathbf{h}_l-}^{(j)}(1),\, v_{\mathbf{h}_l+}^{(j)}(2) = v_{\mathbf{h}_l-}^{(j)}(2), \quad (l = 1 \sim N) \quad \text{for even-parity modes,} \\ v_{\mathbf{h}_l+}^{(j)}(1) &= -v_{\mathbf{h}_l-}^{(j)}(1),\, v_{\mathbf{h}_l+}^{(j)}(2) = -v_{\mathbf{h}_l-}^{(j)}(2), \quad (l = 1 \sim N) \quad \text{for odd-parity modes.} \end{aligned} \qquad (30)$$

Let us assign the index $j = 1, 2, \cdots, 2N$ to the even-parity modes and $j = 2N+1, 2N+2, \cdots, 4N$ to the odd-parity modes. From now on, we shall focus on the even-parity modes.

Equations (27) and (28) imply the following. We let the wave

$$\mathbf{v}_{\mathbf{h}-}^{(j)} e^{i\mathbf{k}_{\mathbf{h}}^{-}\cdot\mathbf{r}} = \begin{pmatrix} v_{\mathbf{h}-}^{(j)}(1) \\ v_{\mathbf{h}-}^{(j)}(2) \end{pmatrix} e^{i\mathbf{k}_{\mathbf{h}}^{-}\cdot\mathbf{r}} \qquad (31)$$

propagate to the PC from above in the channel $(\mathbf{h}-)$ and another wave

$$\mathbf{v}_{\mathbf{h}+}^{(j)} e^{i\mathbf{k}_{\mathbf{h}}^{+}\cdot\mathbf{r}} = \begin{pmatrix} v_{\mathbf{h}+}^{(j)}(1) \\ v_{\mathbf{h}+}^{(j)}(2) \end{pmatrix} e^{i\mathbf{k}_{\mathbf{h}}^{+}\cdot\mathbf{r}} \qquad (32)$$

propagate from below in the channel $(\mathbf{h}+)$ [see Eq. (29) for the definition of $\mathbf{v}_{\mathbf{h}+}^{(j)}$ and $\mathbf{v}_{\mathbf{h}-}^{(j)}$]. Suppose they are sent to the PC simultaneously with the waves of the other channels, specified, similarly by the jth eigenvector, as shown in Fig. 2. Since their amplitudes are set so that as a whole, they constitute the jth eigenvector $\mathbf{v}^{(j)}$ of S, the wave of any channel exits the PC after having acquired only a common phase change $2\delta^{(j)}$. Thus, for stationary wave propagation, the electric field of a channel $\mathbf{h}$ *above* the slab turns out to be

$$\mathbf{v}^{(j)}_{\mathbf{h}-} e^{i\mathbf{k}^-_{\mathbf{h}}\cdot\mathbf{r}} + e^{2i\delta^{(j)}} \mathbf{v}^{(j)}_{\mathbf{h}+} e^{i\mathbf{k}^+_{\mathbf{h}}\cdot\mathbf{r}} = e^{i\delta^{(j)}} \mathbf{v}^{(j)}_{\mathbf{h}+} e^{i(\mathbf{k}_\parallel+\mathbf{h})\cdot\rho} \times \cos(\Gamma_{\mathbf{h}} z + \delta^{(j)}), \quad (33)$$

where $\rho = (x,\, y)$. The first term expresses the incident light of Eq. (31) and the second is the light produced by the PC. Similarly, we find below the slab

$$\mathbf{v}^{(j)}_{\mathbf{h}+} e^{i\mathbf{k}^+_{\mathbf{h}}\cdot\mathbf{r}} + e^{2i\delta^{(j)}} \mathbf{v}^{(j)}_{\mathbf{h}-} e^{i\mathbf{k}^-_{\mathbf{h}}\cdot\mathbf{r}} = e^{i\delta^{(j)}} \mathbf{v}^{(j)}_{\mathbf{h}} e^{i(\mathbf{k}_\parallel+\mathbf{h})\cdot\rho} \times \cos(-\Gamma_{\mathbf{h}} z + \delta^{(j)}). \quad (34)$$

The property of even-parity modes, $\mathbf{v}^{(j)}_{\mathbf{h}+} = \mathbf{v}^{(j)}_{\mathbf{h}-} (\equiv \mathbf{v}^{(j)}_{\mathbf{h}})$ was used in Eqs. (33) and (34). Combining them, we find that the field of the channel $\mathbf{h}$ outside the slab has the form

$$e^{i\delta^{(j)}} \mathbf{v}^{(j)}_{\mathbf{h}} e^{i(\mathbf{k}_\parallel+\mathbf{h})\cdot\rho} \cos(\Gamma_{\mathbf{h}}|z| + \delta^{(j)}). \quad (35)$$

This expression, which has the form of a standing wave, is valid both above and below the PC and suits our purpose of determining the eigenvalues.

C. Boundary condition and frequencies of normal modes

To obtain the eigenvalues, we put the PC slab symmetrically between two perfect mirrors, as shown in Fig. 4. We place the mirrors at $z = \pm L$. To determine the normal modes of the whole space of $-L < z < +L$, which has the PC at the center, we impose the boundary condition that the lateral components of the electric field vanish at the mirrors.

To find a solution subject to this boundary condition, we superpose Eq. (35) over j and $\mathbf{h}$

$$\mathbf{E}(\mathbf{r}) = \sum_{\mathbf{h}=\mathbf{h}_1}^{\mathbf{h}_N} \sum_{j=1}^{2N} e^{i\delta^{(j)}} \mathbf{v}^{(j)}_{\mathbf{h}} e^{i(\mathbf{k}_\parallel+\mathbf{h})\cdot\rho} \cos(\Gamma_{\mathbf{h}}|z| + \delta^{(j)}) C_j, \quad (36)$$

with unknown coefficients C_j, which we determine so that $\mathbf{E}(\mathbf{r})$ satisfies the boundary condition. The lateral components are x and y, and they are obtained by returning from the local coordinates to the fixed coordinates, which are obtained by using the inverse of the matrix $\mathbf{R}^{\pm}_{\mathbf{h}}$ given by Eq. (A1). Retaining a 2×2 block of matrix $(\mathbf{R}^{\pm}_{\mathbf{h}})^{-1}$ for conversion from (1, 2) to $(x,\, y)$, we denote it as $\mathbf{r}^{+}_{\mathbf{h}}$. The procedure of Appendix A then leads to

$$\begin{pmatrix} E_x(\mathbf{r}) \\ E_y(\mathbf{r}) \end{pmatrix} = \sum_{\mathbf{h}=\mathbf{h}_1}^{\mathbf{h}_N} \sum_{j=1}^{2N} e^{i\delta^{(j)}} \mathbf{r}^{+}_{\mathbf{h}} \mathbf{v}^{(j)}_{\mathbf{h}} e^{i(\mathbf{k}_\parallel+\mathbf{h})\cdot\rho} \times \cos(\Gamma_{\mathbf{h}}|z| + \delta^{(j)}) C_j, \quad (37)$$

the product $\mathbf{r}^{+}_{\mathbf{h}}\mathbf{v}^{(j)}_{\mathbf{h}}$ giving a column vector composed of the x and y components of $\mathbf{v}^{(j)}_{\mathbf{h}}$. The right-hand side of this equation should vanish at the mirror surfaces at $z = \pm L$. Since the plane-waves $e^{i(\mathbf{k}_\parallel+\mathbf{h})\cdot\rho}$ of different $\mathbf{h}$'s are linearly independent, it then follows that

$$\sum_{j=1}^{2N} e^{i\delta^{(j)}} \mathbf{r}^{+}_{\mathbf{h}} \mathbf{v}^{(j)}_{\mathbf{h}} \cos(\Gamma_{\mathbf{h}} L + \delta^{(j)}) C_j = \mathbf{r}^{+}_{\mathbf{h}} \begin{pmatrix} \sum_{j=1}^{2N} e^{i\delta^{(j)}} v^{(j)}_{\mathbf{h}}(1) \cos(\Gamma_{\mathbf{h}} L + \delta^{(j)}) C_j \\ \sum_{j=1}^{2N} e^{i\delta^{(j)}} v^{(j)}_{\mathbf{h}}(2) \cos(\Gamma_{\mathbf{h}} L + \delta^{(j)}) C_j \end{pmatrix} = 0 \quad (38)$$

for all $\mathbf{h}$. As the determinant of the 2×2 matrix $\mathbf{r}^{+}_{\mathbf{h}}$ is not zero, the column vector of this equation should vanish.

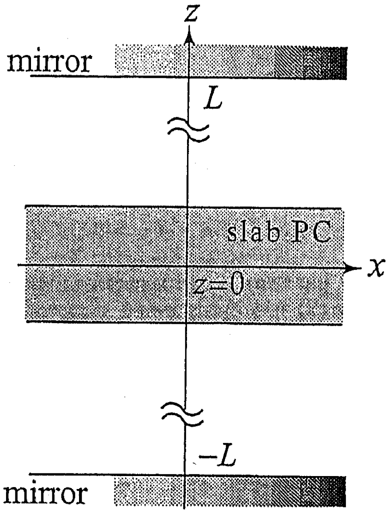

FIG. 4: Two parallel mirrors placed at $z = \pm L$ to consider the Fabry-Perot normal modes. We compare the number of the normal modes set up between the mirrors with and without the slab PC placed at $z = 0$.

Finally, the condition for any open channel $\mathbf{h}$ leads to

$$\begin{array}{cccc}
 & j=1 & 2 & \cdots \\
\mathbf{h}_1 & e^{i\delta^{(1)}}v^{(1)}_{\mathbf{h}_1}(1)\cos(\Gamma_{\mathbf{h}_1}L+\delta^{(1)}) & e^{i\delta^{(2)}}v^{(2)}_{\mathbf{h}_1}(1)\cos(\Gamma_{\mathbf{h}_1}L+\delta^{(2)}) & \cdots \\
\mathbf{h}_1 & e^{i\delta^{(1)}}v^{(1)}_{\mathbf{h}_1}(2)\cos(\Gamma_{\mathbf{h}_1}L+\delta^{(1)}) & e^{i\delta^{(2)}}v^{(2)}_{\mathbf{h}_1}(2)\cos(\Gamma_{\mathbf{h}_1}L+\delta^{(2)}) & \cdots \\
\mathbf{h}_2 & e^{i\delta^{(1)}}v^{(1)}_{\mathbf{h}_2}(1)\cos(\Gamma_{\mathbf{h}_2}L+\delta^{(1)}) & e^{i\delta^{(2)}}v^{(2)}_{\mathbf{h}_2}(1)\cos(\Gamma_{\mathbf{h}_2}L+\delta^{(2)}) & \cdots \\
\mathbf{h}_2 & e^{i\delta^{(1)}}v^{(1)}_{\mathbf{h}_2}(2)\cos(\Gamma_{\mathbf{h}_2}L+\delta^{(1)}) & e^{i\delta^{(2)}}v^{(2)}_{\mathbf{h}_2}(2)\cos(\Gamma_{\mathbf{h}_2}L+\delta^{(2)}) & \cdots \\
\vdots & \cdots & \cdots & \cdots \\
\vdots & \cdots & \cdots & \cdots \\
\mathbf{h}_N & \vdots & \vdots & \ddots
\end{array}
\begin{pmatrix} C_1 \\ C_2 \\ C_3 \\ \vdots \\ \vdots \\ C_j \\ \vdots \\ C_{2N} \end{pmatrix} = 0. \qquad (39)$$

This equation reveals that the index j of the eigenvalue of S cannot, in general, be the index to specify the normal modes. Rather, combined effect of all j determines the normal modes. If it were not for the sum over j in Eq. (36), we would have obtained the eigenvalue equation from Eq. (38)

$$\cos(\Gamma_{\mathbf{h}}L+\delta^{(j)})=0, \qquad (40)$$

for a single j. This equation should be satisfied simultaneously for all $\mathbf{h}$'s by the eigenvalue of ω. This is indeed impossible, for a solution for ω of Eq. (40) of a particular $\mathbf{h}$ depends on that $\mathbf{h}$ and it cannot in general satisfy Eq. (40) for the other open channels.

We have so far concentrated on the even-parity solutions, constructed by using the even-parity eigenphase shifts $j = 1, 2, \ldots, 2N$. For the odd-parity eigenphase shifts $j = 2N+1, 2N+2, \ldots, 4N$, an analysis similar to the above leads to an odd-parity secular equation, which is given by Eq. (39) with the cosines all replaced by sines.

When the mirror symmetry is absent in the slab, a superposition of even and odd modes constitutes a solution. In this case, the phase space of $j = 1, 2, \ldots, 2N$ and that of $j = 2N+1, 2N+2, \ldots, 4N$ no longer decouple. Extension to this less symmetric case is similarly carried out. Our remaining task is to count the number of solutions of Eq. (39) in a given frequency range.

III. CHANGE OF DENSITY OF STATES

Let us denote the matrix appearing in Eq. (39) of the even-parity modes as M. The eigenvalues for the normal modes are obtained from

$$\det \mathrm{M} = 0. \qquad (41)$$

We can eliminate from M the factors that are irrelevant in determining the eigenvalues. First, we divide each of the columns by

$$e^{i\delta^{(1)}},\ e^{i\delta^{(2)}},\ \ldots. \qquad (42)$$

We further eliminate the factor $\cos\Gamma_{\mathbf{h}}L$ from the $\mathbf{h}$th rows and $\cos\delta^{(j)}$ from the jth column of the matrix M, making use of

$$\cos\left(\Gamma_{\mathbf{h}}L+\delta^{(j)}\right)=\cos\Gamma_{\mathbf{h}}L\cos\delta^{(j)}[1-\tan\Gamma_{\mathbf{h}}L\tan\delta^{(j)}]$$

in Eq. (39). These factors can be removed because they are independent either of the phase shifts $\delta^{(1)}, \delta^{(2)}, \ldots$ or the size L of the boundary condition: the eigenvalues ω must depend on them both in view of the induced shifts of frequency from the free-space values. By this procedure we are left with

$$\det \mathrm{M} = 0 \longrightarrow \det \mathrm{M}' = 0, \qquad (43)$$

where

$$\mathrm{M}' = \begin{pmatrix} v_{\mathbf{h}_1}^{(1)}(1)(1 - \tan\Gamma_{\mathbf{h}_1} L \tan\delta^{(1)}) & v_{\mathbf{h}_1}^{(2)}(1)(1 - \tan\Gamma_{\mathbf{h}_1} L \tan\delta^{(2)}) & \cdots \\ v_{\mathbf{h}_1}^{(1)}(2)(1 - \tan\Gamma_{\mathbf{h}_1} L \tan\delta^{(1)}) & v_{\mathbf{h}_1}^{(2)}(2)(1 - \tan\Gamma_{\mathbf{h}_1} L \tan\delta^{(2)}) & \cdots \\ v_{\mathbf{h}_2}^{(1)}(1)(1 - \tan\Gamma_{\mathbf{h}_2} L \tan\delta^{(1)}) & v_{\mathbf{h}_2}^{(2)}(1)(1 - \tan\Gamma_{\mathbf{h}_2} L \tan\delta^{(2)}) & \cdots \\ v_{\mathbf{h}_2}^{(1)}(2)(1 - \tan\Gamma_{\mathbf{h}_2} L \tan\delta^{(1)}) & v_{\mathbf{h}_2}^{(2)}(2)(1 - \tan\Gamma_{\mathbf{h}_2} L \tan\delta^{(2)}) & \cdots \\ \cdots & \cdots & \cdots \\ \cdots & \cdots & \cdots \\ \vdots & \vdots & \ddots \end{pmatrix}. \tag{44}$$

The poles of the factors

$$\tan\Gamma_{\mathbf{h}_1} L,\ \tan\Gamma_{\mathbf{h}_2} L,\ \ldots$$

of M′ or the solutions of $\cos\Gamma_{\mathbf{h}} L = 0$ in the complex ω plane, give even-parity eigenvalues of photons in the free space bounded by the mirrors. Therefore, we conclude that the eigenvalues perturbed by the presence of the PC are given by the zeros of $\det \mathrm{M}'$, while the unperturbed eigenvalues in the absence of the PC are given by the poles of $\det \mathrm{M}'$. Thus, the increment of the number of the normal modes due to the presence of the slab PC in a frequency interval is given by the number of poles therein minus the number of zeros.

From the theory of complex function (see Ref. 12, for example), the increment of the number of modes of wave vector $\mathbf{k}_\parallel$ in the frequency interval $[\omega_0, \omega]$, denoted as $\Delta N_{\mathbf{k}_\parallel}(\omega_0; \omega)$, is given by

$$\Delta N_{\mathbf{k}_\parallel}(\omega_0; \omega) = -\frac{1}{\pi}\mathrm{Im}\left[\log\frac{\det \mathrm{M}'(\omega + \mathrm{i}\epsilon)}{\det \mathrm{M}'(\omega_0 + \mathrm{i}\epsilon)}\right], \tag{45}$$

where $\mathrm{Im}\,[\cdots]$ stands for the imaginary part of $[\cdots]$ and $+\mathrm{i}\epsilon$ ($\epsilon = +0$) shows that the logarithms are evaluated on the upper edge of the branch cut on the real ω axis. The change of DOS at the frequency ω, denoted by $\Delta\rho_{\mathbf{k}_\parallel}(\omega)$, is obtained by differentiating $\Delta N_{\mathbf{k}_\parallel}(\omega_0; \omega)$ with respect to ω.

It seems difficult to reduce $\det \mathrm{M}'$ further to obtain $\Delta\rho_{\mathbf{k}_\parallel}(\omega)$ because the dependences on the column index $\mathbf{h}$ and row index j are both present in the matrix elements of Eq. (44). In the special limit $L \to \infty$, however, we can proceed further to arrive at the final analytical expression. In this limit, we find (Appendix B)

$$\tan\Gamma_{\mathbf{h}}(\omega + \mathrm{i}\epsilon)L \to i \qquad (L \to \infty). \tag{46}$$

Thus, from Eq. (44), we find

$$\det \mathrm{M}' = \det \begin{bmatrix} v_{\mathbf{h}_1}^{(1)}(1) & v_{\mathbf{h}_1}^{(2)}(1) & v_{\mathbf{h}_1}^{(3)}(1) & \cdots \\ v_{\mathbf{h}_1}^{(1)}(2) & v_{\mathbf{h}_1}^{(2)}(2) & v_{\mathbf{h}_1}^{(3)}(2) & \cdots \\ v_{\mathbf{h}_2}^{(1)}(1) & v_{\mathbf{h}_2}^{(2)}(1) & \cdots & \cdots \\ v_{\mathbf{h}_2}^{(1)}(2) & v_{\mathbf{h}_2}^{(2)}(2) & \cdots & \cdots \\ \vdots & \vdots & \vdots & \ddots \end{bmatrix} \times \prod_{j=1}^{2N}(1 - i\tan\delta^{(j)}). \tag{47}$$

The first factor of the right-hand side is unity and can be removed. This property of the eigenvectors comes from the unitarity of the S matrix and the reality of the eigenvectors, the latter being guaranteed by the time reversal symmetry of the S matrix. Since

$$\begin{aligned} \mathrm{Im}\left[\log\prod_{j=1}^{2N}(1 - i\tan\delta^{(j)})\right] &= \sum_{j=1}^{2N}\mathrm{Im}\left[\log(1 - i\tan\delta^{(j)})\right] \\ &= -\sum_{j=1}^{2N}\delta^{(j)}, \end{aligned} \tag{48}$$

we find

$$\begin{aligned} \Delta\rho_{\mathbf{k}_\parallel}(\omega)^{(\mathrm{even})} &= \frac{d}{d\omega}\Delta N_{\mathbf{k}_\parallel}(\omega_0; \omega) \\ &= -\frac{d}{d\omega}\frac{1}{\pi}\mathrm{Im}\left[\log\prod_{j=1}^{2N}(1 - i\tan\delta^{(j)})\right] \\ &= \frac{1}{\pi}\sum_{j=1}^{2N}\frac{d\delta^{(j)}}{d\omega} \end{aligned} \tag{49}$$

for even-parity PBs. This is our final expression for the increment of DOS of even-parity PBs. We have assigned the superscript 'even' to emphasize that. The expression for the odd-parity PBs is similar except that the odd-parity eigenphase shifts $\delta^{(j)}$ ($j = 2N{+}1, 2N{+}2, \ldots, 4N$) are used:

$$\Delta\rho_{\mathbf{k}_\parallel}(\omega)^{(\mathrm{odd})} = \frac{1}{\pi}\sum_{j=2N+1}^{4N}\frac{d\delta^{(j)}}{d\omega}. \tag{50}$$

Altogether, we find

$$\begin{aligned} \Delta\rho_{\mathbf{k}_\parallel}(\omega) &= \Delta\rho_{\mathbf{k}_\parallel}(\omega)^{(\mathrm{even})} + \Delta\rho_{\mathbf{k}_\parallel}(\omega)^{(\mathrm{odd})} \\ &= \frac{1}{\pi}\sum_{j=1}^{4N}\frac{d\delta^{(j)}}{d\omega}, \end{aligned} \tag{51}$$

i.e. the ω-derivative of the sum of the $4N$ eigenphase shifts gives the total change of DOS. This expression of the total increment is shown to be valid in the absence of the mirror symmetry in the xy plane of the PC.

IV. APPLICATION TO PHOTONIC CRYSTALS OF SPHERES ARRAYED IN A SQUARE LATTICE AND A SIMPLE CUBIC LATTICE

In this section, we apply the above formula to slab PCs of arrayed spheres. We examine 2D systems of dielectric spheres arrayed periodically. Based on Eqs. (49) and (50), we calculate the DOS for monolayer and stacked layer model PCs. We choose n, the refractive index of spheres, to be 1.44, having in mind polytetrafluoroethylene (PTFE)[13] spheres whose diameter is in the millimeter range, and let the ratio of radius a of spheres to lattice constant d be $a/d = 0.5$, for the system of spheres just in contact in the square lattice. These parameters correspond to the PCs, which were actually prepared and used to examine their optical properties experimentally in the millimeter wavelength region of light.[14]

Light scattering from a slab of arrayed dielectric spheres is treated precisely by the vector KKR formalism[15–17] and layer KKR formalism,[6,17] which give us high-quality numerical data for the T and R lights and hence the S matrix defined by Eq. (26) for a prescribed $\mathbf{k}_\parallel$ value. All the eigenphase shifts are then obtained by numerically diagonalizing the S matrix. We emphasize that Eqs. (49) and (50) are general, not limited to systems of spheres, if only the amplitudes of T and R lights of all the open channels are calculated. We assume the square lattice of spheres in the lateral plane and the simple cubic lattice when the layers are stacked.

First we study the monolayer system. This system was examined both theoretically and experimentally by Ohtaka, et al.,[11] Kondo, et al.[18] and Yano, et al..[19] Theoretical analysis was also given for the DOS in the frequency region of no diffraction. In what follows, we investigate the increment of DOS for the lateral wave vector $\mathbf{k}_\parallel d/2\pi = (0.3,\ 0)$, which was chosen arbitrarily.

Figure 5 depicts 2D RL points in the $k_x k_y$ plane, each specified by the point $(2\pi/d)(m,\ n)$ of the square lattice. A circle of radius ω is also shown with its center placed at $\mathbf{k}_\parallel d/2\pi = (-0.3,\ 0)$. In the figure, circles of three different radii are drawn. From Eq. (5), the channel $\mathbf{h}$ opens when the radius increases with ω to cross the point $\mathbf{h}$. The number of the RL points inside the circle is equal to the number of open channels at ω.

For an incident light of frequency ω and wave vector $\mathbf{k}_\parallel$, we can imagine an Ewald sphere of radius ω in the $(k_x k_y k_z)$ space, whose center is placed at

$$\left(-\mathbf{k}_\parallel,\ -\sqrt{(\omega/c)^2 - \mathbf{k}_\parallel^2}\right).$$

The vector drawn from this center to the origin $\mathbf{k} = 0$ represents the incident wave vector $\mathbf{k}^+$. A circle of Fig. 5 may also be viewed as a locus of this Ewald sphere cut by the plane $k_z = -\sqrt{(\omega/c)^2 - \mathbf{k}_\parallel^2}$, where the center is lying; in this picture, the lattice points of Fig. 5 are the horizontal view of the 2D reciprocal lattice *rods* arrayed parallel to z.

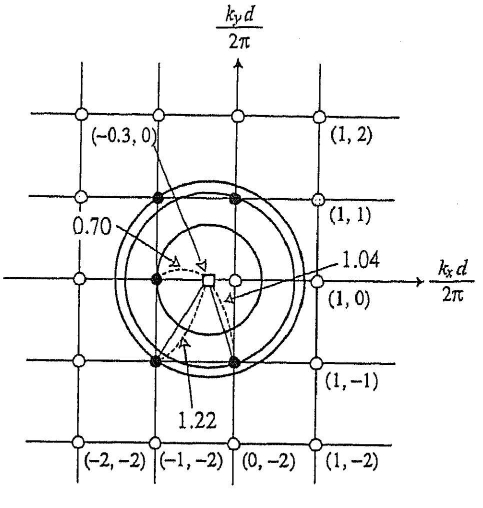

FIG. 5: Circles of radius ω and 2D reciprocal lattices (RL) in the $k_x k_y$ plane. The center of the circles shown by the open square is taken at $(k_x,\ k_y)(d/2\pi) = (-0.3,\ 0)$, corresponding to the incident condition $\mathbf{k}_\parallel d/2\pi = (0.3,\ 0)$ under study. The RL points of the square lattice are shown by open and solid points. Three circles are given to show the critical situations of channel opening, with the touching RL point of each case indicated by the filled lattice point.

As ω increases in Fig. 5 with $k_x d/2\pi$ fixed at 0.3, the circle becomes larger, touching first the point $\mathbf{h}d/2\pi = (-1,\ 0)$ at $\omega d/2\pi c = 0.70$, when the diffracted T light of $\mathbf{k}_\mathbf{h}^+$ and R light of $\mathbf{k}_\mathbf{h}^-$ start to appear in channel $\mathbf{h}d/2\pi = (-1,\ 0)$. The frequency $\omega d/2\pi c = 1.044$ is for the second contact, when two additional channels, $\mathbf{h}d/2\pi = (0,\ 1)$ and $(0,\ -1)$, open. The third (fourth) contact takes place at $\omega d/2\pi c = 1.221$ (1.30). Figure 6 shows N, the number of open channels, in the $(k_x,\ \omega)$ plane for the incident light of $\mathbf{k}_\parallel = (k_x,\ 0)$. The vertical dashed line corresponds to the case $(k_x,\ k_y)(d/2\pi) = (0.3, 0)$, presented in Fig. 5.

In the frequency region $0 < \omega d/2\pi c < 0.70$, there is no diffraction ($N = 1$) for $(k_x,\ k_y)(d/2\pi) = (0.3, 0)$. We have one plane-wave T light of a complex amplitude T_{00} and one R light of a complex amplitude R_{00}, representing directly transmitted light and specularly reflected light. The S matrix is 4×4, yielding four eigenphase shifts by diagonalization. They are p-polarized and s-polarized eigenmodes, both classified further into even and odd parities of the mirror reflection in the xy plane. The p and s modes decouple because our choice of $\mathbf{k}_\parallel$ to be directed along the Δ axis of 2D Brillouin zone guarantees the mirror symmetry in the xz plane (the p mode is even and the s mode is odd). Analysis of Ref. 11 (Eqs. (A12) and (A15) thereof) proved that the sum of the four eigenphase shifts is equal to the sum of the phase of T_{00} of p-polarised incident light and that of s-polarized incident light for the frequency range of $N = 1$. Namely, the phase of T_{00} of the p-polarized light is equal to the sum of $(p+)$ and $(p-)$ eigenphase shifts. The same holds

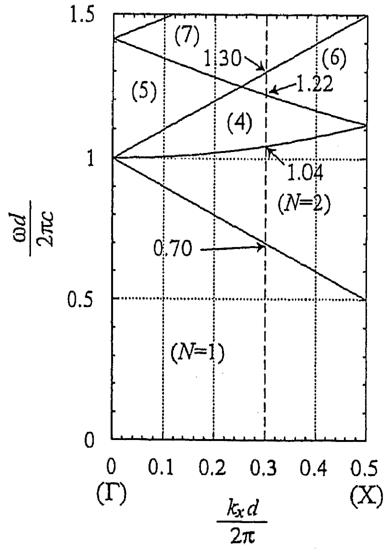

FIG. 6: Number of open 2D reciprocal lattice points as functions of ω and k_x, in the Γ-X direction ($k_y = 0$). The number N of the open RL points is given in parenthesis in each region. Three threshold values for $\omega d/2\pi c$ of channel opening are given for the case of $k_x d/2\pi = 0.3$, corresponding to the three circles of Fig. 5.

true for T_{00} of s-polarized light. Therefore, the DOS formula defined in Ref. 11 is reproduced by the special case $N = 1$ of the present general theory.

In the frequency region $\omega d/2\pi c \geq 0.70$, we enter the new regime of $N \geq 2$. We compare the calculated transmittance $|T_{00}|^2$ of the direct light with the DOS formula. We restrict ourselves to the response of the s-polarized incident light, because the discussion of the p incidence is similar.

Let us first examine what the previous DOS formula, valid only for $N = 1$, yields in the case of $N \geq 2$. Namely, we plot the phase of T_{00} of s light as our DOS. Figure 7(a) shows the calculated $|T_{00}|^2$ for the s-light, and Fig. 7(b) shows the phase of the s-light T_{00}. Note that we can treat *scalar* T_{00} in obtaining the phase because the polarization of the directly transmitted light is the same as the incident light for $\mathbf{k}_{\parallel}$ along the Δ axis. There is perfect coincidence in the positions of the fine structures in Figs. 7(a) and 7(b). Consequently, the DOS formula valid for $N = 1$ still works in the case $N \geq 2$ for simply determining the existence of PBs. However, we note that a correct DOS change due to the presence of a PB mode should be one, i.e. the sum of the phase shifts should change by π, whenever ω increases to cross a PB mode.[11] In Fig. 7(b), we see that the change of the phase shift at any fine structure is very short of π. (For comparison, in Fig. 8, we plot the situation seen in the region of $N = 1$ to show that the procedure indeed works there.) Neither the DOS of PBs nor the leakage-induced lifetime estimated from Fig. 7(b) is hardly reliable. For example, peaks and humps of the curves of Fig. 7(b) produce singular line-shapes in the DOS profile when differentiated according to Eqs. (49) and (50), quite different from Lorentzian shapes expected from the general theory of lifetime broadening. To summarize, the straightforward extension of the DOS formula of $N = 1$ to the new region of $N \geq 2$ does not give correct information. This incorrect procedure using the previous DOS formula does not take proper account of diffracted waves. So we apply the present formula defined by Eqs. (49) and (50) to this condition.

Figure 7(c) depicts the sum of the eigenphase shifts

$$\sum_{j=1}^{4N} \delta^{(j)} \tag{52}$$

of Eq. (51), which we claim to be a correct formula for the increment of DOS. We can easily classify by inspection the whole set of eigenphase shifts into the p- and s-polarized modes by the numerically calculated eigenvectors of S. We retain in (c) only the phase shifts of s-polarized modes to obtain the DOS of s-active PBs, which is to be compared with the s transmittance $|T_{00}|^2$ given in (a). We display the sum of the phase shifts by dividing it into ± parities of the mirror symmetry with respect to the xy plane. Panel (c) obviously confirms that the sum of the eigenphase shifts corrects the insufficient magnitudes of the jumps at the excited PB modes shown in Fig. 7(b).

Figure 7(d) shows its ω-derivative, the DOS of the PBs of $(k_x, k_y)(d/2\pi) = (0.3, 0)$. The DOS profile consists of Lorentzian peaks, as it should, whose full width at half maximum (FWHM) gives the inverse of the lifetime of the PBs. Any optical response of a PC is related more or less to its DOS profile and generally has a resonant enhancement accompanying a PB excitation. For example, the FWHM of excited PB modes primarily determines the emission spectrum from an atom in a PC. Three DOS peaks around $\omega d/2\pi c \simeq 1.3$ of Fig. 7(d) provide an estimate FWHM $= \Delta\omega d/2\pi c \simeq 0.01$, leading to an estimate of $Q = \omega/\Delta\omega \simeq 100$. The kinks seen at the frequencies of channel opening in Fig. 7(d) are interesting. The singular behavior of the spectrum associated with the channel opening has been historically named the Wood anomaly[20] and was analyzed in detail in quantum mechanics text book.[21] Various kinds of singularities, appearing often as sharp kinks but sometimes as dips or inflection points, are known to arise in the transmission spectrum. See Ref. 22 for the variety of singularities in the case of a PC. In Fig. 7(d), we have plotted the *increment* of DOS due to the presence of a slab PC and denoted it simply as DOS. Actually, therefore, a negative DOS of Fig. 7(d) just above the channel opening stands for a *decrease* of DOS. We believe the negative increment of DOS to be a genuine feature associated with Wood anomalies.

Next, we turn to the systems composed of stacked layers of arrayed PTFE spheres. Let N_s be the number of

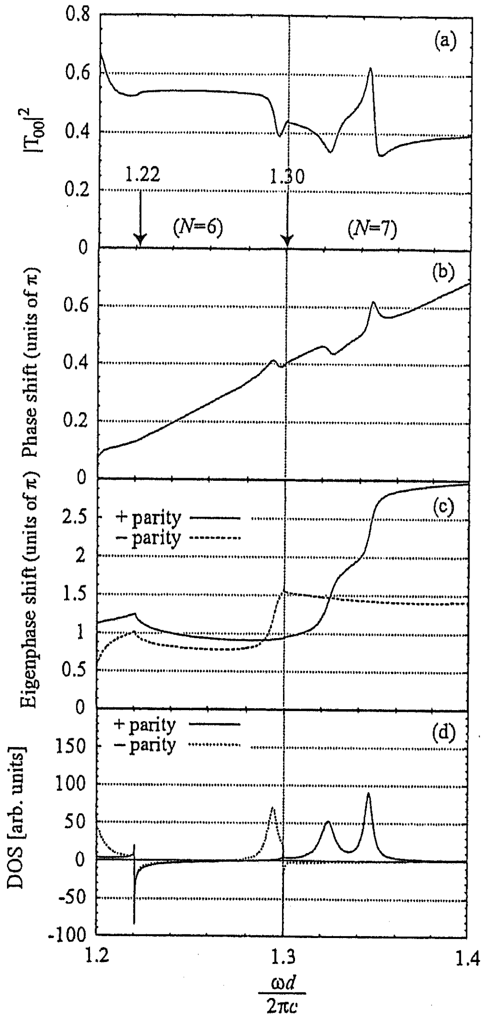

FIG. 7: Frequency dependence in the region $1.2 < \omega d/2\pi c < 1.4$ of transmittance and increment of DOS of s-polarized light with $(k_x, k_y)(d/2\pi) = (0.3, 0)$. The calculation is made for a monolayer PC consisting of a square array of dielectric spheres, whose parameters are given in the text. Panel (a) shows the transmittance of the direct light (h = 0), defined by $|T_{00}|^2$. Two arrows indicate the threshold frequencies for the change of the number N of open channels, one from the case of $N = 4$ to $N = 6$ at $\omega d/2\pi c = 1.22$ and the other from $N = 6$ to $N = 7$ at $\omega d/2\pi c = 1.30$. See Fig. 5 for the values of the threshold frequency. Panel (b) shows the phase of the complex amplitude derived from $T_{00}/|T_{00}|$, which would yield a correct sum of the eigenphase shifts when $N = 1$. Panel (c) shows the sum of the eigenphase shifts derived from the formula (51). Only the eigenphase shifts of s-polarized modes are retained. Panel (d) gives the correct DOS of the s-polarized PBs, which is defined by Eq. (51). See the text for the cause of the sharp decreases of DOS seen just at the channel openings.

stacked layers. For this case, too, a theoretical analysis of DOS was given previously in the region of $N = 1$.[19]

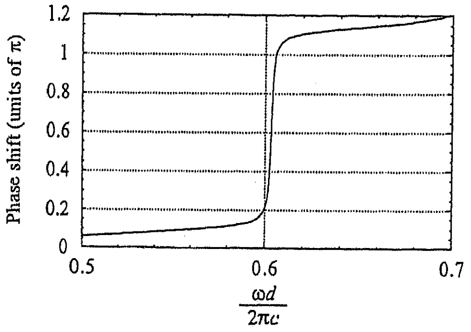

FIG. 8: Typical example of an abrupt phase change of the complex transmission amplitude. The phase obtained from $T_{00}/|T_{00}|$ is plotted in the frequency region of $N = 1$. The light is s-polarized with $(k_x, k_y)(d/2\pi) = (0.3, 0)$, incident on the monolayer PC used in Fig. 7. The change of the phase is just π.

In the bilayer system ($N_s = 2$), the monolayer photonic-bands of each of the two layers, which will be doubly degenerate if they are sufficiently far apart, are coupled to produce bonding and antibonding PB states.[23,24] Therefore, as N_s increases, the band population increases in a given frequency range. Figure 9 shows DOS obtained from our formulae [Eqs. (49) and (50)] for several N_s in the same frequency range and array of spheres as above. Except in the regions of channel opening, we can clearly see the bonding and antibonding splitting, when N_s becomes twice as large. The resonant optical response of a PB becomes sharper and sharper in accordance with the sharpening of DOS peaks as N_s increases. We can see that the DOS peaks for $N_s = 4$ have their Q values several times larger than those in the system of $N_s = 1$, estimated above to be about 100. In this way, we can quantitatively discuss the bonding and antibonding splitting of lifetime-broadened degenerate levels through the correct DOS formula and can calculate the Q values of the split levels as functions of N_s. These features are extensions of what was found previously in the frequency region of no diffraction.[25]

The plot of the positions of the DOS peaks as functions of $\mathbf{k}_\|$ gives the band structure of leaky PBs. Figure 10(a) illustrates the band structure for $\mathbf{k}_\| = (k_x, 0)$, i.e. along the Γ-X direction of the monolayer PC examined in Fig. 7. We show only the band structure of s-active PBs, derived from the s-active eigenphase shifts. The empty (filled) circles correspond to the modes with even (+) (odd (−)) parity with respect to the xy mirror symmetry. The general features of the calculated band structure are understandable using the band structure of an empty lattice. The similarity to an empty lattice stems from the fact that we have used a small refractive index $n = 1.44$ in the analysis. For a PC of larger n, no problem arises except for a slower convergence in the calculation of the matrix S, which, too, is overcome by the KKR formulation used here.

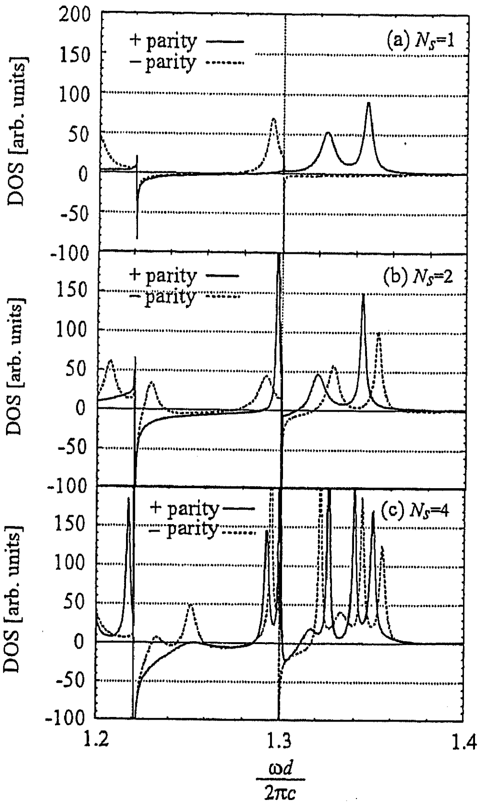

FIG. 9: Increment of DOS of a slab PC of stacked 2D layers as a function of frequency. N_s is the number of stacked layers. The result is given for PBs of s polarization with $(k_x, k_y)(d/2\pi) = (0.3, 0)$. Panel (a) is a reproduction of Fig. 7(d) and shows the DOS of a monolayer PC ($N_s = 1$). The solid (dashed) curve shows the even-parity (odd-parity) PBs. The Q values of PBs improve, or their lifetimes become longer and the density of the peaks increases, when N_s increases.

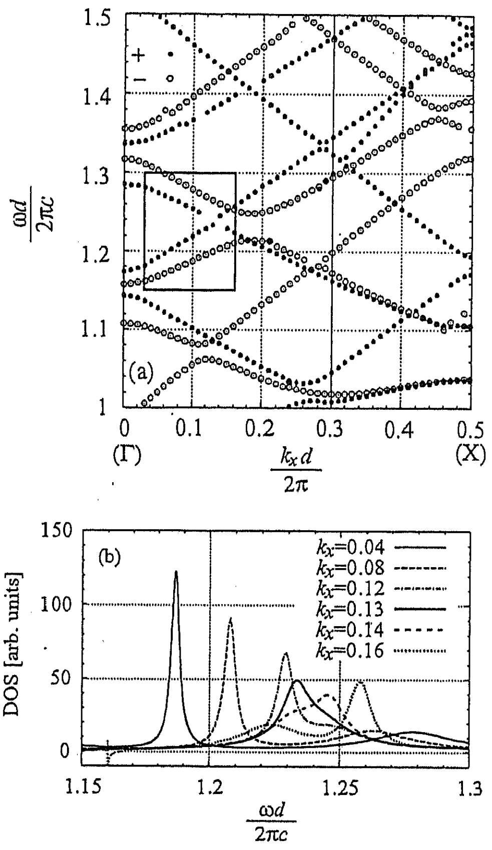

FIG. 10: Band structure and the wave-vector dependence of the DOS profile (s-polarized PBs). Panel (a) shows the band structure of a 2D PC (a monolayer array of spheres) along the Γ-X axis in the 2D Brillouin zone. The parameters for the PC are the same as used above. The solid circles correspond to the even-parity modes of s polarization, while the dotted circles represent the odd-parity modes of s polarization. A vertical line is drawn at $k_x d/2\pi = 0.3$, corresponding to the case examined in Fig. 7. Panel (b) shows how the width of a DOS peak depends on the band index and wave vector. The phase space enclosed by the rectangle in (a) is examined in (b).

In the band structure of Fig. 10(a), there are some bands have disconnected parts, which are too broad to produce a distinct peak there. Figure 10(b) illustrates this feature in the frequency region enclosed by the square in Fig. 10(a). The DOS profiles for even-parity (+) modes with several values of k_x are given in Fig. 10(b), which shows that the lifetime of a leaky PB depends both on the wave vector k_x and the band index.[2,3,11] As k_x becomes larger, the two peaks approach and at $k_x = 0.13$ they coalesce into a single broad peak, shown by the thick solid line. A further increase in k_x, however, resolves two modes again (e.g., the case of $k_x d/2\pi = 0.16$). Near $k_x d/2\pi = 0.13$, we cannot follow the two modes precisely.

V. SUMMARY

This paper presents a formula for the DOS of leaky PBs. The DOS of PBs in the leaky region of the phase space $(\omega, \mathbf{k}_\parallel)$ is a key factor that determines the magnitude of the resonant enhancement of optical signals from PCs, such as the emission cross-section of photons from an imbedded atom, for example.[26-30] In the DOS calculation, a complication arises from the need to take account of the presence of energy-carrying diffraction channels. We have shown that the DOS of leaky PBs of slab PCs is obtained from the complex transmission and reflection amplitudes of all the lights incident in the open channels and that it is expressed by the eigenphase shifts obtained by diagonalizing the S matrix defined using all the diffracted lights.

Based on the derived formula, we analyzed the transmittance of incident light for PCs of arrayed spheres and demonstrated that the extended definition of the scattering matrix given in this paper is very crucial in the frequency range where the diffraction channels are open. To show the usefulness of the formula, we have calculated the dispersion relations and lifetime of PBs from the DOS profile obtained for a model PC of arrayed spheres of finite thickness.

Since the formula requires only the complex amplitudes of the reflected and transmitted waves, its applicability is quite general and not limited to PCs of spheres.

Acknowledgments

The present work is supported by "Promotion of Science and Technology" from the Ministry of Education, Sports, Culture, Science and Technology of Japan. This work is also supported by a Grant-in-Aid from the same ministry.

APPENDIX A: CHANGE BETWEEN THE LOCAL COORDINATES AND FIXED COORDINATES

Using the polar angles, $\theta_{\mathbf{h}}$, $\phi_{\mathbf{h}}$ of the wave vector $\mathbf{k}_{\mathbf{h}}$, defined with respect to the fixed coordinate system $\{xyz\}$, The $\{xyz\}$ components are transformed to those of the local coordinates $\{123\}$ of a light of wave vectors $\mathbf{k}_{\mathbf{h}}^{\pm}$ by a 3 × 3 transformation matrix

$$
\begin{aligned}
\mathrm{R}_{\mathbf{h}}^{\pm} &= \begin{pmatrix} R_{\mathbf{h}}^{1x} & R_{\mathbf{h}}^{1y} & R_{\mathbf{h}}^{1z} \\ R_{\mathbf{h}}^{2x} & R_{\mathbf{h}}^{2y} & R_{\mathbf{h}}^{2z} \\ R_{\mathbf{h}}^{3x} & R_{\mathbf{h}}^{3y} & R_{\mathbf{h}}^{3z} \end{pmatrix} \\
&= \begin{pmatrix} \cos\theta_{\mathbf{h}}\cos\varphi_{\mathbf{h}} & \cos\theta_{\mathbf{h}}\sin\varphi_{\mathbf{h}} & \mp\sin\theta_{\mathbf{h}} \\ \mp\sin\theta_{\mathbf{h}} & \cos\varphi_{\mathbf{h}} & 0 \\ \pm\sin\theta_{\mathbf{h}}\cos\varphi_{\mathbf{h}} & \pm\sin\theta_{\mathbf{h}}\sin\varphi_{\mathbf{h}} & \cos\theta_{\mathbf{h}} \end{pmatrix} \qquad (A1)
\end{aligned}
$$

The rule for transforming the tensor $\mathrm{T}_{\mathbf{hh}'}^{++}$ from fixed to local coordinates is then

$$
\begin{aligned}
\mathrm{T}_{\mathbf{hh}'}^{++} \longrightarrow \mathrm{R}_{\mathbf{h}}^{+}\mathrm{T}_{\mathbf{hh}'}^{++}\left(\mathrm{R}_{\mathbf{h}'}^{+}\right)^{\mathrm{t}} &= \begin{pmatrix} R_{\mathbf{h}}^{1x} & R_{\mathbf{h}}^{1y} & R_{\mathbf{h}}^{1z} \\ R_{\mathbf{h}}^{2x} & R_{\mathbf{h}}^{2y} & R_{\mathbf{h}}^{2z} \\ R_{\mathbf{h}}^{3x} & R_{\mathbf{h}}^{3y} & R_{\mathbf{h}}^{3z} \end{pmatrix} \\
&\times \begin{pmatrix} T_{xx}^{++} & T_{xy}^{++} & T_{xz}^{++} \\ T_{yx}^{++} & T_{yy}^{++} & T_{yz}^{++} \\ T_{zx}^{++} & T_{zy}^{++} & T_{zz}^{++} \end{pmatrix} \begin{pmatrix} R_{\mathbf{h}'}^{1x} & R_{\mathbf{h}'}^{2x} & R_{\mathbf{h}'}^{3x} \\ R_{\mathbf{h}'}^{1y} & R_{\mathbf{h}'}^{2y} & R_{\mathbf{h}'}^{3y} \\ R_{\mathbf{h}'}^{1z} & R_{\mathbf{h}'}^{2z} & R_{\mathbf{h}'}^{3z} \end{pmatrix}^{\mathrm{t}} . \qquad (A2)
\end{aligned}
$$

This procedure causes the matrix elements related to the local coordinate 3 (i.e. third row or third column of the right-hand side) to vanish naturally. In this way, we are left with a 2×2 matrix denoted $\widehat{\mathrm{T}}_{\mathbf{hh}'}^{++}$. By arranging $\widehat{\mathrm{T}}_{\mathbf{hh}'}^{++}$, etc., according to the channel labels, we may construct a $4N \times 4N$ S matrix. This is the S matrix S defined by Eq. (26).

When we impose the boundary condition at the boundary mirrors on the x and y components of the electric field of channel $\mathbf{h}$, we have to return from the local coordinates $\{123\}$ to the $\{xyz\}$ system. For the components 1 and 2 of the jth eigenvector $\mathrm{v}_{\mathbf{h}}^{(j)}$ introduced in Eqs. (27) and (29), this is accomplished by

$$
\begin{pmatrix} (v_{\mathbf{h}}^{(j)})_x \\ (v_{\mathbf{h}}^{(j)})_y \end{pmatrix} = (\mathbf{r}_{\mathbf{h}}^{+})^{\mathrm{t}} \begin{pmatrix} (v_{\mathbf{h}}^{(j)})_1 \\ (v_{\mathbf{h}}^{(j)})_2 \end{pmatrix}, \qquad (A3)
$$

where the 2 × 2 transformation matrix $(\mathbf{r}_{\mathbf{h}}^{+})^{\mathrm{t}}$ is the 2 × 2 upper left block of

$$
(\mathbf{R}_{\mathbf{h}}{}^{+})^{-1} = (\mathbf{R}_{\mathbf{h}}{}^{+})^{\mathrm{t}} = \begin{pmatrix} (x,1) & (x,2) & (x,3) \\ (y,1) & (y,2) & (y,3) \\ (z,1) & (z,2) & (z,3) \end{pmatrix}, \qquad (A4)
$$

where $\mathbf{R}_{\mathbf{h}}^{+}$ is defined by (A1) and $(x,3)$, for example, is the direction cosine between the x and 3 axes. The (x,y) component of $\mathrm{v}_{\mathbf{h}}^{(j)}$ is obtained compactly by

$$
\begin{pmatrix} x \\ y \end{pmatrix} = \mathbf{r}_{\mathbf{h}}^{+} \begin{pmatrix} 1 \\ 2 \end{pmatrix}, \qquad (A5)
$$

namely the product $\mathbf{r}_{\mathbf{h}}^{+}\mathrm{v}_{\mathbf{h}}^{(j)}$ gives the x and y components of $\mathrm{v}_{\mathbf{h}}^{(j)}$. This product notation is used in Eq. (37).

APPENDIX B: REDUCTION OF THE MATRIX M'

In Eq. (5) we note

$$
\begin{aligned}
\Gamma_{\mathbf{h}}(\omega + \mathrm{i}\epsilon') &= \sqrt{[(\omega+\mathrm{i}\epsilon')/c]^2 - (\mathrm{k}_{\parallel}+\mathrm{h})^2} \\
&= \sqrt{(\omega/c)^2 - (\mathrm{k}_{\parallel}+\mathrm{h})^2} + \mathrm{i}\epsilon \\
&\equiv \Gamma_{\mathbf{h}} + \mathrm{i}\epsilon \qquad (B1)
\end{aligned}
$$

with an infinitesimal $\epsilon\,(\epsilon > 0)$, and hence

$$
e^{\mathrm{i}\Gamma_{\mathbf{h}}(\omega+\mathrm{i}\epsilon')L} = e^{\mathrm{i}\Gamma_{\mathbf{h}}L - \epsilon L}. \qquad (B2)
$$

Thus

$$
\tan\Gamma_{\mathbf{h}}(\omega+\mathrm{i}\epsilon')L = -i\frac{\exp(\mathrm{i}\Gamma_{\mathbf{h}}L - \epsilon L) - \exp(-\mathrm{i}\Gamma_{\mathbf{h}}L + \epsilon L)}{\exp(\mathrm{i}\Gamma_{\mathbf{h}}L - \epsilon L) + \exp(-\mathrm{i}\Gamma_{\mathbf{h}}L + \epsilon L)}. \qquad (B3)
$$

In the limit $L \to \infty$, we obtain

$$
\tan\Gamma_{\mathbf{h}}(\omega+\mathrm{i}\epsilon')L \to i \qquad (L\to\infty). \qquad (B4)
$$

Therefore, the $\mathbf{h}$ dependence in the $(\mathbf{h}, j)$ matrix element

$$
1 - \tan\Gamma_{\mathbf{h}}(\omega+\mathrm{i}\epsilon')L\tan\delta^{(j)} \qquad (B5)
$$

of the matrix M′ disappears and we obtain Eq. (47).

[1] K. M. Ho, C. T. Chan, and C. M. Soukoulis, Phys. Rev. Lett. **65**, 3152 (1990).

[2] T. Ochiai and K. Sakoda, Phys. Rev. B **63**, 125107 (2001).

[3] S. Fan and J. D. Joannopoulos, Phys. Rev. B **65**, 235112 (2002).

[4] See, e.g., P. Fulde, J. Keller and G. Zwicknagl, *Solid State Physics* (Academic Press, New York, 1988) eds. F. Seits, D. Turnbull and H. Ehrenreich, vol. 41, p. 2; A. C. Hewson, *Kondo Problem to Heavy Fermions* (Cambridge University Press, Cambridge, 1993).

[5] See, e.g., G. D. Mahan, *Many-Particle Physics*, 3rd ed. (Kluwer Academic, Plenum, New York, 2000), p. 195.

[6] K. Ohtaka and Y. Tanabe, J. Phys. Soc. Jpn., **65**, 2276 (1996).

[7] K. Sakoda, Opt. Express **4**, 167 (1999); K. Sakoda, K. Ohtaka, and T. Ueta, *ibid*, **4**, 481 (1999).

[8] F. J. Garcia de Abajo, Phys. Rev. Lett. **82**, 2776 (1999); Phys. Rev. E **61**, 5743 (2000).

[9] K. Ohtaka and S. Yamaguti, Opt. Spectrosc. **91**, 506 (2001); Opt. Quantum Electron. **34**, 235 (2002).

[10] S. Yamaguti, J. Inoue, H. Haeberlé, and K. Ohtaka, Phys. Rev. B **66**, 195202 (2002).

[11] K. Ohtaka, Y. Suda, S. Nagano, T. Ueta, A. Imada, T. Koda, J. S. Bae, K. Mizuno, S. Yano, and Y. Segawa, Phys. Rev. B **61**, 5267 (2000).

[12] P. Lloyd, Proc. Phys. Soc. **86**, 825 (1965).

[13] J. R. Birch, J. D. Dromey, and J. Lesurf, Infrared Physics **21**, 225 (1981).

[14] T. Kondo (unpublished).

[15] K. Ohtaka, Phys. Rev. B **19**, 5057 (1979).

[16] K. Ohtaka, J. Phys. C **13**, 667 (1980).

[17] N. Stefanou, V. Karathanos, and A. Modinos, J. Phys.: Condens. Matter **4**, 7389 (1992); A. Modinos, N. Stefanou, and V. Yannopapas, Opt. Express **8**, 197 (2001).

[18] T. Kondo, M. Hangyo, S. Yamaguchi, S. Yano, Y. Segawa, and K. Ohtaka, Phys. Rev. B **66**, 033111 (2002).

[19] S. Yano, Y. Segawa, J. S. Bae, K. Mizuno, K. Ohtaka, and S. Yamaguchi, Phys. Rev. B **63**, 153316 (2001); S. Yano, Y. Segawa, J. S. Bae, K. Mizuno, S. Yamaguchi, and K. Ohtaka, Phys. Rev. **66**, 075119 (2002).

[20] R. W. Wood, Philos. Mag. **4**, 396 (1902); J. W. S. Rayleigh, Philos. Mag. **14**, 60 (1907).

[21] L. D. Landau and E. M. Lifshitz, *Quantum Mechanics*, 2nd ed. (Pergamon, London, 1965), p. 565.

[22] K. Ohtaka and M. Inoue, Phys. Rev. B **25**, 677 (1982); M. Inoue, K. Ohtaka and S. Yanagawa, *ibid*, **25**, 689 (1982).

[23] M. Bayer, T. Gutbrod, J. P. Reithmaier, A. Forchel, T. L. Reinecke, P. A. Knipp, A. A. Dremin, and V. D. Kulakovskii, Phys. Rev. Lett. **81**, 2582 (1998).

[24] T. Mukaiyama, K. Takeda, H. Miyazaki, Y. Jimba, and M. Kuwata-Gonokami, Phys. Rev. Lett. **82**, 4623 (1999).

[25] K. Ohtaka, J. Lightwave Technol. **17**, 2161 (1999).

[26] E. Yablonovitch, Phys. Rev. Lett. **58**, 2059 (1987).

[27] S. John and T. Quang, Phys. Rev. A **50**, 1764 (1994); T. Quang, M. Woldeyohannes, S. John, and G. S. Agarwal, Phys. Rev. Lett. **79**, 5238 (1997).

[28] T. Suzuki and P. K. L. Yu, J. Opt. Soc. Am. B **12**, 570 (1995).

[29] Z. Y. Li, L. L. Lin, and Z. O. Zhang, Phys. Rev. Lett. **84**, 4341 (2000).

[30] V. Lousse and J. P. Vigneron, Phys. Rev. B **64**, 201104 (2001).

Photonic material for designing arbitrarily shaped mirrors and microcavities in two dimensions

Hiroshi Miyazaki[a] and Yoichi Kurokawa
Department of Applied Physics, Tohoku University, Aramaki, Sendai
980-8579, Japan
Masashi Hase, Hideki T. Miyazaki, and Norio Shinya
[1] National Institute for Materials Science (NIMS), 1-2-1 Sengen, Tsukuba
305-0047, Japan

(Dated: November 5, 2003)

Abstract

Based on the numerical finding of a two-dimensional photonic material which has large complete photonic gaps and structural uniformity, we propose a photonic plate which can be used to design arbitrarily shaped photonic mirrors and microcavities on a wavelength scale. This paper describes a wavelength-sized parabolic mirror that can collect light very efficiently without loss. In addition, we present circular microcavities of tunable resonance frequencies with high values of quality factor Q.

PACS numbers: 71.55.Jv, 42.70.Qs, 42.25.Dd

§1 INTRODUCTION

Photonic crystals (PhCs) are artificial photonic materials whose periodic structure engenders photonic gaps (PGs), ranges of frequencies at which light cannot propagate within the PhCs. Using these PGs, PhCs can be used to confine or guide light within the wavelength scale. Their increased use is anticipated for wide technological applications in the near future.[1–3] One example is an optical waveguide, which is ordinarily formed by removing periodic elements along a certain line. Consequently, its structure should be commensurate with the periodicity of the host PhC. This characteristic is different from the conventional waveguides of microwaves, which are made of metal plates. Metals can reflect microwaves of arbitrary incidence angle without loss. Therefore, optical materials that have both complete PG and structural flexibility in the wavelength scale are necessary to create such an arbitrarily shaped waveguide in the optical region.

We recently proposed a two-dimensional photonic material: uniformly distributed photonic scatterers (UDPS).[4] UDPS are formed by randomly placing parallel dielectric rods under the condition that distance $|R_i–R_j|$ between the centers of ith and jth rods, R_i and R_j, is larger than a certain value D_{min}, i.e., $|R_i–R_j| > D_{min}$. When rods have sufficient density and dielectric contrast, UDPS have large complete PG. Our study also demonstrated the highly efficient transmission of light in arbitrarily shaped waveguides that is comparable with wavelength λ. Such efficiency is achieved by combining UDPS and smooth side walls made of periodic rods. The present study shows that combined use of UDPS and side walls, which we call a UDPS plate, enables us to design two-dimensional curved mirrors and microcavities of arbitrary shape whose size can be reduced to the wavelength order.

§2 UDPS PLATES

Figure 1(a) shows an example of UDPS plates. Periodic rods of radius a and dielectric constant $\varepsilon=12$ surround a rectangular region of $|x|<80a$ and $-26.67a<y<0$. Each rod is represented by a white circle. Then, we fill the surrounded region with UDPS. We generate more than one million random sets of rod positions within the rectangular region and place rods successively so that the distances between a rod and those already placed are always greater than D_{min}. This procedure yields extremely uniform and dense rod distribution if the number of randomly generated rod positions is sufficiently large. In this study, we commonly choose $D_{min}=4a$. Transmittance T is obtained for plane wave incidence of TM or TE (E or H // rod axis) mode from the positive y axis by calculating the energy flow at the line L using the multiple scattering method.[5]

Average transmittances over five rod configurations including Fig. 1(a) are shown by blue (TM) and red (TE) lines in Fig. 1(c) as a function of size parameter $\Omega= 2\pi a/\lambda$. Adopting the gap condition as $|T|<0.01$, we find the PG of TM mode as $0.362<\Omega<0.508$ with average penetration depth of about $2a$. The PG of TE mode is $0.732<\Omega<0.782$. Figure 1(a) shows distributions of total electric field intensity and energy flow (white arrows) for TM mode incidence at $\Omega=0.40$ ($\lambda = 15.71a$). One can see the yellow-red region of large intensity lying parallel to the upper side wall. Its periodicity equals the wavelength. Therefore, the UDPS plate in Fig. 1(a) can be regarded as an ideal flat mirror without loss. Detailed calculation reveals that we can effectively replace this UDPS plate with a perfectly reflecting flat mirror at $y=0.7a$.

To illustrate the importance of the upper side wall, Fig. 1(b) shows an example of incomplete UDPS plates in which the upper side wall is removed from Fig. 1(a) and UDPS are filled in. Average transmittance of TM mode over five cases including Fig. 1(b) is shown in Fig. 1(c) by the green line. As shown, the gap position and depth are almost identical to the blue line, indicating that gap structure is independent of the presence of the upper side wall. However, the reflected electric field differs completely. We show in Fig. 1(b) the distributions of total electric field intensity and energy flow at Ω=0.40. The irregular presence of large intensity regions is shown by the yellow or red dots in front of incomplete UDPS plate. This distribution demonstrates that the smoothness of side walls is an essential prerequisite for the UDPS plate to work as an ideal mirror. A recent independent report has indicated the importance of side walls for efficient transmission in the waveguide of PhCs.[6]

§3 UDPS MICRO MIRRORS AND CAVITIES

Figure 1 illustrates the simple procedure for producing a UDPS plate of arbitrary shape: first decide the side wall shape; then fill the surrounding region with UDPS. Thereby, if we place periodic rods along a curve, we can produce a curved mirror of arbitrary shape and dimension. Figure 2(a) shows such an example in which the upper side wall consists of equidistant rods (period=4a) on the parabola $y=x^2/(4f)$ with $f=16.67a$. Here, we relaxed the UDPS condition $D_{min}<|R_i-R_j|$ at right and left corners of upper side walls for simplicity of construction. Figure 2(b) shows the TM mode transmittance of plane wave incidence from positive y axis. Obviously, we observe the same PG with that in Fig. 1(c). Distribution of scattered electric field intensity at Ω=0.45 is also plotted in Fig. 2(a). The incident plane wave from positive y axis is collected reasonably well at the focal point (x=0, $y=f$) of a parabolic mirror in the geometrical optics. This fact indicates that the UDPS plate in Fig. 2(a) can be regarded as an almost ideal parabolic mirror.

Structural flexibility of UDPS plate allows formation of a two-dimensional microcavity[7] of arbitrary shape with great ease. Figures 3(a)–3(c) show circular cavities of inner and outer radius R_{in} and R_{out} between which we fill the UDPS. The red line in Fig. 3(d) is a plot of normalized electromagnetic energy U stored within the cavity in Fig. 3(a) or 3(b) for plane wave incidence of TM mode from the positive y axis. Sharp peaks appear at Ω=0.40586, 0.40702, 0.43054, 0.48318, and 0.48580 within PG. These states are resonance states of the cavity. Corresponding values of quality factor Q at these peaks are 1.49×10^7, 1.37×10^7, 2.56×10^7, 2.95×10^6, and 3.77×10^6.

Figures 3(a) and 3(b) also show distributions of total electric field intensity and energy flow at Ω=0.40586 and 0.43054, respectively. The intensity distribution inside the cavity, shown in Fig. 3(a), has four-fold symmetry indicating that this peak corresponds to the state with azimuthal quantum number m=2, whereas that in Fig. 3(b) represents the state with m=0. The peak at Ω=0.40702 also shows four-fold symmetry, but its distribution is rotated by $\pi/4$ from that in Fig. 3(a). This rotation is also evident for peaks at Ω=0.48318 and 0.48580, which represent the resonance states with m=3. We can also observe smooth energy flow around the outer circle. This flow smoothness indicates that the outer side wall plays the role of a circular mirror.

Resonance frequencies of the present circular cavity can be obtained approximately from the condition that the electric field vanishes at the inner boundary R=R_{in}. Corresponding size parameters are given in terms of the zeroes of the Bessel function $J_m(j_{mk})=0$ ($m\geq0$, $k\geq1$) as $\Omega_{mk}=j_{mk}a/R_{in}$. For $R_{in}=13.33a$, we have non-degenerate level $\Omega_{m=0,k=2}=0.4140$, and two doubly degenerate levels $\Omega_{m=2,k=1}=0.3852$ and $\Omega_{m=3,k=1}=0.4785$ within PG. These values concur well with those in Fig. 3(d). To achieve better agreement, we simply reduce the cavity radius R_{in} by the order of rod radius a, which is consistent with the position of perfectly reflecting flat mirror in Fig. 1(a). The lift of degeneracy is caused by local non-uniformity of rod distribution in UDPS. The resonant field has exponentially decaying amplitude within the UDPS region. Because the field distributions at Ω=0.40586 and 0.40702 differ by $\pi/4$ rotation, they are influenced by the difference of the rod distribution within UDPS, as shown in Fig. 3(a).

From a practical point of view, it is desirable to use single mode cavity with, say, m=0 and k=1 mode. Such a single mode cavity can be designed easily using a UDPS cavity. If this mode is chosen to appear in the middle of PG at, e.g., Ω=0.425, the cavity radius is determined as R_{in}=5.66a because $j_{m=0,k=1}$=2.405 and $R_{in}=j_{mk}a/\Omega_{mk}$. A cavity of this size is plotted in Fig. 3(c), where UDPS plate thickness (R_{out}-R_{in}) is identical to that of Figs. 3(a) and 3(b). Corresponding normalized internal energy is shown by the green line in Fig. 3(d) for plane wave incidence of TM mode from positive y axis. As shown in that figure, only a single sharp peak appears at Ω=0.45527 with Q=8.30 × 10^6, shifted 7 % from the predicted position. We also show in Fig. 3(c) the corresponding distributions of total electric field intensity and energy flow.

We will briefly discuss the origin of PGs in UDPS. PGs are formed either by coherent interference of scattered waves from periodic rods like Bragg diffraction in X-rays or by bonding and anti-bonding states of Mie resonance within each rod that are similar to electronic bandgaps in semiconductors. The latter are formed by local interaction. Therefore, they are not as easily smeared out by fluctuations in position and radius of rods as in the former case. Therefore, we conclude that PGs of UDPS result from interaction of Mie resonance states. However, an important difference exists between electrons and photons: resonance wavefunctions of photons are not localized exponentially. Rather, they decay in inverse power and have a long-range nature. This long-range nature of wavefunctions is responsible for formation of PGs in UDPS which do not require even a short-range order. Consequently, UDPS can acquire tremendous structural flexibility that is free from either long-range or short-range ordering.

§4 SUMMARY

We have proposed a two-dimensional photonic material called UDPS plate. It is a combination of smooth side walls and UDPS filling material. UDPS plate allows the design of arbitrarily curved mirrors of wavelength size and circular microcavity of requested resonance frequencies. Because the UDPS cavity shape is not limited to that of a circle, UDPS plate provides an intriguing research field of various microcavities of complicated shapes. Detailed discussion of various characteristics of UDPS plates will be undertaken in future studies.

Acknowledgments

This work was supported by a Grant-in-Aid for Scientific Research from the Ministry of Education, Culture, Sports, Science, and Technology. One author (H. M.) particularly thanks R. Ohkawa for his continued encouragement and inspiration.

[a] Electronic address: hmiyazak@olive.apph.tohoku.ac.jp

[1] J. D. Joannopoulos, P. R. Villeneuve, and S. Fan, Nature 386, 143 (1997).

[2] A. Mekis, J. C. Chen, I. Kurland, Shanhui Fan, Pierre R. Villeneuve, and J. D. Joannopoulos, Phys. Rev. Lett. 77, 3787 (1996).

[3] S.-Y. Lin, E. Chow, V. Hietala, P. R. Villeneuve, and J. D. Joannopoulos, Science 282, 274 (1998).

[4] H. Miyazaki, M. Hase, H. T. Miyazaki, Y. Kurokawa, and N. Shinya, Phys. Rev. B 67, 235109 (2003).

[5] H. A. Yousif and S. Kohler, J. Opt. Soc. Am. A 5, 1085 (1988).

[6] K.-C. Kwan, X. Zhang, Z.-Q. Zhang, and C. T. Chan, Appl. Phys. Lett. 82, 4414 (2003).

[7] E. Yablonovitch, T. J. Gmitter, R. D. Meade, A. M. Rappe, K. D. Brommer, and J. D. Joannopoulos, Phys. Rev. Lett. 67, 3380 (1991).

Fig. 1: (a), (b) Examples of UPDS plates. In (a), dielectric rods of radius a and ε=12 are arranged periodically within the vacuum as side walls along the rectangular region of $|x|<80a$ and $-26.67a<y<0$, whereas the upper side wall is removed in (b). Their periods are 4.0a and 4.44a along the x and y axes, respectively. The rectangle interior is filled with rods satisfying the condition that rod distance be larger than $D_{min}=4a$. Volume fractions V_f are 0.174 and 0.164 in (a) and (b), respectively. Distributions are also shown of the total electric field intensity and energy flow (white arrows) at Ω=0.40 for TM mode incidence of plane wave from the positive y axis. Intensity increases from blue to red with maxima of 4.73 and 7.53 in (a) and (b), respectively. (c) Transmittance as a function of size parameter $\Omega=2\pi a/\lambda$ at the line L of length 5.67a placed at $y=-28.17a$. The plane wave of TM or TE mode is incident from the positive y axis. Transmittance is the average of five configurations including (a) or (b).

Fig. 2: (a) Parabola mirror made of UDPS plate, (b) Transmittance of TM mode at line L. Plane wave of TM mode is incident from the positive y axis. Rods are placed along the rectangular region of $|x|<44.80a$ and $-20a<y<30.13a$. Lower and right or left side walls are made with period 4.07a and 4.59a, respectively. The upper side wall is formed by putting rods with period 4a along the parabola $y=x^2/4f$ with f=16.67a. Volume fraction V_f is 0.189. In addition, (a) shows the distribution of scattered field intensity at Ω=0.45 in the region $|x|<66.67a$ and $-40a<y<93.33a$ with maximum intensity of 24.67.

Fig. 3: (a), (b), and (c) Circular cavities of inner radius R_{in} and outer radius R_{out}. R_{in}=13.33a, R_{out}=40a, and V_f = 0.169 in (a) and (b) while R_{in}=5.66a, R_{out}=32.33a, and V_f=0.171 in (c). The plane wave of TM mode is incident from the positive y axis. Also shown are distributions of total electric field

intensity and energy flow at (a) Ω=0.40586, (b) Ω=0.43054, and (c) Ω=0.45527. Maximum field intensity is (a) 9.19×10^3, (b) 3.44×10^6, and (c) 1.42×10^6. (d) Normalized energy U stored within cavities for TM mode incidence. Red and green lines correspond to cavity (a) or (b), and (c), respectively.

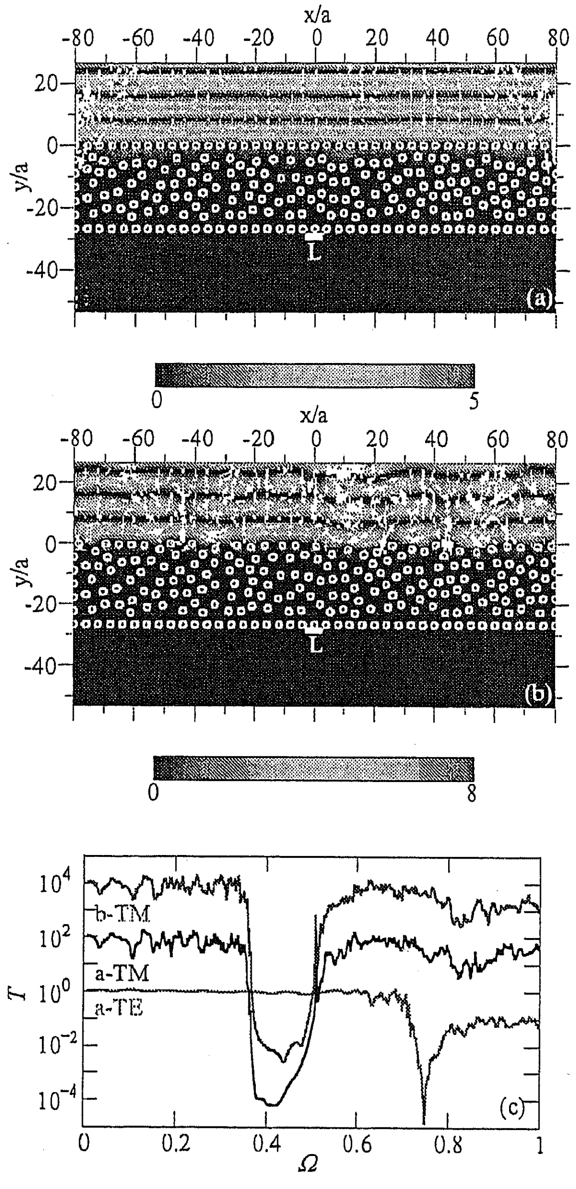
x/a
-80
-60
-40
-20
0
20
40
60
80
y/a
20
0
-20
-40
L
(a)
0
5
x/a
-80
-60
-40
-20
0
20
40
60
80
y/a
20
0
-20
-40
L
(b)
0
8
T
10^4
10^2
10^0
10^{-2}
10^{-4}
b-TM
a-TM
a-TE
(c)
0
0.2
0.4
0.6
0.8
1
Ω

Fig. 1

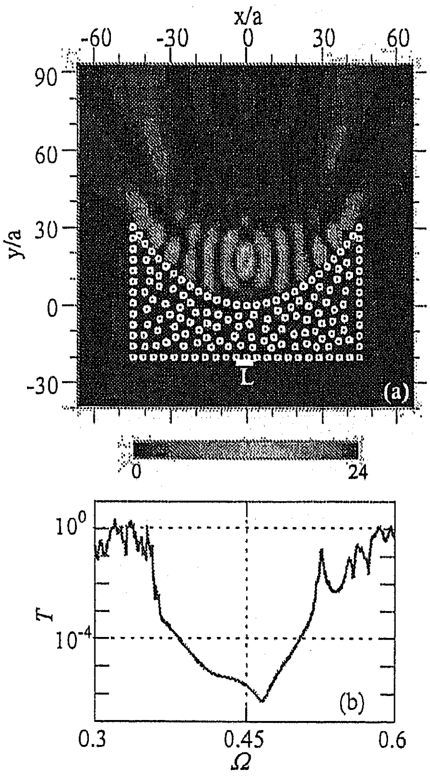

Fig. 2

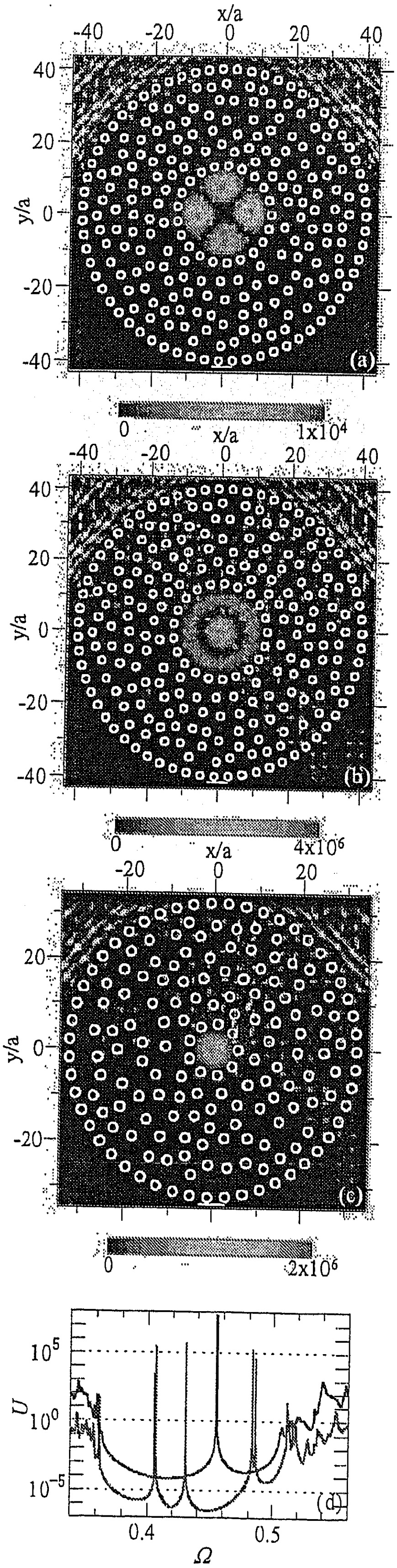
x/a
-40
-20
0
20
40
y/a
40
20
0
-20
-40
(a)
0
1x10^4
(b)
0
4x10^6
(c)
0
2x10^6
U
10^5
10^0
10^-5
(d)
0.4
0.5
Ω

Fig. 3